



# Turbine Vane External Heat Transfer

## Volume II.

### Numerical Solutions of the Navier-Stokes Equations for Two- and Three-Dimensional Turbine Cascades with Heat Transfer

By: R. J. Yang  
B. C. Weinberg  
S. J. Shamroth  
H. McDonald

Scientific Research Associates, Inc.  
Glastonbury, Connecticut

performed under subcontract for

Allison Gas Turbine Division  
General Motors Corporation  
Indianapolis, Indiana 46206-0420

## Final Report

prepared for

National Aeronautics and Space Administration  
NASA-Lewis Research Center  
Cleveland, Ohio 44135  
Contract No. NAS3-23695

N87-13661

Unclas  
43282

G3/34

(NASA-CR-174828) TURBINE VANE EXTERNAL HEAT  
TRANSFER. VOLUME 2. NUMERICAL SOLUTIONS OF  
THE NAVIER-STOKES EQUATIONS FOR TWO- AND  
THREE-DIMENSIONAL TURBINE CASCADES WITH HEAT  
TRANSFER Final Report (General Motors)





# **Turbine Vane External Heat Transfer**

## **Volume II.**

### **Numerical Solutions of the Navier-Stokes Equations for Two- and Three-Dimensional Turbine Cascades with Heat Transfer**

**By: R. J. Yang  
B. C. Weinberg  
S. J. Shamroth  
H. McDonald**

**Scientific Research Associates, Inc.  
Glastonbury, Connecticut**

**performed under subcontract for**

**Allison Gas Turbine Division  
General Motors Corporation  
Indianapolis, Indiana 46206-0420**

**Final Report  
July 1985**

**prepared for**

**National Aeronautics and Space Administration  
NASA-Lewis Research Center  
Cleveland, Ohio 44135  
Contract No. NAS3-23695**





## TABLE OF CONTENTS

<u>Section</u>	<u>Title</u>	<u>Page</u>
I	Summary . . . . .	1
II	Introduction . . . . .	2
III	Analysis . . . . .	6
IV	Test Cases and Results . . . . .	30
V	Conclusions . . . . .	55
	Appendix A--Solution Procedure . . . . .	57
	Appendix B --User's Manual . . . . .	64
	Appendix C--List of Acronyms, Abbreviations, and Symbols . . .	145
	References . . . . .	149

**PRECEDING PAGE BLANK NOT FILMED**

# LIST OF ILLUSTRATIONS

<u>Figure</u>	<u>Title</u>	<u>Page</u>
1	C-type grid for Turner cascade geometry . . . . .	7
2	Constructive O-type coordinate system . . . . .	9
3	Four basic loops of the constructive coordinate system . . . . .	10
4	O-type grid coordinate system for Turner cascade . . . . .	12
5	O-type grid coordinate system for C3X cascade . . . . .	13
6	Three-dimensional C3X cascade with endwall . . . . .	26
7	C-type coordinate system for Turner cascade . . . . .	31
8	Pressure coefficients distribution of the subsonic laminar cascade . . . . .	32
9	Pressure coefficients distribution of the subsonic turbulent cascade . . . . .	33
10	Turner cascade pressure distribution of the transonic case . . . . .	35
11	Comparison of measured and calculated pressure distribution of the C3X cascade . . . . .	37
12	Surface temperature distribution for case 144 . . . . .	38
13	Comparison of measured and calculated pressure distributions of the C3X cascade for cases 144, 148, and 158 . . . . .	39
14	Vector plot for C3X cascade, case 144 . . . . .	40
15	Comparison of measured and calculated heat transfer coefficient distributions of the C3X cascade . . . . .	41
16	The effect of film cooling on heat transfer coefficient distributions . . . . .	42
17	The effect of film cooling on pressure coefficient distributions . . . . .	44
18	Temperature contours . . . . .	45
19	Pressure contours . . . . .	46
20	Mach number contours . . . . .	47
21	Three-dimensional rectilinear pressure coefficient distribution of the C3X cascade . . . . .	49
22	Static pressure contour at the endwall . . . . .	50
23	Static pressure contour at the 3.5% spanwise plane . . . . .	50

# LIST OF ILLUSTRATIONS (CONT)

<u>Figure</u>	<u>Title</u>	<u>Page</u>
24	Static pressure contour at the midspan plane . . . . .	51
25	Leading edge vector plot at the 0.135% spanwise plane . . . .	52
26	Leading edge vector plot at the 2.95% spanwise plane . . . . .	53
27	Leading edge vector plot at the midspan plane . . . . .	54
28	The overall program flow for program COORD . . . . .	66
29	The overall program flow for program DAL . . . . .	67
30	The program flow chart for subroutine READA . . . . .	68
31	The program flow chart for subroutine EXEC . . . . .	69
32	Cascade geometry . . . . .	72

# LIST OF TABLES

<u>Table</u>	<u>Title</u>	<u>Page</u>
I	COORD namelist input description . . . . .	70
II	MINT namelist input description . . . . .	73
III	List of major FORTRAN variables in MINT . . . . .	77
IV	Sample input for COORD . . . . .	81
V	Sample inputs for MINT code . . . . .	82
VI	Sample outputs for COORD program . . . . .	83
VII	Sample outputs for MINT code . . . . .	94

## I. SUMMARY

The multidimensional, ensemble-averaged, compressible, time-dependent Navier-Stokes equations have been used to study the turbulent flow field in two- and three-dimensional turbine cascades. The viscous regions of the flow were resolved and no-slip boundary conditions were used on solid surfaces. The calculations were performed in a constructive O-type grid, which allows representation of the blade rounded trailing edge. Converged solutions were obtained in relatively few time steps (~80-150) and comparisons of both surface pressure and heat transfer showed good agreement with the data. The three-dimensional turbine cascade calculation showed many of the expected flow field features.

## II. INTRODUCTION

An important factor in the overall design of advanced gas turbine engines is the flow in and about the turbine blade passages. These components are a source of aerodynamic loads and losses that can control the overall machine efficiency and that may be subject to extreme heat transfer problems. Inaccurate estimates of both loss coefficients and heat transfer rates may lead to erroneous predictions of engine performance and to poor component life or even catastrophic failure of component parts, respectively. Therefore, an accurate estimate of both the flow field and the accompanying heat transfer properties in the turbine passages would be a valuable tool for the gas turbine design engineer.

In recent years, reliable and efficient computational procedures for predicting the flow field and the accompanying heat transfer characteristics within the turbine blade passages have been developed. Several methods for analyzing the two-dimensional (2-D) passages in the turbine blades are available. Many analyses are based on solving inviscid flow equations (Ref 1 and 2) and, in many cases, these analyses are capable of predicting the blade pressure distribution well.

Due to a lack of any viscous phenomena, however, these analyses cannot predict heat transfer or loss information. To predict heat transfer and/or viscous loss data, a set of boundary layer equations can be solved in conjunction with the inviscid analysis. A review of boundary layer techniques for turbomachinery applications has been presented by McDonald (Ref 3). When the inviscid flow boundary layer analysis technique is used, the calculations can be made in an interactive or noninteractive mode. In the noninteractive mode, an inviscid flow is calculated and the boundary layer is then calculated subject to the inviscid flow pressure distribution. This approach is viable if viscous displacement effects are small. When viscous displacement effects are significant, then the calculation should be performed in an interactive mode (Ref 4), which recognizes the mutual dependence of the inviscid and viscous solutions.

An alternative method of determining the 2-D viscous flow in the turbine passages is to solve an ensemble-averaged set of Navier-Stokes (N-S) equations in conjunction with a turbulence model to predict the entire passage flow field.

The N-S procedure has distinct advantages over other methods. The N-S analysis precludes any need to divide the flow into inviscid and viscous subregions. Although in some cases such a division may not be troublesome, in other cases no clear cut division is obvious. The N-S analysis solves the entire flow field with a single set of equations and, therefore, the influence of the viscous phenomena, taken in the boundary layer and in the wake, on the pressure distribution is inherent in the solution. Similarly, streamwise flow separation is not difficult to solve with the N-S analysis. This fact is particularly important in cases involving distributed surface injection or blades subjected to high loading where local regions of separation, which may be regions of high heat transfer, may occur. Although boundary layer analyses can proceed through separation if approximations are made (Ref 5), such analyses contain serious approximations in and near the separated region if these regions are not small and thin. The results in this instance must be viewed with caution. The N-S analysis contains no approximations, other than those involved in turbulence modeling in this region.

When considering three-dimensional (3-D) cascades, which include endwall and corner effects, the flow phenomena become even more complicated. In addition to possible 2-D flow-type situations in the vicinity of the midplane, complex 3-D, viscous flow patterns appear in the endwall regions. These flow patterns include the leading edge horseshoe vortex at the strut endwall intersection, the complex vortex patterns passing through the passage (Ref 6), and the corner regions. These complex 3-D, viscous flow regions argue strongly for a full N-S approach.

In simple quasi-two-dimensional situations, the viscous and turbulent near wall region velocity profile can sometimes be described by 3-D extensions of the law of the wall for turbulent boundary layers, although these 3-D extensions are much less universal than their 2-D counterparts. In the complex 3-D flows existing in the turbine passage, the near wall flow is not well described by such a wall law. Consequently, it becomes necessary to define the near wall region with mesh points when heat transfer and loss mechanisms are of interest. The added mesh point density and the presence of these additional length scales in the solution place very stringent requirements on the numerical methodology.

Successful calculations that applied a N-S procedure to several 2-D cascade problems using no-slip boundary conditions (as opposed to a wall law) have been reported in Ref 7 through 12. The procedure used in these efforts was the consistently split linearized block implicit (LBI) scheme of Briley and McDonald (Ref 13). The numerical scheme is embodied in a general computer code termed MINT (multidimensional, implicit, nonlinear, time-dependent). The particular form of the code being used for the cascade application solves the general tensor form of the N-S equations and, therefore, can be used with a general coordinate system. The dependent variables in the analysis are the Cartesian velocity components, the density, and, if turbulent flow with a turbulence energy model is considered, the turbulence kinetic energy,  $k$ , and if a two-equation model is used, the dissipation rate,  $\epsilon$ . The choice of Cartesian velocity components as dependent variables is based on experience obtained with a variety of choices including the contravariant velocity components, the physical velocity components in the coordinate directions, and the Cartesian velocity components as discussed in Ref 14.

To date, the cascade analysis has been used to predict the 2-D flow in several cascade configurations using a C-type coordinate system. In Ref 10, flow fields were obtained for cascades formed by unstaggered NACA 0012 airfoils in subsonic laminar and turbulent flow. The results were obtained very economically in relatively few time steps ( $\sim 60$  for laminar flow) and showed the expected cascade flow field features. In Ref 11, the analysis was extended to the transonic regime and results were obtained for transonic flow through a Jose Sanz diffusion cascade. Once again, the results were obtained very economically in a relatively few number of time steps ( $\sim 150$ ) and showed the qualitative features expected in a transonic cascade flow field.

In particular, the analysis showed its capability to predict transonic flows with sharp shock definition and, on a grid point-to-point basis, to cost little more than an efficient solution of the Euler equations. One case study corresponded to conditions for which an inviscid, i.e. Euler equation, solution existed. The results of the N-S analysis showed good agreement with the inviscid result. The differences observed were consistent with the inclusion of viscous boundary layer development in the N-S analysis. In comparing the viscous and inviscid results, with this particular N-S solution procedure no Kutta condition or exit flow angle specification is required, the exit flow follows



the specifications of the inlet total pressure and the exit static pressure. Inviscid flow calculations with other boundary conditions have the possibility of being different by virtue of these boundary conditions. Ref 7 and 9 contain calculations for both subsonic and transonic compressor configurations and a transonic turbine configuration. The predicted blade pressure distributions were comparable with the measurements of Stephens and Hobbs (Ref 15) and Hobbs, Wagner, Dennenhoffer, and Dring (Ref 16). The subsonic cascade flow (Ref 16) had two boundary layer profile measurements at the 97% chord pressure and suction surface stations. Although only a tentative assessment of the procedure can be made on the basis of these two profiles in the immediate vicinity of the blade trailing edge, the comparison showed the predicted profiles to be in agreement with the measured data even though further turbulence modeling work with particular emphasis on transition was indicated.

This effort applies this same N-S procedure to 2-D and 3-D transonic turbine cascade flows. Such an application requires several new features, including a new coordinate capability, extension to three dimensions, and the inclusion of an energy equation in the governing system. In general, the geometrical configuration of the turbine blades impacts both the grid construction procedure and the implementation of the numerical algorithm. Because the turbine blades of interest, e.g. Turner and C3X turbine cascades, are characterized by very blunt leading edges, rounded trailing edges, and high stacking angles, a robust grid construction procedure that can accommodate the severe body shape while resolving regions of large flow gradients is required. A constructive O-type grid generation technique that meets these requirements has been developed and used in this effort. An energy equation was activated in the code, 2-D calculations employing the N-S procedure were performed for the Turner and C3X turbine cascades, and the predicted pressure coefficients and heat transfer rates were compared with experimental data wherever available. A calculation with a film-cooling option applied over the C3X turbine blade surface was also demonstrated. In addition, the corresponding 3-D rectilinear C3X turbine cascade in which blade-endwall effects are present is considered. Throughout the effort, no-slip boundary conditions with the viscous near wall definition of the flow were used as appropriate with the total pressure inflow and exit static pressure at outflow used to obtain the mass flow through the channel and to determine the flow turning. These boundary conditions were found the most plausible yet the least restrictive in terms of the predicted flow.

### III. ANALYSIS

This analysis is based on a solution of the ensemble-averaged Navier-Stokes (N-S) equations using the linearized block implicit (LBI) method of Briley and McDonald (Ref 13). The equations are solved in a constructive coordinate system (Ref 7) with density and the Cartesian velocity components as dependent variables. The application of the LBI method to the two-dimensional (2-D) cascade flow field problem together with the C-type grid coordinate system has been discussed in some detail in Ref 7 through 12. This effort deals with the application of the LBI method to the 2-D or 3-D transonic turbine cascade flow field problem using an O-type grid coordinate system and includes the effects of heat transfer.

#### COORDINATE SYSTEM

An important component of the turbine cascade analysis is the cascade coordinate system. Any coordinate system used in the analysis should satisfy conditions of generality, smoothness, resolvability, and allow easy application of boundary conditions. A coordinate system must be sufficiently general to allow application to a wide class of problems of interest if it is to be practical. The metric data associated with the coordinate system must be sufficiently smooth so that the variation from grid point to grid point does not lead to a numerical solution dominated by metric coefficient truncation error. This requirement differs from the requirement of the existence of a specified number of transformation derivatives. The coordinate system must resolve flow regions where rapid flow field changes occur. Finally, coordinates should allow accurate implementation of boundary conditions; for the cascade this requirement is equivalent to the requirement that the metric coefficients be continuous across the periodic lines where periodic boundary conditions are to be applied.

To date, several types of coordinate systems are available. These include solutions based on a conformal transformation, solutions based on the solution of a Poisson equation (Ref 17), and constructive systems. This effort uses a constructive system based on the approach of Eiseman (Ref 18). Shamroth, et al (Ref 7 through 12) have applied the constructive technique to generate C-

type grids for a variety of cascades. The C-type grid requires an approximation of the actual trailing edge geometry by means of a cusped geometry (see Figure 1). Therefore, the computed results based on the C-type grid represent only solutions for approximated geometry instead of realistic ones. The effect of the trailing edge approximation will depend on the type of cascade being considered. In compressor-type cascades, the trailing edge radius is small and the viscous boundary layers are subjected to large adverse pressure gradients. Under these conditions, the blade viscous displacement effects are expected to dominate any trailing edge geometry approximations and, consequently, the cusped approximation should not significantly influence the results for compressor blade calculations. The situation is not as clear, however, for turbine blades. Turbine blades have a large trailing edge radius and their boundary layers are subjected to strong favorable pressure gradients. In transonic flow the pressure distribution and possibly the shock location are sensitive to small changes in the blade shape or the effective blade shape due to viscous effects. In these cases it is not clear if the trailing edge modification inherent in the C-type grid significantly affected results. As the first step in this effort, an O-type grid capability was developed.

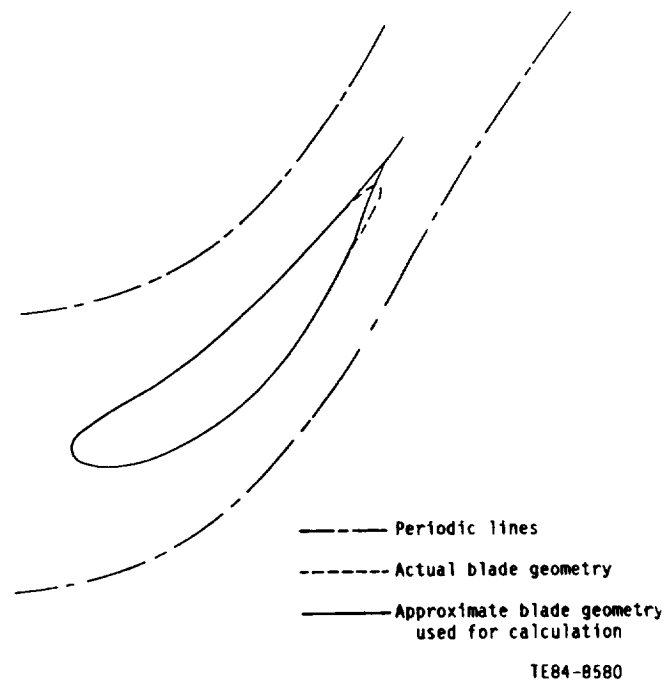


Figure 1. C-type grid for Turner cascade geometry.

A sketch of the O-type grid coordinate system is presented in Figure 2. In brief, the coordinate system consists of a set of two families of curves; the  $\xi$  equals constant curves such as lines FG or HI in Figure 2 and the  $\eta$  equals constant curves such as ABCDEA or A'FB'HA' in Figure 2. The coordinate system is constructed by first forming the inner loop A'FB'HA', which includes the blade. The blade may be specified either by an analytic equation or by discrete data points. If an equation is used then construction of the inner loop is straightforward. If the blade is specified by discrete data points then, in general, the points required on the inner loop will not coincide with any point used for blade specification. In this case, a curve fit is used to obtain the required inner loop points. The curve fit is based on a local parabolic fit. For any given point required on the inner loop, a parabola is fitted through three adjacent specifying points, two on the right and one on the left, with the axis of the parabolic normal to the chord line connecting the two outer points. A second parabola is then fitted through the two points on the left and the one on the right. The location of the required point is obtained by means of a weighted average of these curve fits. The weighting factor is determined by the distance from the required point to the center specifying point of each parabola. This calculation is followed by constructing an outer loop ABCDEA, which consists of periodic lines BC and DE, a frontal curve CD, and a rear cap EB. Both the inner and outer loops are then represented by parametric curves  $x = x(s)$  and  $y = y(s)$  where the parameter varies from zero to unity. The present coordinate generation process uses a two-part transformation for the inner loop. First,  $x$  and  $y$  are expressed as a function of  $s'$ , the physical distance along the curve. Then  $s'$  is normalized so that its range is between zero and unity. Second, a transformation based on Oh (Ref 19) is applied to the inner loop surface so that higher resolution at the leading and trailing edge of the blade are achieved. The Oh technique uses a truncated series of error functions and complimentary error functions as the basis of the transformation. The feature of the technique is that the locations that require higher resolution and their corresponding grid point numbers are specified explicitly through input. After applying Oh's transformation, the desired grid point locations are obtained simultaneously.

The outer loop is then parameterized to relate points on the outer loop to corresponding points on the inner loop. For two outer loop points that are

periodic, such as G and I in Figure 2, to maintain periodicity, it is necessary that  $S_G = 1 - S_I$ . These values will ensure that coordinate points on the upper and lower periodic lines will be periodically aligned.

The present parameterization applies Oh's technique on an iterative basis over surface ABCC' so that the grid point locations are obtained as desired. The grid point locations for the surface C'DEA are obtained by means of correspondence to those on the surface ABCC' again on an iterative basis using Oh's technique. This technique eliminates the complexity of the multipart transformation technique used previously (Ref 7 through 11), and the grid point locations are obtained directly through Oh's transformation.

Following the construction and determination of the grid point locations for the inner and outer loops, two intermediate loops are constructed as shown in Figure 3. The first intermediate loop is constructed around the blade surface with a normal distance,  $h_1$ , from the inner loop. A similar loop is constructed inside the outer loop with a normal distance,  $h_2$ , from the outer loop. Points on these intermediate loops must then be associated with a parameter  $s$ ,  $0 \leq s \leq 1$ . This association is accomplished as shown in Figure 3 by setting  $S_{A'} = S_A$  and  $S_{B'} = S_B$ . These four loops allow the construction of the pseudoradial lines such as GF of Figure 2 by means of the multiloop method originally developed by Eiseman (Ref 20).

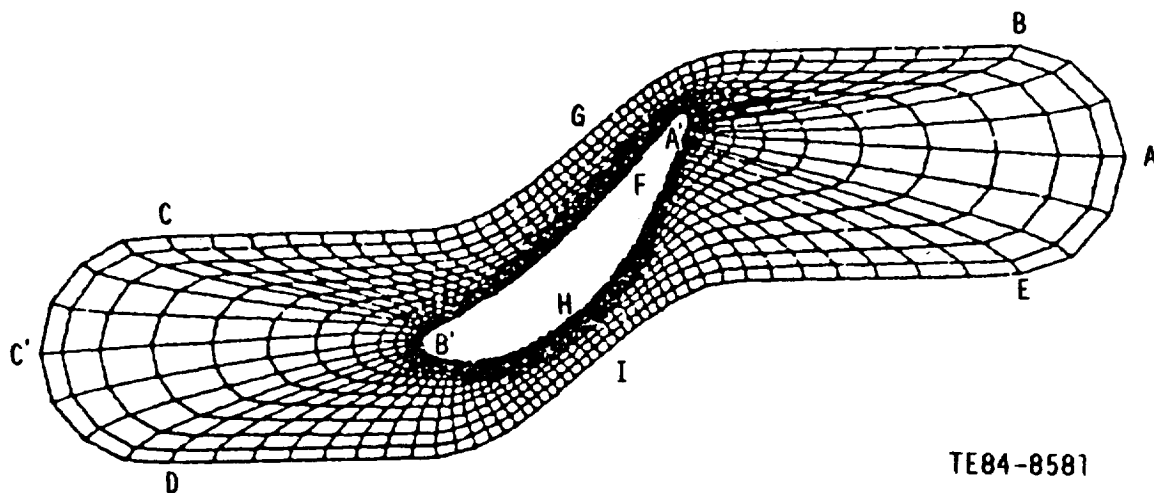
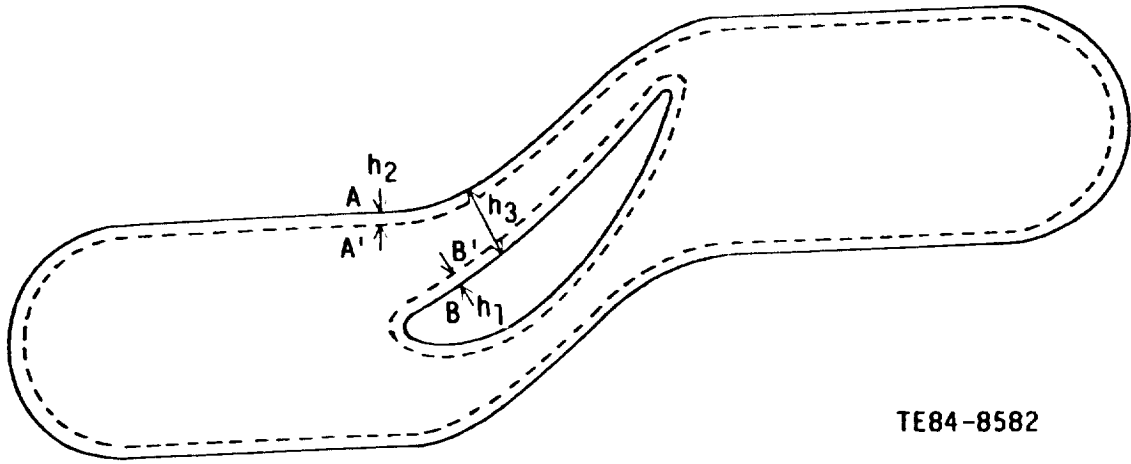


Figure 2. Constructive O-type coordinate system.



TE84-8582

Figure 3. Four basic loops of the constructive coordinate system.

The multiloop method requires introduction of a position vector,  $\vec{P}(r,s)$ , with components  $(x, y)$ , which will represent the coordinate location of grid points. Based on the four-loop construction process, vectors  $\vec{P}_i(s)$  are defined with  $i = 1, 2, 3, 4$ . Each  $\vec{P}_i$  has a coordinate  $(x_i, y_i)$  associated with it at specific values of  $s$  through the previously described construction process. A radial parameter,  $r_i$ , is then introduced. This parameter is defined, see Figure 3, as the distance from the loop in question to the inner loop normalized by the distance from the outer loop to the inner loop,  $h_3$ . Thus,  $r_1 = 0$ ,  $r_2 = h_1/h_3$ ,  $r_3 = (h_3 - h_2)/h_3$ ,  $r_4 = 1$ . With the definition of these quantities, the general position vector,  $\vec{P}(r, s)$ , is related to the loop position vectors,  $\vec{P}_1(s)$ ,  $\vec{P}_2(s)$ ,  $\vec{P}_3(s)$ , and  $\vec{P}_4(s)$ , by means of

$$\begin{aligned} \vec{P}(r,s) = & (1-r)^2(1-\alpha_1 r)\vec{P}_1(s) + (\alpha_1+2)(1-r)^2 r\vec{P}_2(s) \\ & + r^2[1-\alpha_2(1-r)]\vec{P}_4(s) + (\alpha_2+2)r^2(1-r)\vec{P}_3(s) \end{aligned} \quad (1)$$

where

$$\begin{aligned} \alpha_1 &= \frac{2}{3r_2-1} \\ \alpha_2 &= \frac{2}{3(1-r_2)-1} \end{aligned} \quad (2)$$

It should be noted that at  $r = 0$ ,  $\vec{P}(0,s) = \vec{P}_1(s)$  and at  $r = 1$ ,  $\vec{P}(1,s) = \vec{P}_4(s)$ . Further, because at  $r = 0$ ,

$$\frac{\partial P}{\partial r}(0, s) = [\bar{P}_2(s) - \bar{P}_1(s)](a_1 + 2) \quad (3)$$

and at  $r = 1$

$$\frac{\partial P}{\partial r}(1, s) = [\bar{P}_4(s) - \bar{P}_3(s)](a_2 + 2) \quad (4)$$

specification of the derivatives at the inner and outer boundaries is determined by the parametric representation of intermediate loops 2 and 3. Thus, the four-loop method allows specification of the boundary point locations and coordinate angles at these boundaries. This method of construction assures that the grid is orthogonal at the inner and outer loop boundaries.

After loops 2 and 3 are constructed to satisfy the coordinate angle at the boundary points, the grid is constructed as follows. If the grid is to contain  $M$  pseudoradial lines (such as line FG of Figure 2) and  $N$  pseudoazimuthal lines (such as line ABCDEA), the values of the pseudoradial coordinate are  $r(i) = i/(N - 1)$ ,  $i = 0, 1, 2, \dots, N - 1$  and the values of the pseudoazimuthal coordinates are  $s(j) = j/(M - 1)$ ,  $j = 0, 1, 2, \dots, M - 1$  then the position vector, i.e., the grid locations  $(x, y)$  for each point in the grid, is given by Equation (1).

The preceding discussion has assumed a uniform spacing in the radial direction. If radial grid point concentration is desired, it is necessary to assume a radial distribution function, such as

$$R = \left[ 1 - \frac{\tanh D(1-r)}{\tanh D} \right] \quad (5)$$

which concentrates points in the wall region. Grid points are then chosen at  $r(i) = (i)/(N-1)$  and the analysis proceeds as outlined.

Grids generated with this procedure are shown in Figures 4 and 5. Figure 4 represents a turbine cascade corresponding to the cascade of Turner (Ref 21). The second cascade, shown in Figure 5, corresponds to the C3X turbine cascade (Ref 22).

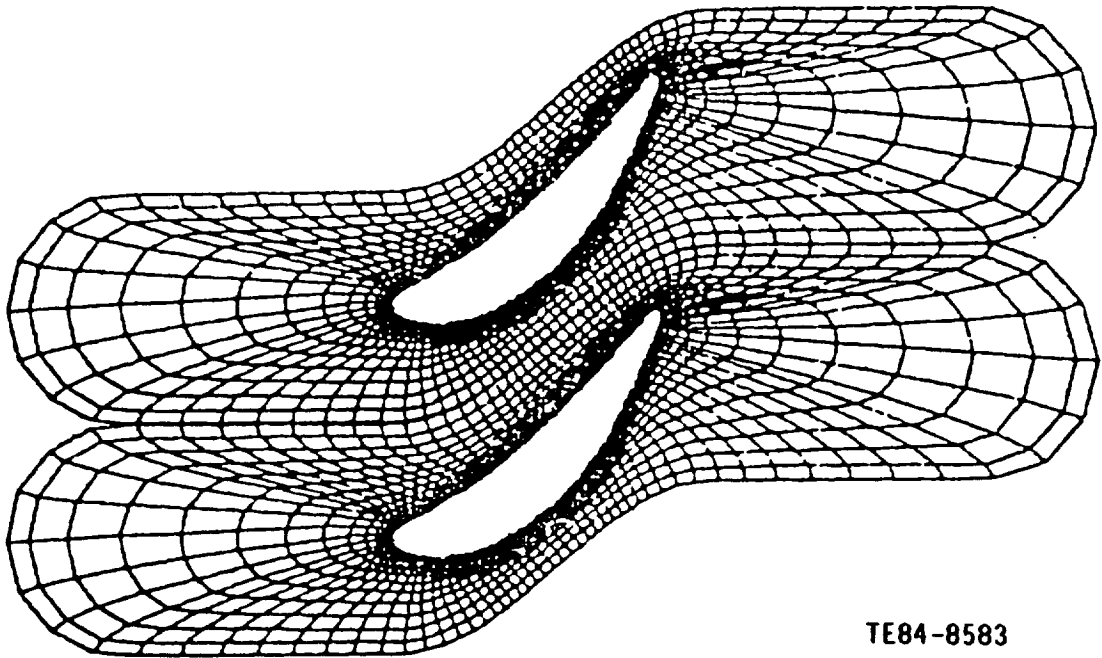
#### GOVERNING EQUATIONS

The ensemble-averaged, time-dependent N-S equations used in this project can be written in vector form as continuity

$$\frac{\partial \rho}{\partial t} + \nabla \cdot \rho \bar{\mathbf{U}} = 0 \quad (6)$$

momentum

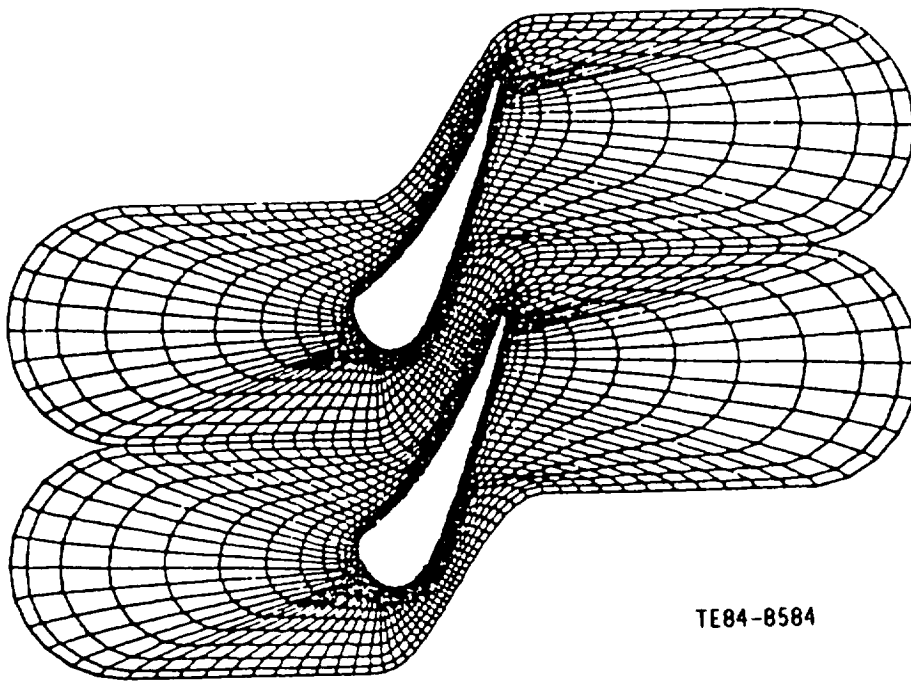
$$\frac{\partial \rho \bar{\mathbf{U}}}{\partial t} + \nabla \cdot (\rho \bar{\mathbf{U}} \bar{\mathbf{U}}) = -\nabla P + \nabla \cdot (\bar{\bar{\boldsymbol{\pi}}} + \boldsymbol{\pi}^T) \quad (7)$$



TE84-8583

Figure 4. 0-type grid coordinate system for Turner cascade.





TE84-8584

Figure 5. O-type grid coordinate system for C3X cascade.

and energy

$$\frac{\partial \rho h}{\partial t} + \nabla \cdot (\rho \bar{U} h) = -\nabla \cdot (\bar{Q} + \bar{Q}^T) + \frac{DP}{Dt} + \Phi + \rho \epsilon \quad (8)$$

where  $\rho$  is density,  $U$  is velocity,  $p$  is pressure,  $\bar{\pi}$  is the molecular stress tensor,  $\bar{\pi}^T$  is the turbulent stress tensor,  $h$  is enthalpy,  $\bar{Q}$  is the mean heat flux vector,  $\bar{Q}^T$  is the turbulent heat flux vector,  $\Phi$  is the mean flow dissipation rate and  $\epsilon$  is the turbulence energy dissipation rate. If the flow is assumed as a constant total temperature, the energy equation is replaced by

$$T_t = T + \frac{q^2}{2C_p} = \text{constant} \quad (9)$$

where  $T_t$  is the stagnation temperature,  $q$  is the magnitude of the velocity, and  $C_p$  is the specific heat at constant pressure. In a number of cases considered in this report, constant total temperature has been assumed constant. This assumption was made to reduce computer run time where the constant  $T_t$  assumption was warranted. Cases in which this substitution has been made are

identified in the description of the results. A number of terms in Equations 6 through 8 require definition. The stress tensor appearing in Equation 7 is defined as

$$\bar{\pi} = 2\mu \mathbb{D} - \left(\frac{2}{3}\mu - \kappa_B\right) \nabla \cdot \bar{\mathbf{U}} \mathbf{I} \quad (10)$$

where  $\kappa_B$  is the bulk viscosity coefficient,  $\mathbf{I}$  is the identity tensor, and  $\mathbb{D}$  is the deformation tensor, defined by

$$\mathbb{D} = \frac{1}{2} ((\nabla \bar{\mathbf{U}}) + (\nabla \bar{\mathbf{U}})^T) \quad (11)$$

In addition, the turbulent stress tensor has been modeled using an isotropic eddy viscosity so that

$$\pi^T = -\rho \overline{\mathbf{u}^T \mathbf{u}^T} = 2\mu_T \mathbb{D} - \frac{2}{3} (\mu_T \nabla \cdot \bar{\mathbf{U}} + \rho k) \mathbf{I} \quad (12)$$

where  $k$ , the turbulent kinetic energy, and  $\mu_T$ , the turbulent viscosity, are determined by a suitable turbulence model.

Equation (8) contains a mean heat flux vector defined as

$$\bar{\mathbf{Q}} = -\kappa \nabla T \quad (13)$$

and a turbulent heat flux vector defined as

$$\bar{\mathbf{Q}}^T = -\kappa^T \nabla T \quad (14)$$

where  $\kappa$  and  $\kappa^T$  are the mean and turbulent thermal conductivities, respectively.

The mean flow dissipation term,  $\Phi$ , which also appears in Equation (8), is defined as

$$\Phi = 2\mu \mathbb{D} : \mathbb{D} - \left(\frac{2}{3}\mu - \kappa_B\right) (\nabla \cdot \bar{\mathbf{U}})^2 \quad (15)$$

In the equation of state for a perfect gas

$$P = \rho RT \quad (16)$$

where  $R$  is the gas constant, the caloric equation of state

$$e = C_v T \quad (17)$$

and the definition of static enthalpy

$$h = C_p T \quad (18)$$

supplement the equations of motion.

Finally the flow properties  $\mu$ ,  $\kappa$ , and  $K_B$  are determined using the following constitutive relations.

The molecular viscosity,  $\mu$ , is determined using Sutherland's law,

$$\frac{\mu}{\mu_0} = \left( \frac{T}{T_0} \right)^{3/2} \frac{T_0 + S_1}{T + S_1} \quad (19)$$

where  $S_1 = 100^\circ\text{K}$  for air.

The bulk viscosity is assumed to be zero

$$K_B = 0 \quad (20)$$

and the thermal conductivity is determined by use of a relation similar to Sutherland's law namely

$$\frac{\kappa}{\kappa_0} = \left( \frac{T}{T_0} \right)^{3/2} \frac{T_0 + S_2}{T + S_2} \quad (21)$$

where  $S_2 = 194^\circ\text{K}$  for air.

## DEPENDENT VARIABLES AND COORDINATE TRANSFORMATION

The governing equations, Equations (6) through (8), are written in general vector form. Prior to their application to specific problems, it is necessary to decide on both a set of dependent variables and a proper coordinate transformation. Based on previous investigations (Ref 8), the specific scalar momentum equations to be solved are the x, y, and z Cartesian momentum equations. The dependent variables chosen are the physical Cartesian velocities u, v, w, and the density  $\rho$ . If the energy equation is solved, enthalpy is added to the set of dependent variables.

The governing equations are then transformed to a general coordinate system in which the general coordinates,  $y^j$ , are related to the Cartesian coordinates,  $x_1$ ,  $x_2$ , and  $x_3$ , by

$$\begin{aligned} y^j &= y^j(x_1, x_2, x_3, t); \quad j = 1, 2, 3 \\ \tau &= t \end{aligned} \quad (22)$$

As implied by Equation 22, the general coordinate,  $y^j$ , may be a function of both the Cartesian coordinates and time. This coordinate time dependence will have an implication in so far as the choice of governing equation form is concerned.

The governing equations can be expressed in terms of the new independent variables,  $y^j$ , as

$$\begin{aligned} &\frac{\partial W}{\partial \tau} + \xi_1 \frac{\partial W}{\partial \xi} + \xi_x \frac{\partial F}{\partial \xi} + \xi_y \frac{\partial G}{\partial \xi} + \xi_z \frac{\partial H}{\partial \xi} \\ &\quad + \eta_1 \frac{\partial W}{\partial \eta} + \eta_x \frac{\partial F}{\partial \eta} + \eta_y \frac{\partial G}{\partial \eta} + \eta_z \frac{\partial H}{\partial \eta} \\ &\quad + \zeta_1 \frac{\partial W}{\partial \zeta} + \zeta_x \frac{\partial F}{\partial \zeta} + \zeta_y \frac{\partial G}{\partial \zeta} + \zeta_z \frac{\partial H}{\partial \zeta} \\ &= \frac{1}{Re} \left[ \xi_x \frac{\partial F_1}{\partial \xi} + \eta_x \frac{\partial F_1}{\partial \eta} + \zeta_x \frac{\partial F_1}{\partial \zeta} + \xi_y \frac{\partial G_1}{\partial \xi} + \eta_y \frac{\partial G_1}{\partial \eta} + \zeta_y \frac{\partial G_1}{\partial \zeta} + \xi_z \frac{\partial H_1}{\partial \xi} + \eta_z \frac{\partial H_1}{\partial \eta} + \zeta_z \frac{\partial H_1}{\partial \zeta} \right] \end{aligned} \quad (23)$$

through a straightforward application of chain rule differentiation. In Equation (23)

$$\xi = y^1$$

$$\eta = y^2$$

$$\zeta = y^3$$

and

$$W = \begin{bmatrix} \rho \\ \rho u \\ \rho v \\ \rho w \end{bmatrix} \quad F = \begin{bmatrix} \rho u \\ \rho u^2 + p \\ \rho uv \\ \rho uw \end{bmatrix} \quad G = \begin{bmatrix} \rho v \\ \rho uv \\ \rho v^2 + p \\ \rho vw \end{bmatrix}$$

$$H = \begin{bmatrix} \rho w \\ \rho uw \\ \rho vw \\ \rho w^2 + p \end{bmatrix} \quad F_1 = \begin{bmatrix} 0 \\ \tau_{xx} \\ \tau_{xy} \\ \tau_{xz} \end{bmatrix} \quad G_1 = \begin{bmatrix} 0 \\ \tau_{xy} \\ \tau_{yy} \\ \tau_{yz} \end{bmatrix} \quad H_1 = \begin{bmatrix} 0 \\ \tau_{xz} \\ \tau_{yz} \\ \tau_{zz} \end{bmatrix}$$

The governing equations have been written in this form in Ref 7 through 12; the form is termed the semistrong conservation form in Ref 23, and the chain rule conservation form in Ref 24. The metric coefficients do not appear within the derivatives. The experiences of Ref 7 through 12 show that results obtained by means of the semistrong conservation form are less sensitive to the method used to evaluate the metric coefficients than are results obtained by means of strong conservation form. The semistrong conservation form was used in this effort.

## TURBULENCE MODELING

Several alternative turbulence models have been considered in the course of this effort. In general terms, the models used were zero-, one-, and two-equation models.

### Zero-Equation Model--Mixing Length

Of all of the available turbulence models, Prandtl's mixing length model is probably still the most widely used. The model was originally developed for use in unseparated boundary layer flow situations and has been shown to perform well under such conditions. An economical advantage of the method is that it does not require additional transport equations to model the effect of turbulence, but rather relates the Reynold's shear stress to mean flow quantities by means of

$$-\overline{\rho u_i' u_j'} = \mu_T \frac{\partial U_j}{\partial x_i} \quad (24)$$

where

$$\mu_T = \rho l^2 (2D : D)^{1/2}$$

where

$$l = \min \left[ l_\infty, \kappa d D \right]$$

where  $d$  is the normal distance to the nearest wall and  $D$  is the van Driest damping coefficient given by

$$\begin{aligned} D &= 1 - \exp(-y^+/A^+) \\ l_\infty &= 0.09\delta \\ \kappa &= 0.4 \\ y^+ &= du_\tau/\nu \\ u_\tau &= (\tau_l/\rho)^{1/2} \end{aligned} \quad (25)$$

where the local shear stress  $\tau_l$  is obtained from

$$\tau_l = (2\mathbb{D}:\mathbb{D})^{1/2} \quad (26)$$

and  $\mathbb{D}$  is defined by Equation (11).

One problem in the mixing length formulation is the definition of  $\delta$ . In boundary layers the streamwise velocity,  $U$ , approaches an edge velocity,  $U_e$ , asymptotically, however a monotonic approach to an asymptotic edge velocity is not characteristic of N-S solutions. To avoid the ambiguity of determining the boundary layer edge,  $\delta$ , as defined in the usual boundary layer context, i.e.,  $\delta$  is the distance from the wall at which  $U/U_e = 0.99$ , the following relation is used

$$\delta = 2.0 d_{(q/q_{\text{MAX}} = c)} \quad (27)$$

In other words,  $\delta$ , is taken as twice the distance (measured away from the nearest wall) for which  $q/q_{\text{max}} = c$ . The value of  $c$  used in the present effort was 0.81.

The model used in the wake is also a mixing length model in which the mixing length was made proportional to the wake height,  $\delta$ , and a linear growth of  $\delta$  with distance was assumed based on the classical free jet boundary results (Ref 25). With the free jet boundary growth assumption

$$\delta = (\delta_{PS} + \delta_{SS}) + (0.2)(x - x_{TE}) \quad (28)$$

where  $\delta_{PS}$  and  $\delta_{SS}$  are the pressure and suction surface trailing edge boundary layer thickness and  $x_{te}$  is the trailing edge location. The mixing length,  $\lambda$ , was taken as  $0.2\delta$ .

### One-Equation Model--k- $\epsilon$

Although the mixing length concept is valid for a variety of flows, some important flow situations arise in which a less restrictive model is required. One such model is the one-equation turbulence model (Ref 26) in which a transport equation for turbulence kinetic energy,  $k$ , is formulated

$$\frac{\partial \rho k}{\partial t} + \nabla \cdot (\rho \bar{U} k) = \nabla \cdot \left( \frac{\mu_T}{\sigma_k} \nabla k \right) + 2\mu_T (\mathbb{D} : \mathbb{D}) - \rho \epsilon \quad (29)$$

where (following Ref 27)  $\sigma_k$  is set to 1.0, and  $k$  is the turbulence kinetic energy

$$k = \frac{1}{2} \overline{u^i \cdot u^i}$$

and the Prandtl-Kolmogorov relation, Equation (30), defines the turbulent viscosity as

$$\mu_T = C_\mu \frac{\rho k^2}{\epsilon} \quad (30)$$

In addition, the turbulence dissipation rate  $\epsilon$  is determined by

$$\epsilon = C_\mu^{3/4} \frac{k^{3/2}}{l} \quad (31)$$

where  $l$  is a relevant turbulent length scale for the problem of interest. The  $k$ - $l$  model has an advantage over the mixing length scale model in that the use of a transport equation for turbulence kinetic energy allows for its convection, production, and dissipation. This is important because it allows a nonequilibrium effect on the turbulence to be included in the calculation while the mixing length model can only account for local equilibrium turbulence effects by means of its association with the mean velocity field. A major disadvantage that the  $k$ - $l$  model shares with the mixing length model is the requirement of length scale specification. Typically the mixing length, as described previously, is used as the representative length scale.



There are two approaches to modeling the flow in the near wall region where low local turbulence Reynolds numbers occur. The first is the wall function approach that does not resolve the near wall region but assumes specific function forms for the required turbulence quantities and uses these forms to create the required normal derivative formulations at the first grid point from the wall. Such an approach obviously requires a detailed knowledge of the turbulence model dependent variables in the vicinity of the wall. Although reasonable function formulations can be specified for simple 2-D flows such as constant pressure boundary layers, specification in the much more complex flows is more difficult. Therefore, the alternative approach in which the viscous sublayer is resolved has been used. The method makes no approximation at the boundary, but requires that the near wall low turbulence Reynolds number physics be modeled. In this effort, a near wall model, which was successfully used by Shamroth and Gibeling (Ref 28) in a time-dependent airfoil flow field analysis, has been implemented in the computer code. The analysis of Ref 28 follows the integral turbulence energy procedure of Ref 26 by using a turbulence function,  $a_1$ , where

$$a_1 = \frac{1}{2} c_\mu^{1/2} \quad (32)$$

and  $a_1$  is taken as a function of a turbulence Reynolds number of the form

$$a_1 = a_o \left[ \frac{f(R_T)}{100} \right] / \left[ 1.0 + 6.66 a_o \left( \frac{f(R_T)}{100} - 1 \right) \right] \quad (33)$$

$$a_o = .0115$$

where

$$\begin{aligned} f(R_T) &= 100 R_T^{0.22} & R_T &\leq 1 \\ f(R_T) &= 68.1 R_T + 614.3 & R_T &\geq 40 \end{aligned} \quad (34)$$

and a cubic curve was fitted for values of  $R_T$  between 1 and 40. In this effort,  $R_T$  was defined as the local ratio of turbulent to laminar viscosity,  $a_1$  was evaluated by means of Equation (33) and  $c_\mu$  related to  $a_1$  by means of Equation (32). As previously discussed, Ref 26 used an integral form of the turbulent kinetic energy and, therefore,  $R_T$  was defined as an average value.

$$R_T = \frac{1}{\delta} \int_0^\delta v_T dy / \frac{1}{\delta} \int_0^\delta v dy_s \quad (35)$$

#### Two-Equation Model--k-ε

Although the one-equation approach does relieve some restrictions in the mixing length approach, it still requires specification of a length scale. The k-ε, two-equation turbulence model (Ref 29 and 30), in which both the turbulence kinetic energy and the turbulence dissipation rate are governed by transport equations, represents a more general model. In this approach, the k-equation is as given in Equation (29), but the algebraic relation for ε given by Equation (31) is replaced by the following transport equation.

$$\frac{\partial \rho \epsilon}{\partial t} + \nabla \cdot (\rho \bar{U} \epsilon) = \nabla \cdot \left( \frac{\mu_T}{\sigma_\epsilon} \nabla \epsilon \right) + C_1 (2\mu_T \mathbb{D} : \mathbb{D}) \frac{\epsilon}{K} + 2\mu_T (\nabla^2 U)^2 - C_2 \rho \frac{\epsilon^2}{K} \quad (36)$$

However, attempts to solve Equations (29) and (36) without modification present problems because an appropriate boundary condition for ε at a solid boundary is difficult to prescribe such that Equation (36) is satisfied. Following the suggestion of Jones and Launder (Ref 27), the turbulence dissipation equation has been modified by the inclusion of the term

$$- 2\mu_T (\nabla^2 U)^2$$

in the energy dissipation equation, Equation (36), and by the inclusion of the term

$$- 2\rho \nu (\nabla K^{1/2})^2$$

in the turbulence energy equation which then becomes

$$\frac{\partial \rho K}{\partial t} + \nabla \cdot (\rho \bar{U} K) = \nabla \cdot \left( \frac{\mu_T}{\sigma_K} \nabla K \right) + 2\mu_T (\mathbb{D} : \mathbb{D}) - \rho \epsilon - 2\rho \nu (\nabla K^{1/2})^2 \quad (37)$$

These additional terms allow an  $\epsilon = 0$  wall boundary condition to be applied and appear to correctly model the near wall region as discussed in Ref 27.

Following Ref 27, the following empirical relations are used

$$\sigma_{\epsilon} = 1.3$$

$$\sigma_k = 1.0$$

$$C_1 = 1.43$$

$$C_{\mu} = 0.09 \exp \left[ -2.5 / (1 + R_{\tau} / 50) \right]$$

$$C_2 = 1.92 \left[ 1.0 - 0.3 \exp (-R_{\tau}^2) \right]$$

and  $R_{\tau}$  is defined as

$$R_{\tau} = \frac{\rho k^2}{\mu \epsilon}$$

The turbulent eddy viscosity is evaluated by Equation (30).

## BOUNDARY CONDITIONS

Boundary conditions play an important role in determining accurate solutions and rapid numerical convergence when solving N-S equations. The boundary conditions used in these calculations follow the suggestion of Briley and McDonald (Ref 31), which specifies upstream total pressure and downstream static pressure conditions. For the 2-D cascade system shown in Figure 2, BC and ED are periodic boundaries and periodic conditions are set here.

Specification of upstream and downstream conditions is somewhat more difficult. For an isolated cascade, boundary conditions for the differential equations may be known at both upstream infinity and downstream infinity. However, since computation economics argues for placing grid points in the vicinity of the cascade and minimizing the number of grid points far from the cascade, the upstream and downstream computational boundaries should be set as close to the cascade as is practical. In addition, with the particular body-fitted coordinates used, as the upstream boundary moves further upstream, the angle between pseudoradial and pseudoazimuthal coordinate lines becomes smaller. Decreasing

the coordinate angle causes the coordinate system to become less well-conditioned, increases truncation error (Ref 32), and increases the role of cross-derivative terms in the equations. All of these characteristics could be detrimental to the present numerical procedure and, therefore, they also argue for placing the upstream boundary as close to the cascade as possible. However, when the upstream boundary is placed close to the cascade, most flow function conditions on the boundary will not be known, because these will have been changed from values at infinity by the presence of the cascade.

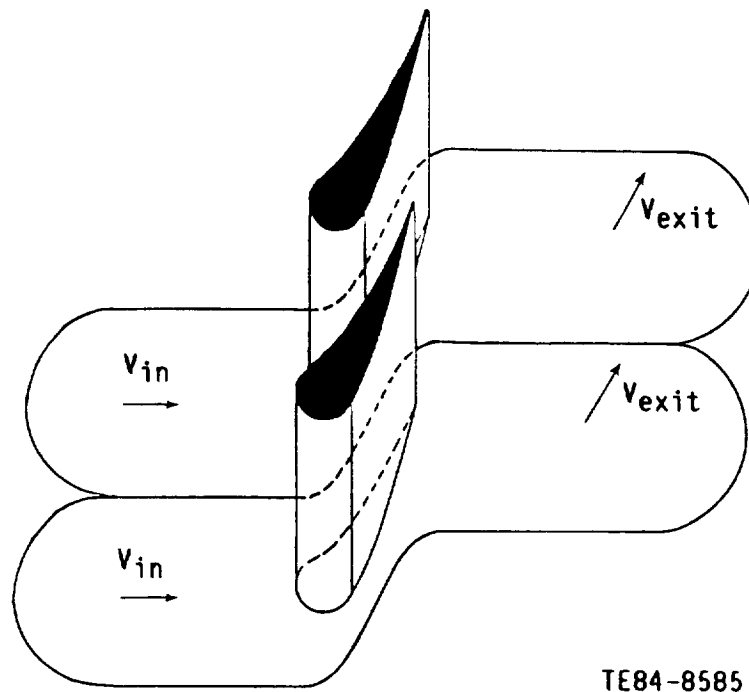
In this effort, total pressure is set on boundary CC'D, shown in Figure 2 (Ref 31). Unless boundary CC'D is very far upstream, the flow velocity along this boundary will not be equal to the velocity at upstream infinity because some inviscid deceleration will have occurred. However, as long as the boundary is upstream of the region of any significant viscous or shock phenomena, the total pressure on this boundary will be equal to the total pressure at upstream infinity. Hence, total pressure is an appropriate boundary condition realistically modeling the desired flow condition. In addition to specifying upstream total pressure, it is necessary to specify the inlet flow angle. In these calculations, a value was assumed constant on the upstream boundary at a specified value, although it is possible that in future studies the inflow angle distribution could be obtained from an inviscid calculation. The third condition set on the upstream boundary concerns the density. A zero density derivative at this boundary was specified as a numerical treatment of the boundary.

The downstream boundary EAB is considered to be far away from the blade surface. A small portion of the boundary may contain inlet flow depending on the turning of the passage flow. For this inlet flow portion, the flow variables were set equal to those at the end of the periodic line, e.g. at point E in Figure 2. For outflow portion, the boundary was treated by setting a constant static pressure as a boundary condition, and by extrapolating (first derivatives) both velocity components along exit flow direction at this location. In the present application, a constant static pressure was set at downstream infinity, and hence it is assumed that the downstream boundary is located in a region where pressure is uniform.

Both the upstream and downstream boundaries have boundary conditions that are nonlinear functions of the dependent variables associated with them. These conditions are the specifications of total pressure on the upstream boundary and static pressure on the downstream boundary. These nonlinear boundary conditions are linearized in the same manner as the governing equations (by means of a Taylor expansion of the dependent variables in time), and then solved implicitly along with the interior point equations. No-slip conditions (except the film cooling option) together with zero pressure gradient were set at solid walls. If film cooling is applied on the blade surface, a wall velocity is specified by means of input for the portion of that surface.

For a three-dimensional (3-D) rectilinear cascade configuration, which consists of a turbine cascade situated in the azimuthal-radial plane and bounded in the transverse direction by an endwall and a symmetry plane (see Figure 6), the incoming flow at the upstream boundary is in boundary layer form due to the endwall and not a uniform stream as in the 2-D unbounded cascade. A two-layer velocity profile condition in place of a uniform velocity profile condition was set at the upstream boundary. The so-called two-layer model (Ref 31) used at the inflow boundary is essentially a total pressure boundary condition applied to the core flow with a specified boundary layer profile shape for the wall region. Matching the static pressure at the edge, defined by the first computational point from the wall at which  $|u|/|u|_{\max}$  was greater than or equal to 0.99 on the previous time step, enables calculation of  $|u|$  at this point. This calculation provides the required normalizing value for the pre-specified boundary layer profile shape. Overall, the method provides a mechanism for drawing mass flow to satisfy the downstream pressure given an upstream core total pressure while maintaining a given inlet endwall boundary layer shape. This specification corresponds to a wind tunnel experiment where stagnation conditions are set in an upstream reservoir and static pressure is set at some downstream location. No-slip conditions in conjunction with zero pressure gradient were set on the endwall. Symmetry boundary conditions were applied on the symmetry plane. The other necessary boundary conditions were treated the same as those for the 2-D case.

The present formulation contains several important advantages over alternative formulations. Specification of upstream total pressure and downstream static



TE84-8585

Figure 6. Three-dimensional C3X cascade with endwall.

pressure allows the flow to develop in a natural manner with no need to specify the velocity magnitude on the upstream boundary. Proper specification of the velocity magnitude on the upstream boundary may be difficult for 2-D cases and is difficult in transonic cascades and/or 3-D cascades. In addition, specification of no-slip conditions at solid surfaces eliminates the problem of specifying a wall function. Although wall functions may be appropriate for relatively simple 2-D flow, their use becomes questionable for 2-D separated flows. In 3-D flows, near wall flows are not well described by such universal laws and, consequently, their use in these cases does not seem appropriate, particularly if heat transfer or loss information is required. Use of the no-slip condition along with proper resolution of the boundary layer does not hinder convergence properties of the numerical method.

#### NUMERICAL PROCEDURE

The numerical procedure used to solve the governing equations is a consistently split LBI scheme originally developed by Briley and McDonald (Ref 13). A scheme similar in concept has been developed for 2-D magnetohydrodynamic problems by Lindemuth and Killeen (Ref 33) as discussed in Ref 13 and 34. The method can be outlined briefly as follows: the governing equations are replaced by an

implicit time difference approximation, either a backward difference or Crank-Nicolson scheme. Terms involving nonlinearities at the implicit time level are linearized by Taylor expansion in time about the solution at the known time level, and spatial difference approximations are introduced. The result is a system of multidimensional coupled (but linear) difference equations for the dependent variables at the unknown or implicit time level. To solve these difference equations, the Douglas-Gunn (Ref 35) procedure for generating alternating direction implicit (ADI) schemes as perturbations of fundamental implicit difference schemes is introduced in its natural extension to systems of partial differential equations. This technique leads to systems of coupled linear difference equations with narrow block-banded matrix structures, which can be solved efficiently by standard block-elimination methods.

The method centers around the use of a formal linearization technique adapted for the integration of initial-value problems. The linearization technique, which requires an implicit solution procedure, permits the solution of coupled nonlinear equations in one space dimension (to the requisite degree of accuracy) by a one-step noniterative scheme. Because no iteration is required to compute the solution for a single time step, and because only moderate effort is required for the solution of the implicit difference equations, the method is computationally efficient. This efficiency is retained for multidimensional problems by using block ADI techniques. The method is also economical in terms of computer storage, requiring only two time levels of storage for each dependent variable. In addition, the block ADI technique reduces multidimensional problems to sequences of calculations that are one-dimensional (1-D) in the sense that easily-solved narrow block-banded matrices associated with 1-D rows of grid points are produced. A more detailed discussion of the solution procedure as discussed by Briley, Buggeln, and McDonald (Ref 36) is given in Appendix A.

#### ARTIFICIAL DISSIPATION

Due to frequent high Reynolds numbers typical of normal turbomachinery applications, it is necessary to suppress spatial oscillations associated with central spatial difference approximations. Such suppression can be achieved by means of a dissipative spatial difference formulation (e.g., one-sided difference

approximations for first derivatives) or by explicitly adding an additional dissipative-type term. For the N-S equations, the latter approach has been selected because when an additional term is explicitly added, the physical approximation being made is clearer than when dissipative mechanisms are contained within numerical truncation errors. Explicit addition of an artificial dissipation term also allows greater control over the amount of nonphysical dissipation being added. The most desirable technique would add only enough dissipative mechanism to suppress oscillations without deteriorating solution accuracy. Various methods of adding artificial dissipation were investigated in Ref 11, and these methods were evaluated in the context of a model 1-D problem containing a shock with a known analytic solution (1-D flow with heat transfer). The methods that were considered included second-order dissipation, fourth-order dissipation, and pressure dissipation techniques.

As a result of this investigation, it was concluded that a second-order anisotropic artificial dissipation formulation suppressed spatial oscillations without adversely impacting accuracy and could be used to capture successfully the nearly normal shocks that are expected in transonic cascades. In this formulation the terms

$$\rho \frac{\partial}{\partial x} \left( d_x \frac{\partial \phi}{\partial x} \right), \quad \rho \frac{\partial}{\partial y} \left( d_y \frac{\partial \phi}{\partial y} \right)$$

are added to the governing equations where  $\phi = u, v, h$ , and  $\rho$  for the x-momentum, y-momentum, energy, and continuity equations, respectively. The exponent  $n$  is zero for the continuity equation and unity for the momentum and energy equations. The dissipation coefficient  $d_x$  is determined as follows. The general equation has an x-direction convective term of the form  $a \partial \phi / \partial x$  and an x-direction diffusion term of the form  $\partial(b \partial \phi / \partial x) / \partial x$ . The diffusive term is expanded

$$\partial(b \partial \phi / \partial x) / \partial x = b \partial^2 \phi / \partial x^2 + \partial b / \partial x \partial \phi / \partial x \quad (38)$$

and then a local cell Reynolds number,  $Re_{\Delta x}$ , is defined for the x-direction by



$$Re_{\Delta x} = \left| \sigma - \partial b / \partial x \right| \Delta x / b \quad (39)$$

where  $b$  is the total or effective viscosity including both laminar and turbulent contributions and  $\Delta x$  is the grid spacing. The dissipation coefficient  $d_x$  is not negative and is chosen as the larger of zero and the local quantity  $b (\sigma_x Re_{\Delta x} - 1)$ . The dissipation parameter  $\sigma_x$  is a specified constant and represents the inverse of the cell Reynolds number below which no artificial dissipation is added. The dissipation coefficient  $d_y$  is evaluated in an analogous manner and is based on the local cell Reynolds number  $Re_{\Delta y}$  and grid spacing  $\Delta y$  for the  $y$ -direction and the specified parameter  $\sigma_y$ .

The question arises as to which values of  $\sigma_x$  and  $\sigma_y$  should be chosen. This question was assessed both through the model problem (Ref 11), and through calculations for a Jose Sanz compressor cascade (Ref 7 and 11). These results indicated that values of  $\sigma = 0.5$ , which corresponds to a cell Reynolds number 2 limitation, would severely damp physical variations. However, when  $\sigma$  was set in the range  $0.025 \leq \sigma \leq 0.05$ , which corresponds to a cell Reynolds number range between 40 and 20, spurious spatial oscillations were damped with no significant change in the calculated results as  $\sigma$  was varied in this range. As discussed in Ref 7 through 11, the results showed good agreement with data. This agreement has since been confirmed at several other studies at Scientific Research Associates (SRA) such as 2-D and 3-D transonic nozzle flows (Ref 37) where a maximum acceptable value of  $\sigma = 0.10$  has been noted for most problems. In cases where spatial resolution may be marginal, such as at the leading edge of a relatively sharp edged blade, it may be necessary to increase  $\sigma$  in this local area. However,  $\sigma$  can be decreased to 0.10 or below if computational grid points are added in this region.

#### IV. TEST CASES AND RESULTS

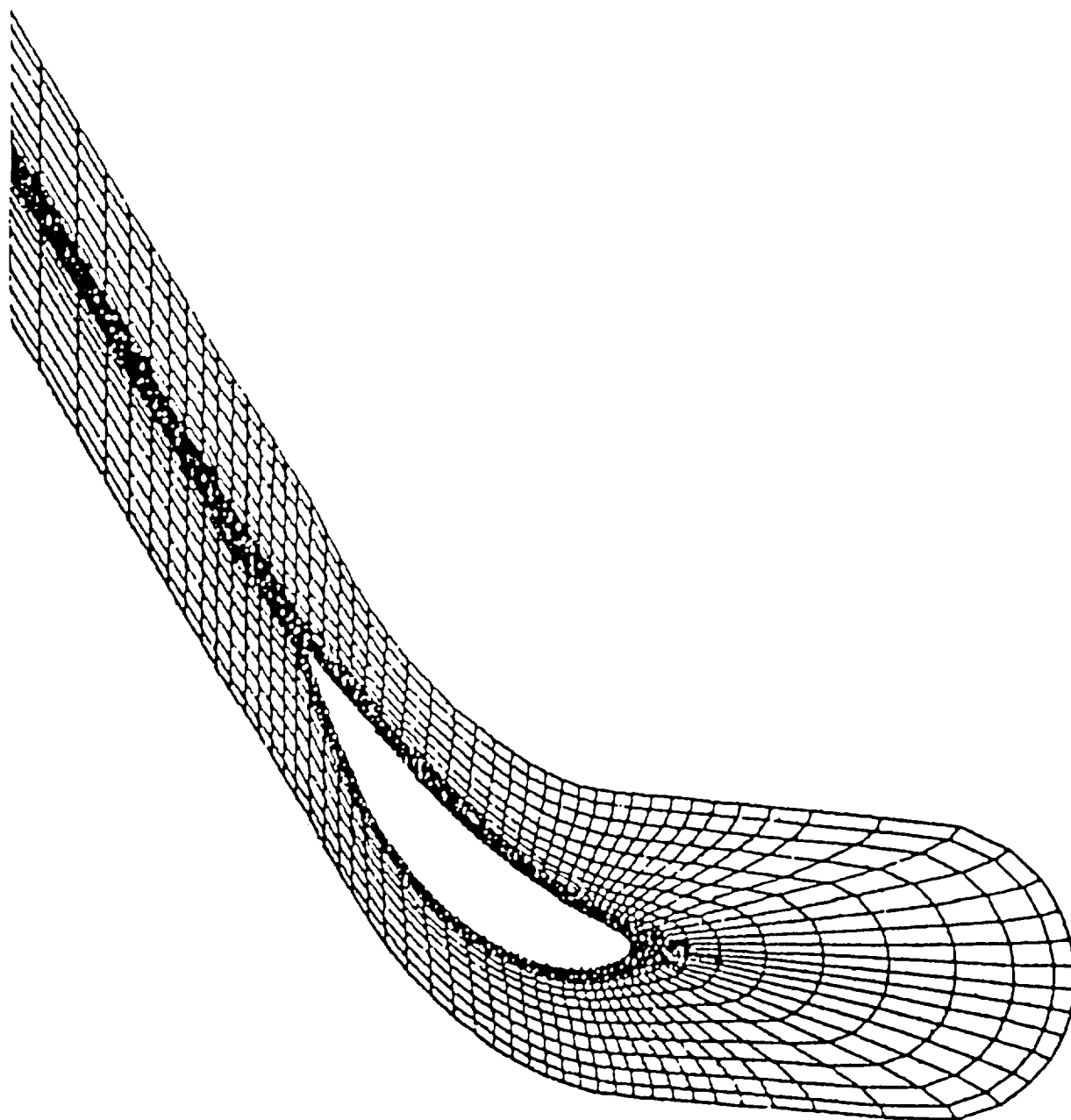
Several test cases were run to demonstrate and assess the computer code for the Navier-Stokes (N-S) analysis. The first case examined the two-dimensional (2-D) Turner turbine cascade (Ref 21). The second case examined the 2-D low solidity C3X turbine cascade (Ref 22). The final case considered was a three-dimensional (3-D) rectilinear C3X cascade.

##### CASE 1--2-D TURNER TURBINE CASCADE

To assess the impact of the new O-type grid on the calculated turbine cascade flow fields, a series of N-S computations were run for the Turner cascade with a rounded trailing edge. The Turner O-type grid is shown in Figure 4 and contains no approximations in the trailing edge geometry. The results of these calculations were compared with the results obtained with the C-type grid for the Turner case with a cusped trailing edge (Figure 7) under the same flow conditions. As shown in Figure 1, the cusp is added by increasing the chord to keep as much of the geometry exact as practical.

The C-type coordinate system, shown in Figure 7, consists of 30 points in the pseudoradial direction and 113 points in the pseudoazimuthal direction. The periodic boundary is extended 0.75 chords upstream of the leading edge. The O-type coordinate system, shown in Figure 4, consists of 30 points in the pseudoradial direction and 100 points in the pseudoazimuthal direction. The periodic boundary is extended 0.9 chords upstream of the leading edge and 1.0 chords downstream of the trailing edge, respectively. The first coordinate line off the airfoil is placed at approximately  $4 \times 10^{-5}$  chords from the surface for both C- and O-type coordinate systems, thus obtaining adequate boundary layer resolution. The geometric inlet angle for the Turner cascade is approximately 0 deg and the geometric exit angle is approximately 62 deg. The blade pitch to chord ratio is approximately 0.65 and the blade shape has a relatively large radius of curvature at the leading edge.

The first flow considered was assumed to be subsonic, laminar, and at constant total temperature. The calculation was run with a free-stream Reynolds number based on chord and inlet conditions of approximately 400 and a ratio of inlet



TE84-8586

Figure 7. C-type coordinate system for Turner cascade.

total pressure to exit static pressure of approximately 1.25. The calculations were initiated by assuming uniform flow with a boundary layer correction on the airfoil surface. With these initial conditions, it took about 80 time steps to reach converged solutions for both C- and O-type coordinate systems. In all cases, convergence was monitored by noting the decrease in maximum flow field residual. Based on previous experience, the solution can be considered converged when the maximum residual has decreased by three orders of magnitude from its initial value and only small changes are occurring in the calculated pressure and velocity distributions for a range of time step sizes. In Figure 8, the pressure coefficient of the two coordinate systems is compared. The C-type grid blade is longer due to the cusped trailing edge. The results are in excellent agreement for both the suction and pressure surfaces except in the vicinity of the trailing edge, which is not unexpected in light of the different trailing edge geometries for the two calculations.

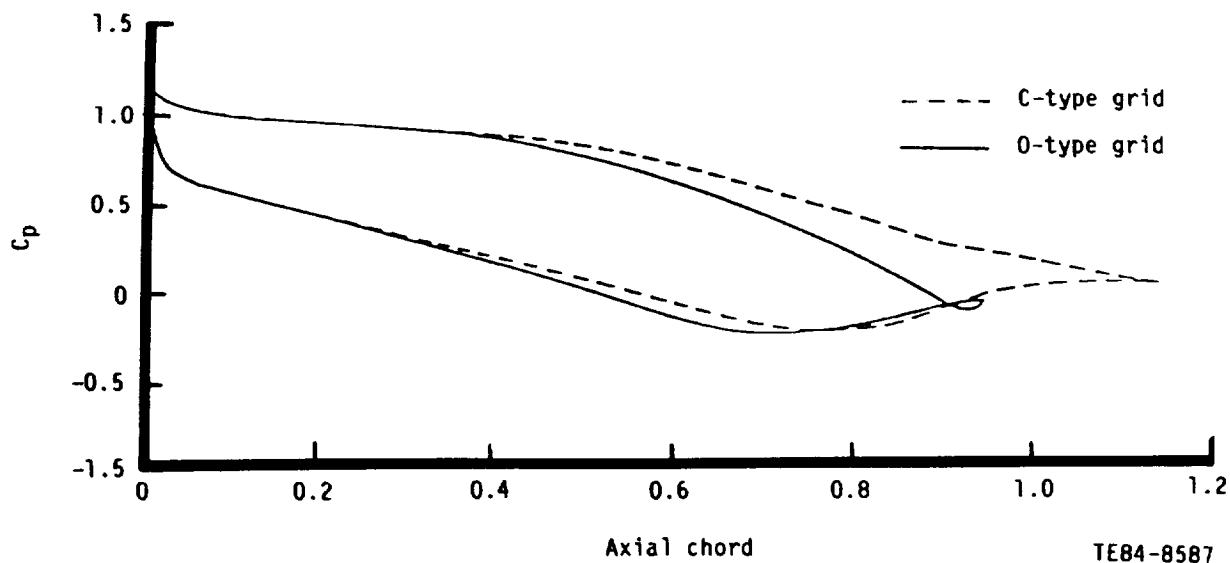


Figure 8. Pressure coefficients distribution of the subsonic laminar cascade.

The second flow considered was similar to the laminar one except the free-stream Reynolds number based on chord and inlet conditions was approximately  $0.527 \times 10^6$  and the flow was assumed to be turbulent. Using the convergent solution obtained from the laminar flow calculation as the initial condition and the mixing length turbulence model, 60 time steps were required to reach a converged solution. Good agreement was obtained for the turbulent subsonic case as can be seen in Figure 9.

The final flow considered was a transonic turbulent flow corresponding to Turner's experiment (Ref 21). The free-stream Reynolds number based on chord and inlet conditions was approximately  $0.884 \times 10^6$  and the ratio of the inlet total pressure to the exit static pressure was approximately 1.778. Total temperature was assumed to be constant in the flow field. The calculations used the solution of the turbulent subsonic case as the initial condition, then the inlet total to exit static pressure ratio was increased linearly from 1.25 to 1.778 within 15 time steps. Using the mixing length turbulence model, convergent solutions were obtained within about 80 time steps for both coordinate

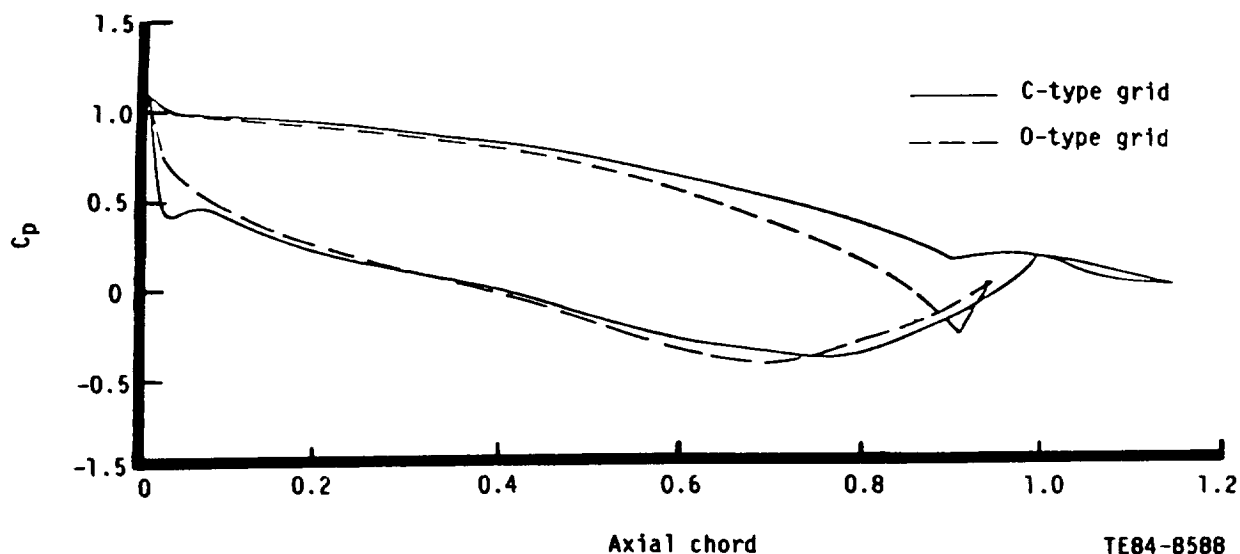


Figure 9. Pressure coefficients distribution of the subsonic turbulent cascade.

systems. In Figure 10, the surface pressure distribution (in terms of velocity ratio) for the two calculations is compared with the data of Turner (Ref 21). Both calculations are comparable with one another over the entire airfoil and both agree with the data over most of the surface except near the trailing edge. In view of the excellent agreement between the two calculations, it is concluded that the discrepancy between the measured data and C-type grid calculations originally noted in Ref 7 are not due to the approximated trailing edge geometry in the C-type grid calculation. In addition, the calculation confirms the operation of the N-S code in the O-type grid mode.

An inspection of Figure 10 reveals that both the O- and C-type grid calculations underpredict the pressure in a similar manner in the region of 60-80% chord on the suction surface. There are several possible sources for this discrepancy. Computationally, the turbulence transition model could give rise to the observed differences. Experimentally, one possible source could be endwall effects changing the axial velocity density ratio (AVDR) from unity. If this change were to occur, it would be particularly important at transonic speeds when the flow field becomes sensitive to the effective area ratio and neglect of a nonunity AVDR could lead to significant discrepancies. In view of the absence of endwall effect discussion in Ref 21, which focused primarily on transitional boundary layers, it is difficult to assess the actual source of the discrepancy. Because the intent of this effort was to verify the suitability of the O-type grid, no further investigation of this question was undertaken.

#### CASE 2--2-D C3X TURBINE CASCADE

The coordinate system for the C3X turbine cascade is shown in Figure 5. This O-type grid consists of 30 points in the pseudoradial direction and 120 points in the pseudoazimuthal direction. In keeping with the objectives of the construction procedure, the minimum coordinate intersection angle is 20 deg and the upstream boundary is placed at 2.25 axial chords upstream of the leading edge and the downstream boundary is placed at 2.65 axial chords downstream of the trailing edge. High radial resolution is obtained near the surface of the blade, and the first coordinate line is located at a distance of  $1.0 \times 10^{-6}$  axial chords from the surface. In addition, high pseudoazimuthal resolution

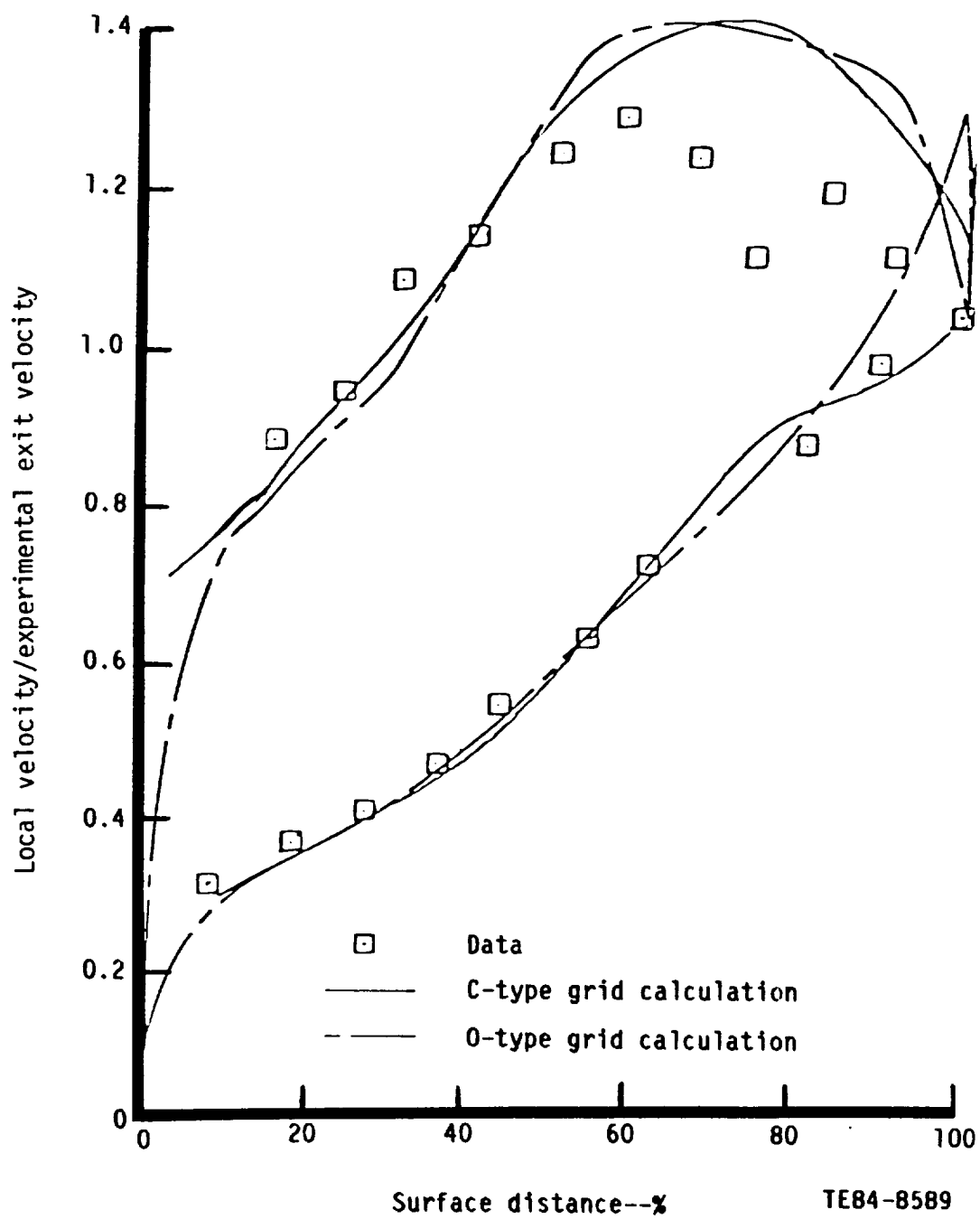


Figure 10. Turner cascade pressure distribution of the transonic case.

is obtained in both leading and trailing edge regions. The C3X cascade geometry is given in detail in Ref 22. The geometric inlet angle is approximately 0 deg and the geometric exit angle is approximately 72 deg. The vane spacing to axial chord ratio is approximately 1.5. The true chord to axial chord ratio is approximately 1.85.

The first flow examined corresponded to case 143 in Ref 22 in which the inlet Mach number,  $Ma_1$ , was 0.17, the exit Mach number,  $Ma_{exit}$ , was 1.05, the inlet Reynolds number based on true chord,  $Re_1$ , was  $0.63 \times 10^6$ , and the estimated ratio of inlet total to exit static pressure,  $P_t/P_{exit}$ , was 2.0. The exit data given in Ref 22, i.e., the average Mach number downstream of the trailing edge, is not suitable for specifying boundary conditions at the downstream boundary of the computational domain as required by the N-S procedure (2.65 axial chords downstream of the trailing edge). In this computational domain, the flow is subsonic at the rear cap. Thus a static exit pressure can be specified. However, a sensitivity study of the effect of  $P_t/P_{exit}$  on surface pressure distribution was undertaken, where  $P_t$  is the upstream stagnation pressure, and  $P_{exit}$  is the static pressure at the downstream boundary of the computational domain. Two values of  $P_t/P_{exit}$  were chosen, 1.9 and 2.0. Constant total temperature was assumed in the calculation. The computed pressure distribution is shown in Figure 11 and is compared with the Allison experimental data (Ref 22) and the inviscid predictions (Ref 1) due to Delaney.

Figure 11 indicates that the pressure distributions on the pressure side of the turbine blade and the forward portion of the suction side are relatively insensitive to  $P_t/P_{exit}$ . However, the pressure distribution on the aft portion of the suction side is sensitive to the pressure ratio, in that a 5% change in  $P_t/P_{exit}$  results in a commensurate pressure variation on the blade's surface. Such behavior is not unexpected because the flow through the cascade is in the transonic regime and indicates a need for definitive specification of boundary conditions if a data comparison is to be made.

Mixing length and two-equation  $k-\epsilon$  turbulence modeling were employed in the calculation, and the results of the calculations indicate little difference in the prediction of the pressure coefficient. The study of the interaction between shock wave and boundary layer in the transonic flow field was not



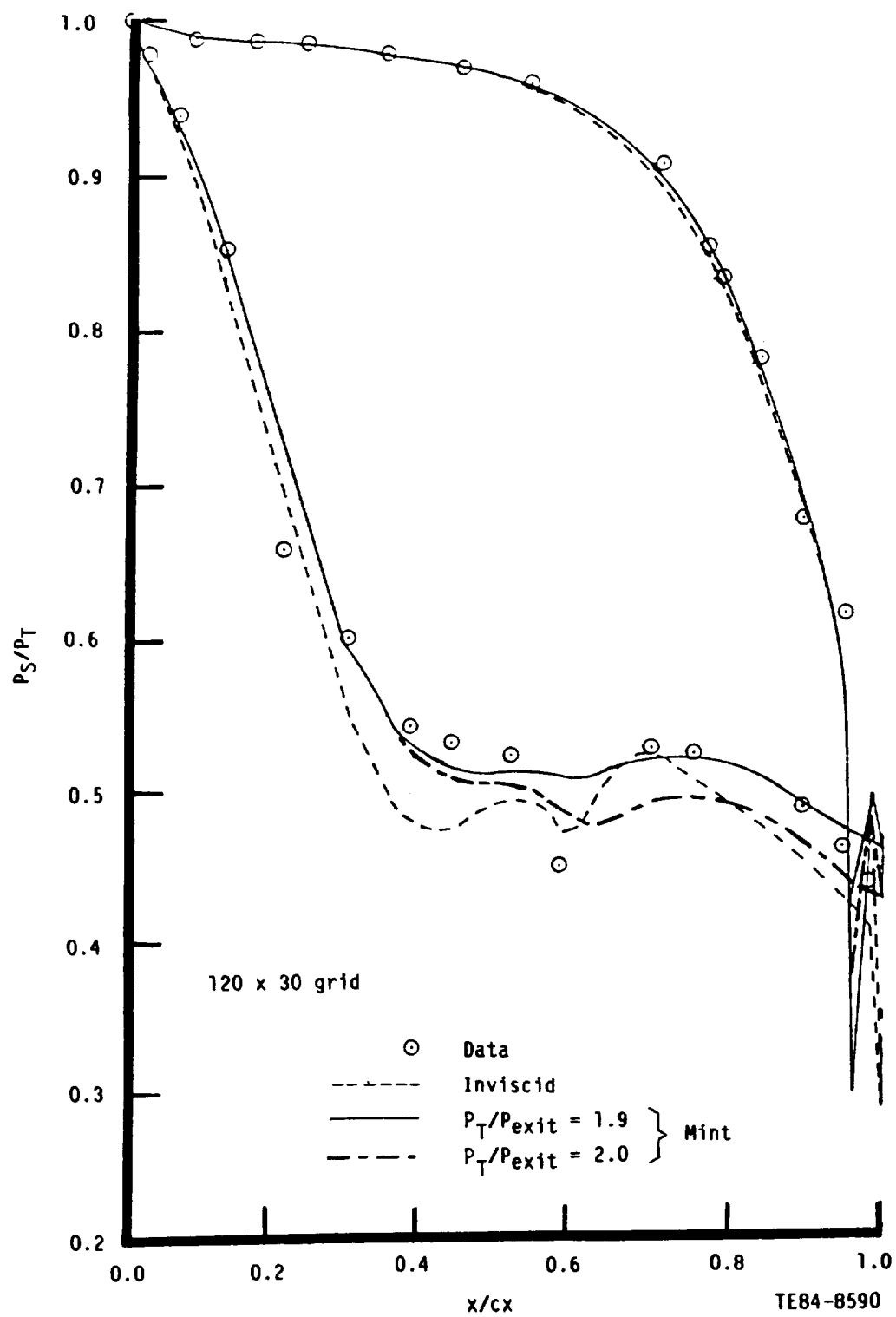


Figure 11. Comparison of measured and calculated pressure distribution of the C3X cascade.

pursued. The mechanism of the transonic shock wave and boundary layer interactions were reported recently by Roscoe, et al (Ref 38).

The second flow considered was case 144 in Ref 22. In this case, heat transfer effects were included in the calculation. The flow conditions were as follows: the inlet Mach number,  $Ma_1$ , was 0.16, the inlet total temperature,  $T_t$ , was 815°K, the exit Mach number,  $Ma_2$ , was 0.9, the exit Reynolds number based on true chord,  $Re_2$ , was  $2.43 \times 10^6$ , the estimated  $P_t/P_{exit}$  was 1.66, and the free-stream turbulence intensity,  $Tu$ , was 6.5%. The surface temperature distribution of the turbine blade is shown in Figure 12. The solid line in the figure represents the actual surface temperature used in the calculation and the dot symbol represents the data given in Ref 22. The boundary conditions for the energy equation, Equation (8), are specified as follows: total temperature is held constant at the upstream inlet; surface temperature distribution is specified through input by means of Figure 12; conditions on periodic and downstream boundaries are treated similarly to other variables at the same boundaries. When compared with the Allison experimental data and inviscid predictions in Figure 13, the calculations indicate excellent agreement. To indicate the relationship between the predictions and the experimental scatter, data from cases 148 and 158 are also shown in Figure 13. The inviscid pressure calculations show close agreement with the computed N-S results. Close agreement was expected because this is an on-design case in which viscous displacement effects are expected to be small. Significant discrepancies would be expected at off-design conditions. Three turbulence models were employed; these

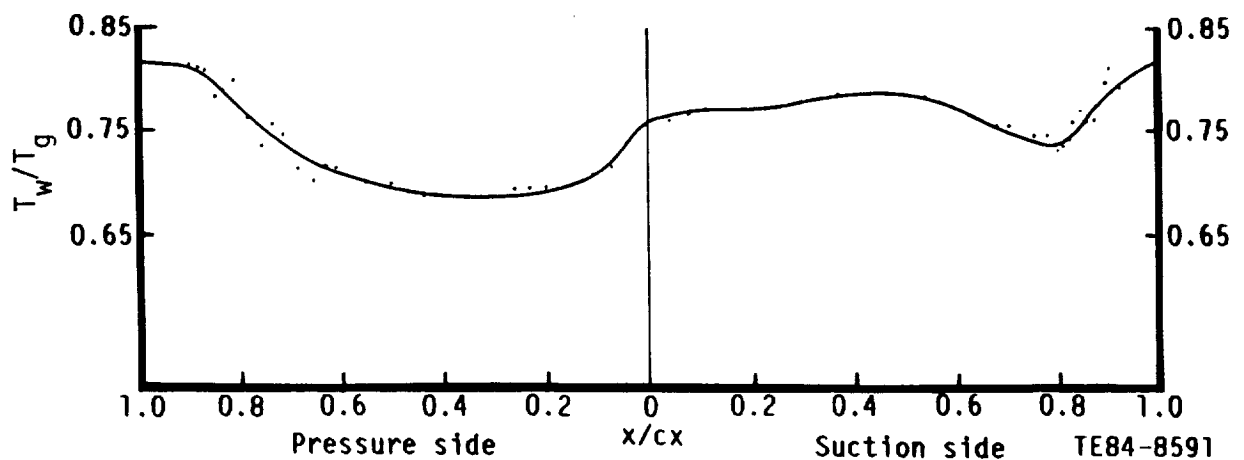


Figure 12. Surface temperature distribution for case 144.

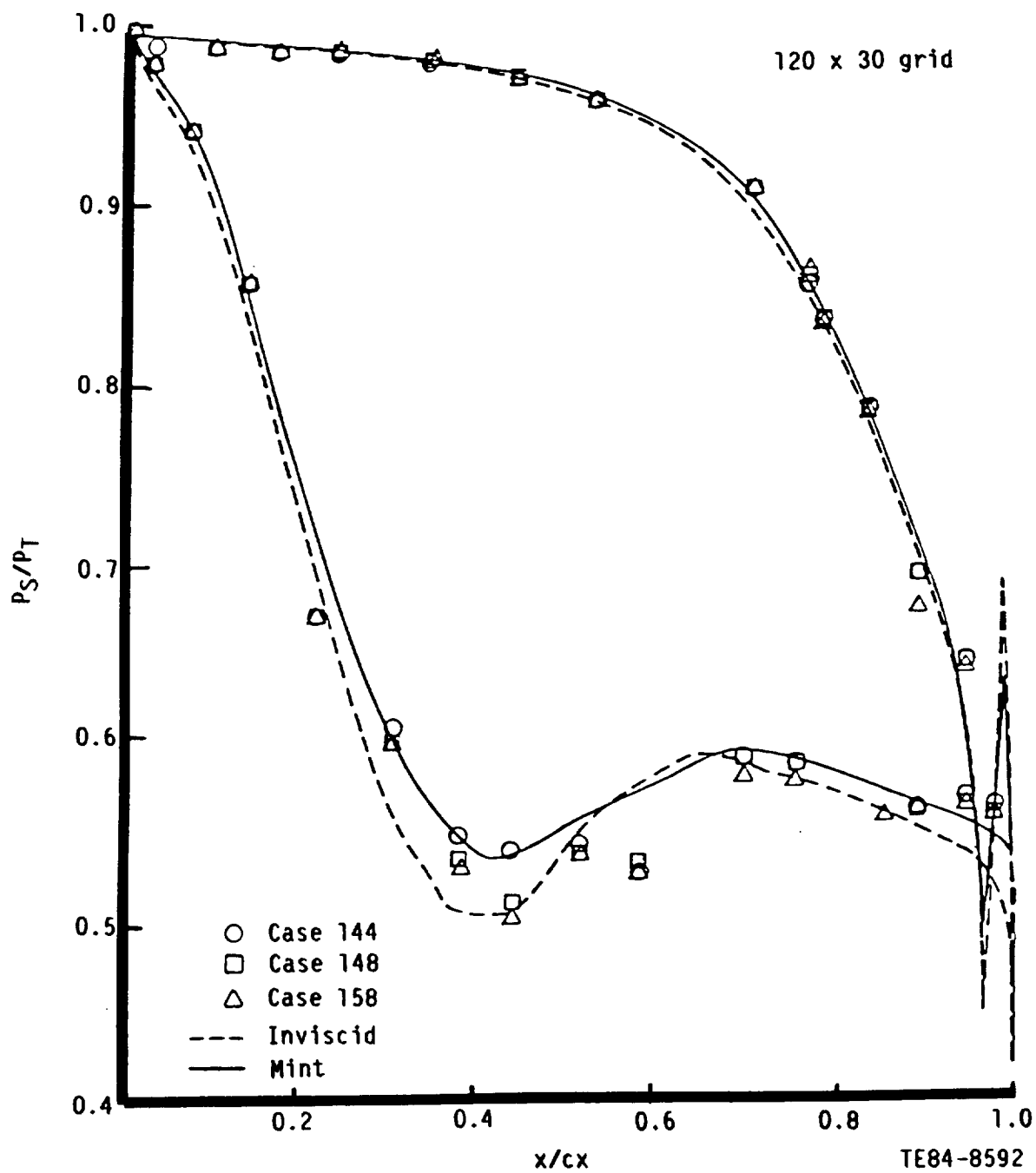


Figure 13. Comparison of measured and calculated pressure distributions of the C3X cascade for cases 144, 148, and 158.

were a mixing length model, a  $k-\epsilon$  one-equation model, and a  $k-\epsilon$  two-equation model. Computed results based on these three models show little difference in the pressure distribution. A vector velocity plot is presented in Figure 14. The turning of the flow as it passes through the cascade is evident. The flow turning (the exit angle) is predicted by the analysis rather than being an input item. The flow acceleration as it passes through the cascade is also shown as is the stagnation region and the wall boundary layer development.

The energy equation was coupled with momentum equations during this calculation. In these calculations, the laminar Prandtl number,  $Pr$ , was set to 0.73 and the effective turbulent Prandtl number,  $Pr_t$ , was set to 0.9. Addition of the energy equation to the governing set made little difference to the calculated pressure distribution, however it allows the calculation of the surface heat transfer coefficient. Surface heat transfer prediction on a turbine blade

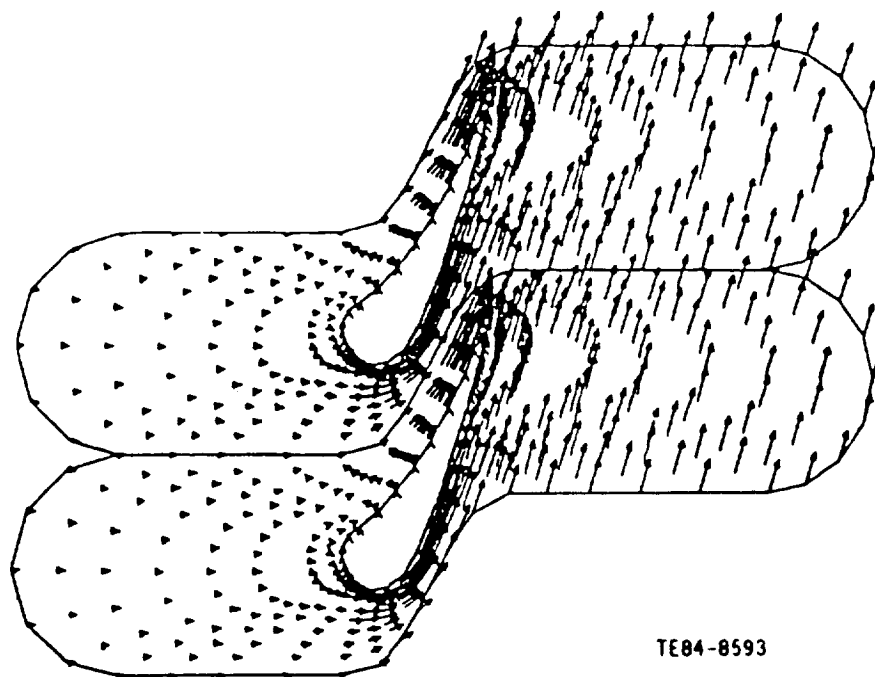


Figure 14. Vector plot for C3X cascade, case 144.

represents a stringent test due to the flow field character. The turbine passage flow field starts from laminar at upstream and then undergoes transition and becomes fully turbulent. The calculation of the transitional behavior represents a difficult factor in the prediction for the heat transfer coefficient. Two cases were considered in employing a mixing length turbulence model; fully turbulent flow and transitional flow in the stagnation region. As can be seen in Figure 15, the fully turbulent flow case overpredicts the heat transfer coefficient particularly in the stagnation zone. In view of this behavior, a transition model was incorporated to investigate the effects on heat transfer. Laminar flow was assumed in the region where  $x/c_x$  is less than 0.2, followed by a transitional zone based on the correlation of Dhawan and Narasimha (Ref 39), and thereafter by fully turbulent flow. The predictions obtained with this simple model compare well with the experimental data.

Although this empirical transition model has given good agreement with data, models containing less empiricism would be desirable. One such model, which has been used successfully for a variety of transitional flows, is the model

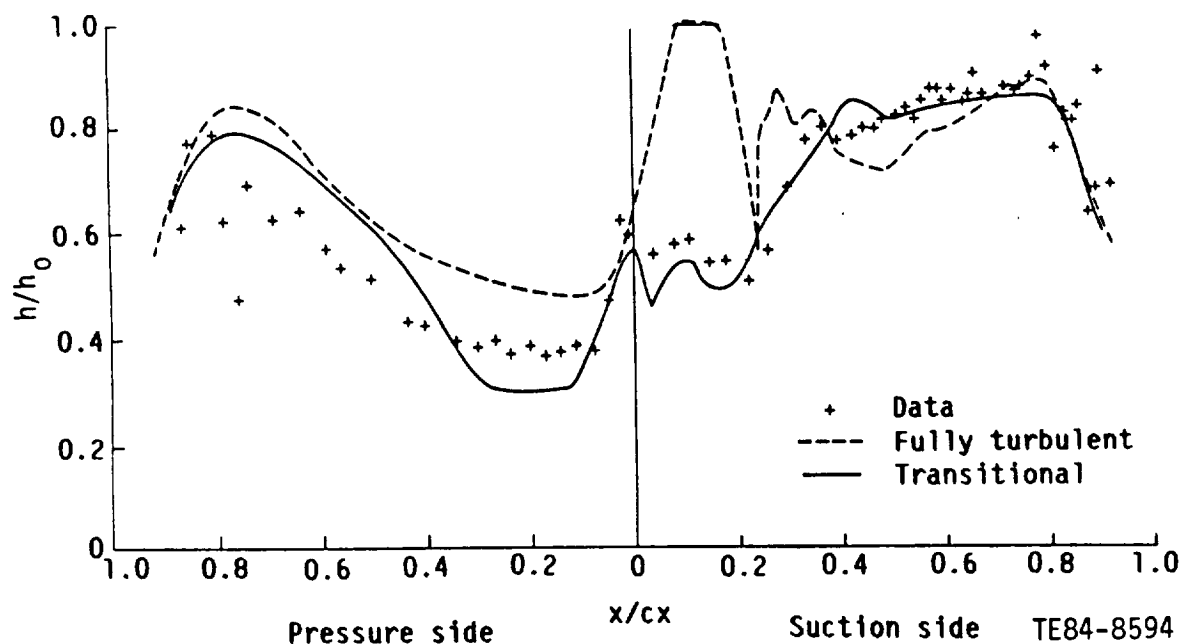


Figure 15. Comparison of measured and calculated heat transfer coefficient distributions of the C3X cascade.

of McDonald and Fish (Ref 26), which is based on an integral turbulence energy equation and has been used in conjunction with a finite difference boundary layer analysis. This model has been generalized from the integral equation formulation to the full partial differential equation formulation by Shamroth and Gibeling (Ref 28) and incorporated in the N-S code.

This K- $\epsilon$  model predicts the transport history of the turbulence kinetic energy and includes the effect of free-stream turbulence. Although this model has not been thoroughly tested under this effort, it may represent a promising approach to transitional calculations and is under study by SRA personnel.

The final 2-D flow considered was case 144 with the film-cooling option. For purposes of calculation, it was assumed that air was injected at 30 deg to the suction side over  $0.8 < x/cx < 0.9$  at a velocity of 7% of free stream and the local surface temperature of the blade was kept fixed at the same value as the nonblowing option. A mixing length turbulence model in conjunction with the transition model used in the nonfilm-cooling option for case 144 was employed in the calculation. In Figure 16 the distribution of the computed heat transfer coefficient is depicted for both film-cooling and nonfilm-cooling options.

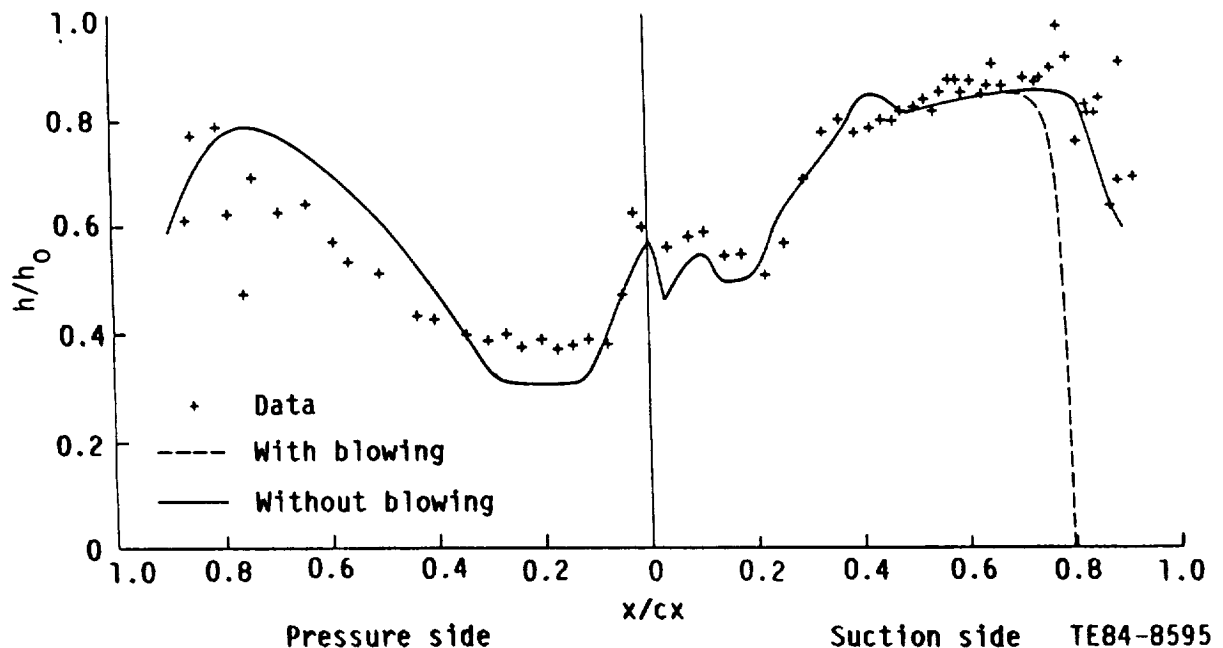


Figure 16. The effect of film cooling on heat transfer coefficient distributions.

The symbol + in the figure indicates the experimental data for the nonfilm-cooling case. As can be seen in Figure 16, the heat transfer rate drops to nearly zero from the onset of the injection to the trailing edge. This behavior is a consequence of the buffer region of constant temperature cool gas, which protects the blade surface from the hotter fluid in the cascade passage. The comparison of the pressure distribution for both film-cooling and nonfilm-cooling options is shown in Figure 17. The effect of transpiration on the pressure distribution is evident. The adverse pressure gradient that is generated, the resulting upstream influence, and the subsequent favorable pressure gradient that follows it can also be seen in this figure. Temperature, pressure coefficient, and Mach number contours are given in Figures 18 through 20. The effects of the film-cooling are evident.

### CASE 3--3-D C3X RECTILINEAR TURBINE CASCADE

The final case considered was a 3-D demonstration calculation assuming laminar flow. The configuration consisted of a C3X cascade situated in the azimuthal-radial plane, and bounded in the transverse direction by an endwall and a symmetry plane. The three-dimensionality was introduced by stacking similar planes parallel to each other in the direction normal to a fixed endwall (see Figure 6). For the calculation, a grid consisting of  $100 \times 25 \times 15$  grid points in the pseudoazimuthal, pseudoradial, and transverse directions, respectively, was constructed. The height of the blade above the endwall (to the symmetry plane, midspan) was set to be one axial chord, while the inlet boundary layer thickness was 20% of that value.

The calculation was initiated with an initial condition that consisted of a 2-D solution with a simple boundary layer correction applied in the vicinity of the endwall. The corresponding 2-D solution was obtained with  $100 \times 25$  grid points, the inlet Mach number,  $Ma_1$ , was 0.15, the inlet Reynolds number based on inlet free-stream and time chord,  $Re_1$ , was 730, and the ratio of inlet total to downstream exit static pressure,  $P_t/P_{exit}$ , was 1.95. Total temperature was assumed to be constant. With this initial condition, a converged solution was obtained in less than 60 time steps.

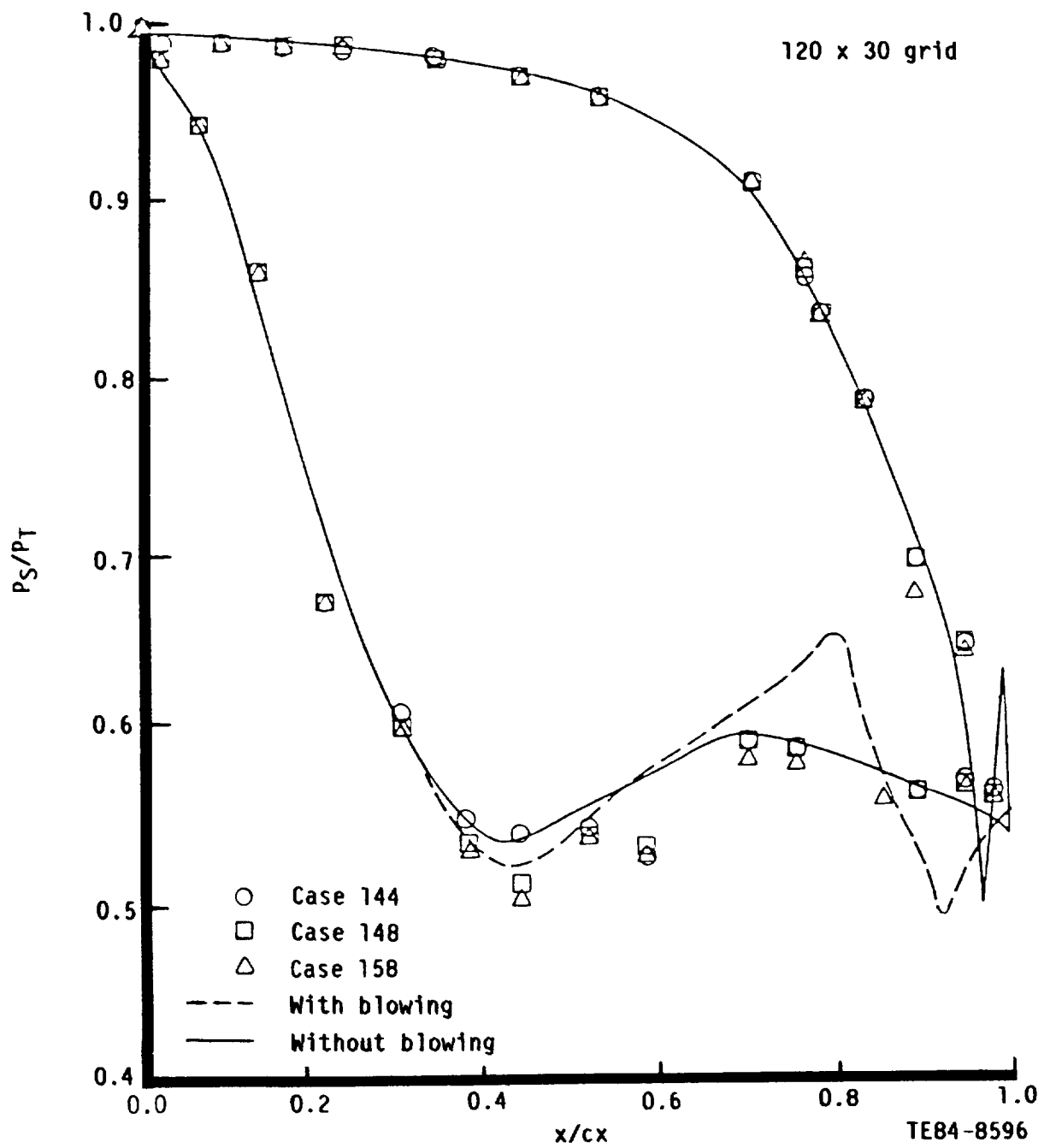
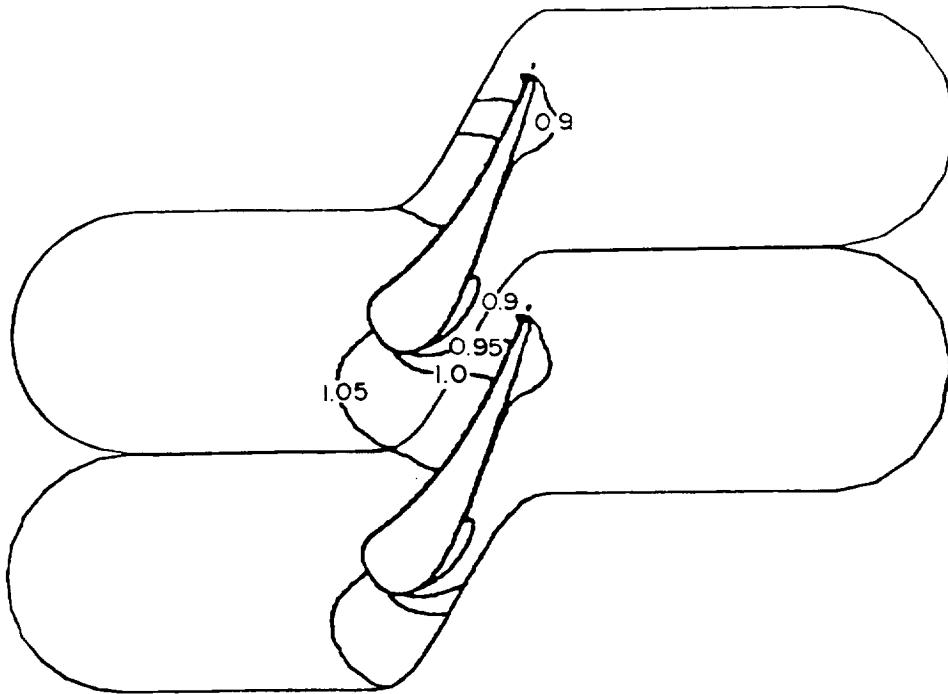
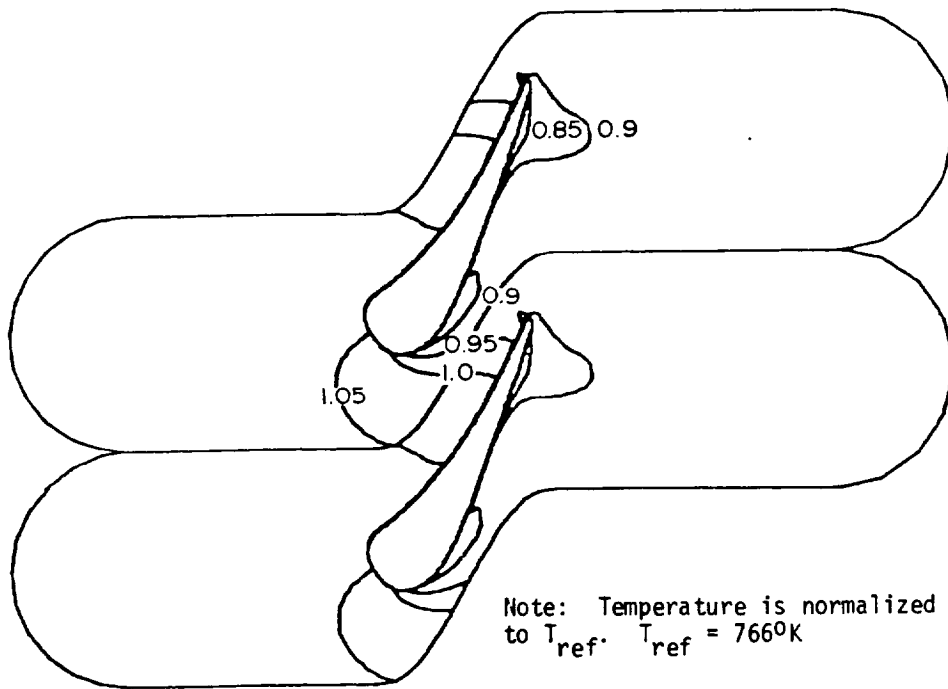


Figure 17. The effect of film cooling on pressure coefficient distributions.





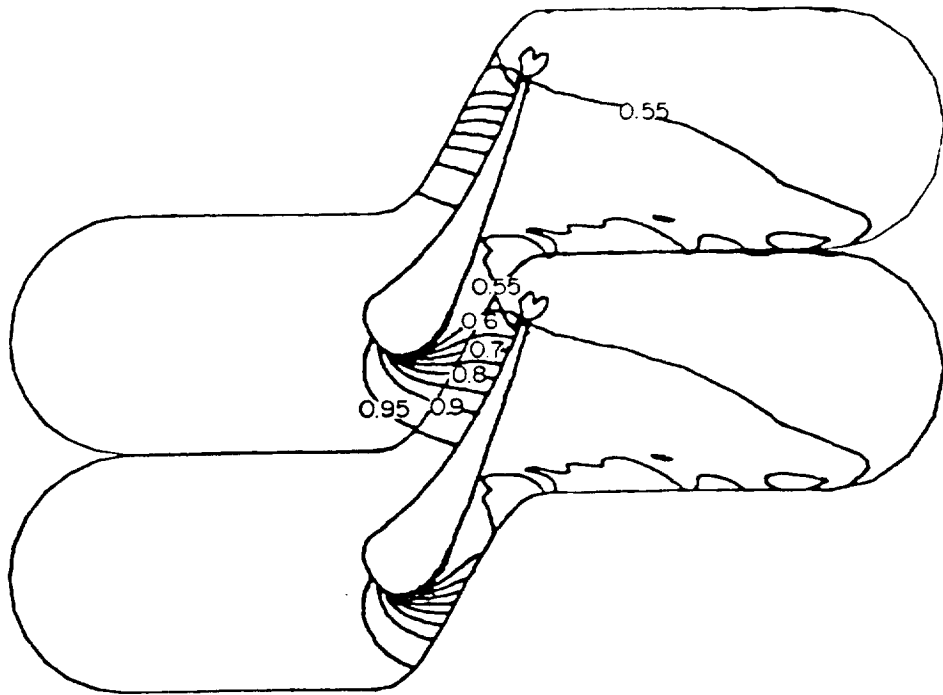
a. Without film cooling



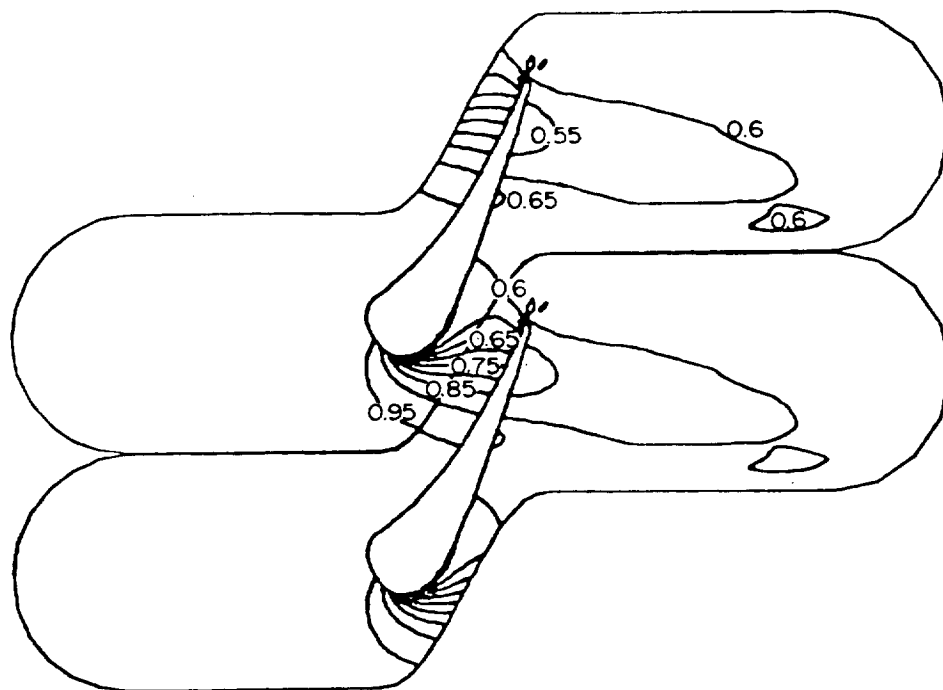
b. With film cooling

TE84-8597

Figure 18. Temperature contours.



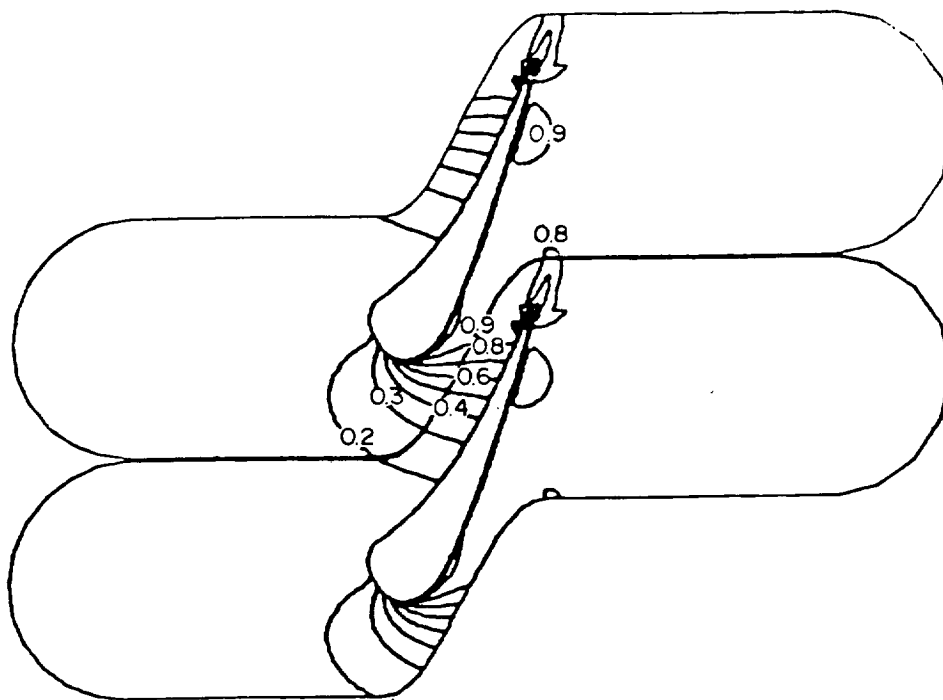
a. Without film cooling



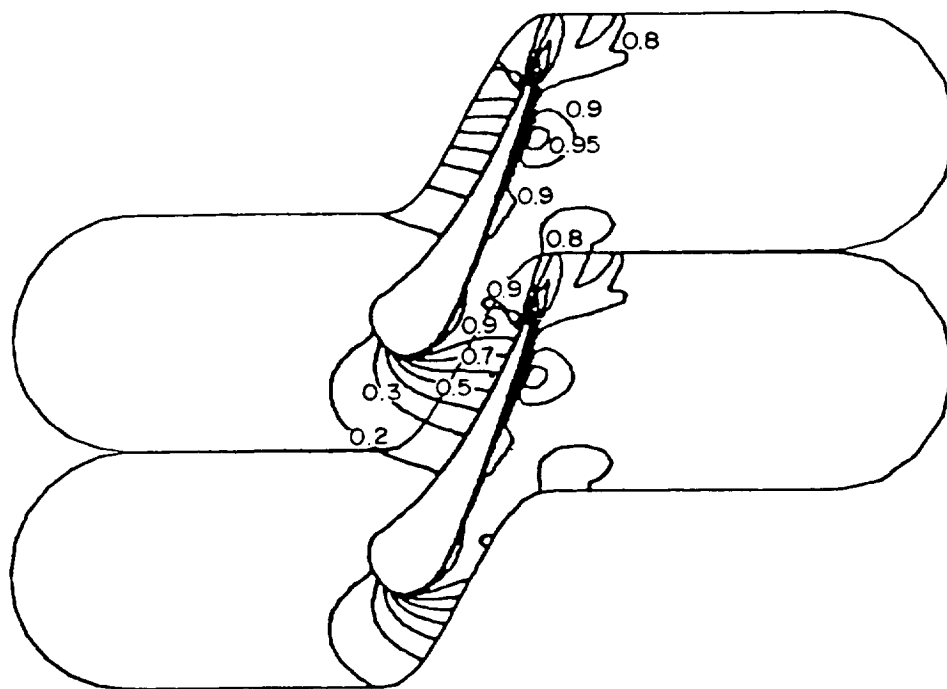
b. With film cooling

TE84-8598

Figure 19. Pressure contours.



a. Without film cooling



b. With film cooling

TE84-8599

Figure 20. Mach number contours.

The computed pressure distributions at different heights above the endwall are shown in Figure 21. The pressure side is minimally affected by the endwall, remaining at or near the 2-D value run on the same spanwise cross-sectional grid, while the suction side, which shows as much as a 15% change over the 2-D value near the 30% axial chord location, approaches the 2-D value at 26% span above the endwall. Near the endwall, the suction side of the blade is lightly loaded compared with the value of the midspan. These differences from the 2-D value are due to the effects of secondary flow generated by horseshoe and passage vortices. The results are consistent with the expected physics (Ref 6 and 40 through 43) though different geometry is considered in this effort. Figures 22, 23, and 24 show the static pressure contours at endwall, 3.5% span, and midspan plane, respectively. The effect of endwall on the pressure distribution is clear. In Figures 25, 26, and 27, the velocity vector plots are presented for the forward portion of the C3X cascade at three different planes above the endwall. Near the endwall (within 2.95% spanwise plane) a saddle point exists as indicated in the figures. This saddle point moves toward the leading edge and disappears beyond the 2.95% spanwise plane. A stagnation point forms on the nose of the blade surface beyond the 2.95% spanwise plane. These features are consistent with those expected.

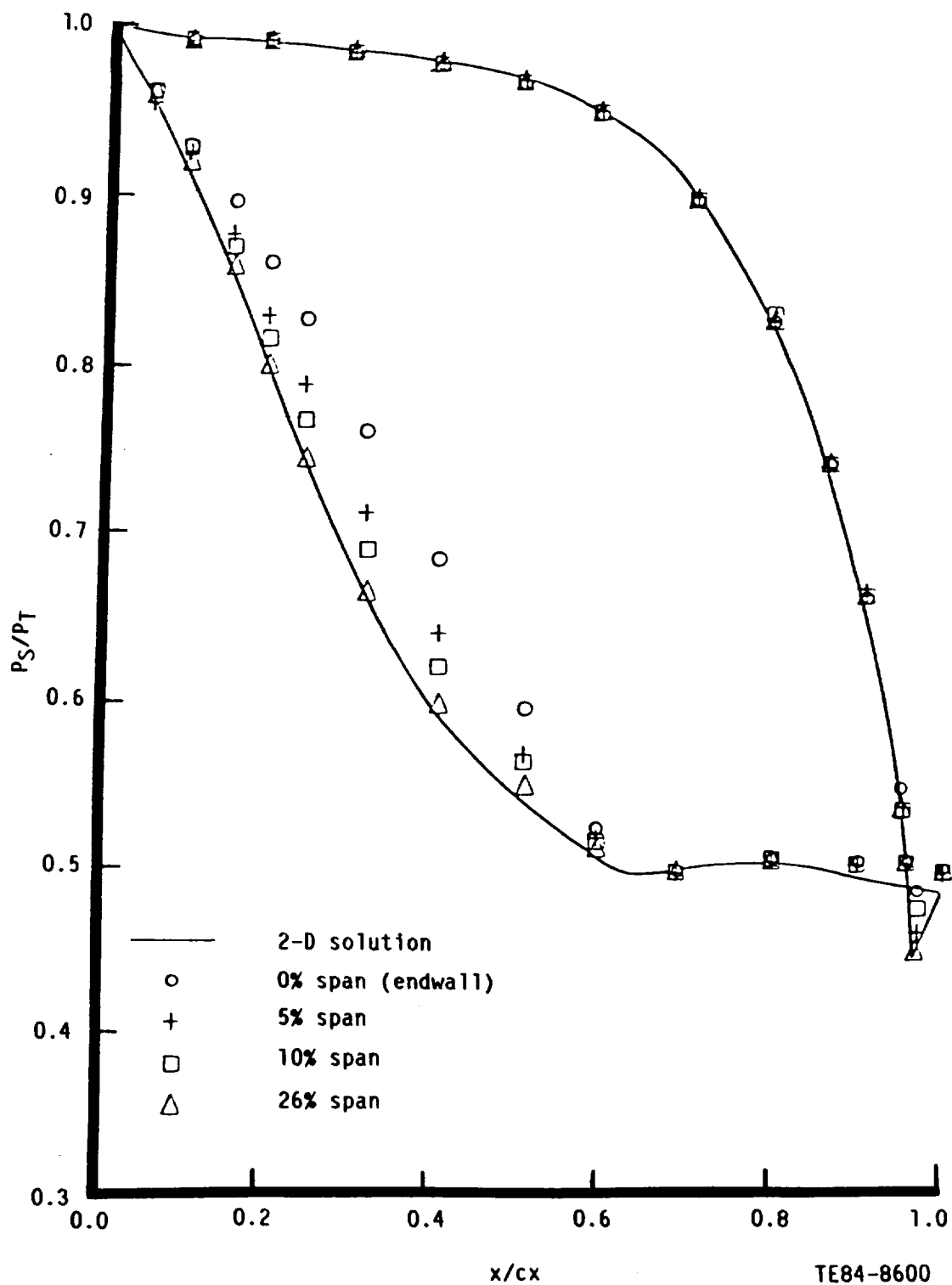


Figure 21. Three-dimensional rectilinear pressure coefficient distribution of the C3X cascade.

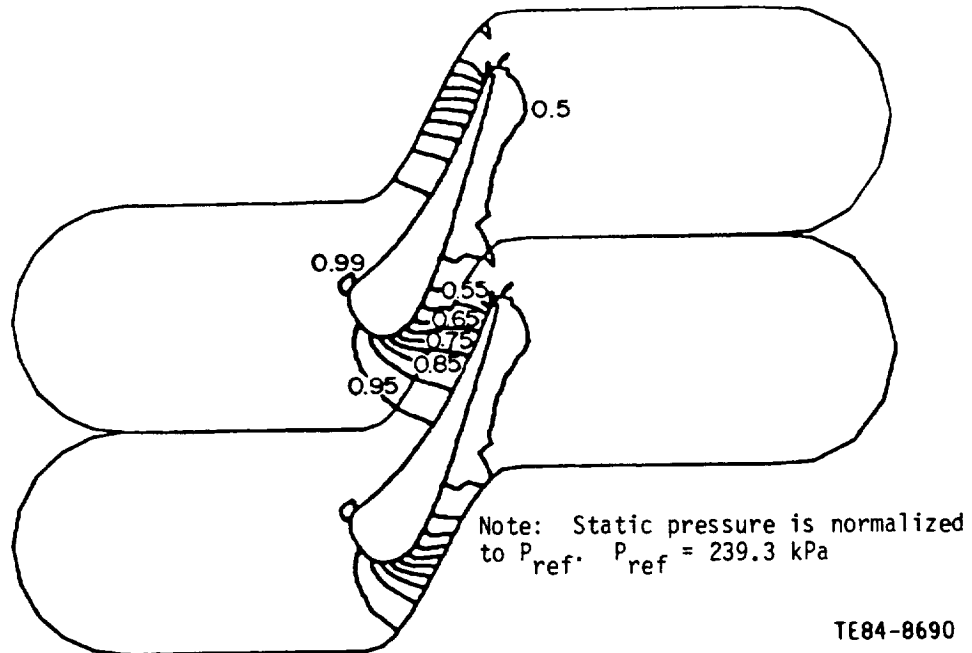


Figure 22. Static pressure contour at the endwall.

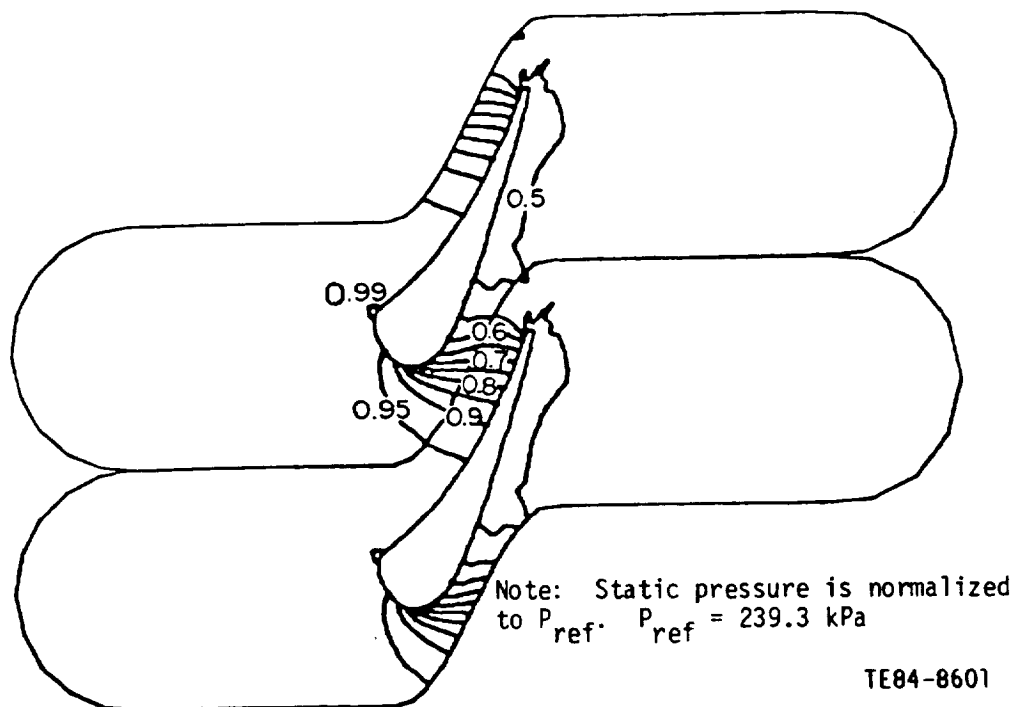


Figure 23. Static pressure contour at the 3.5% spanwise plane.

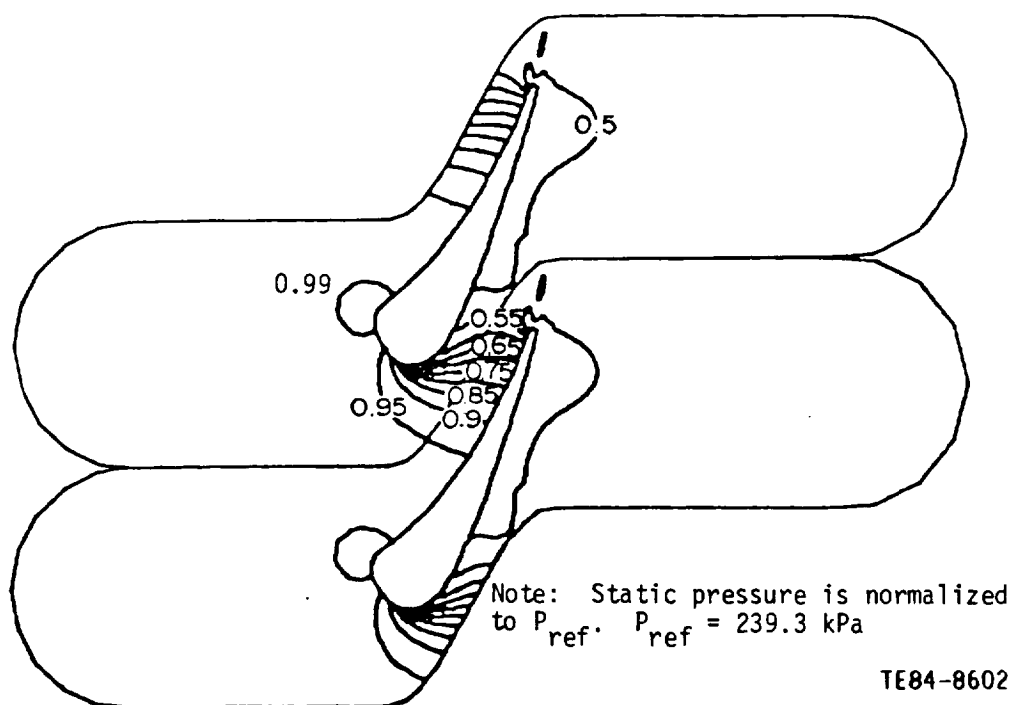


Figure 24. Static pressure contour at the midspan plane.

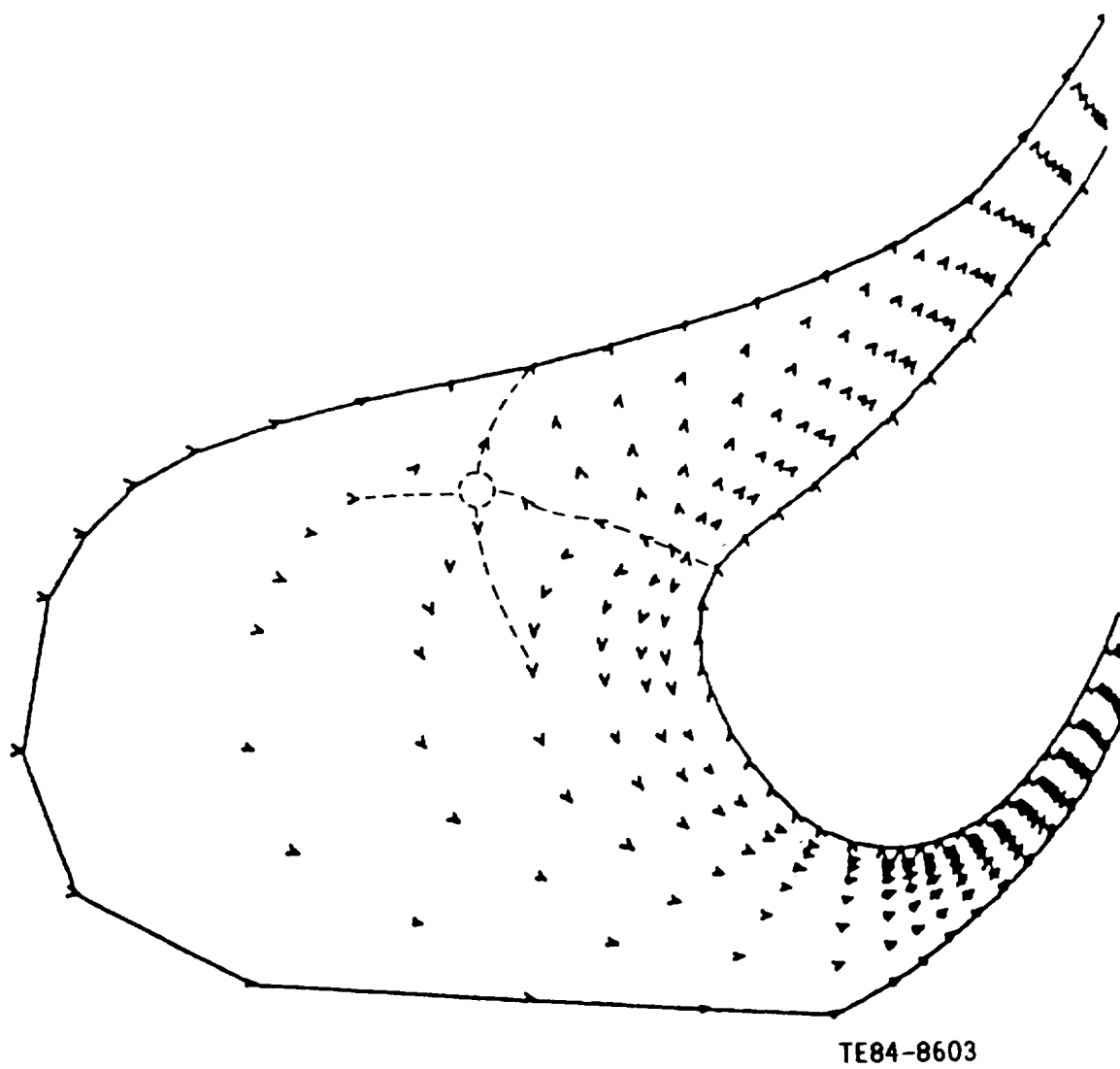


Figure 25. Leading edge vector plot at the 0.135% spanwise plane.



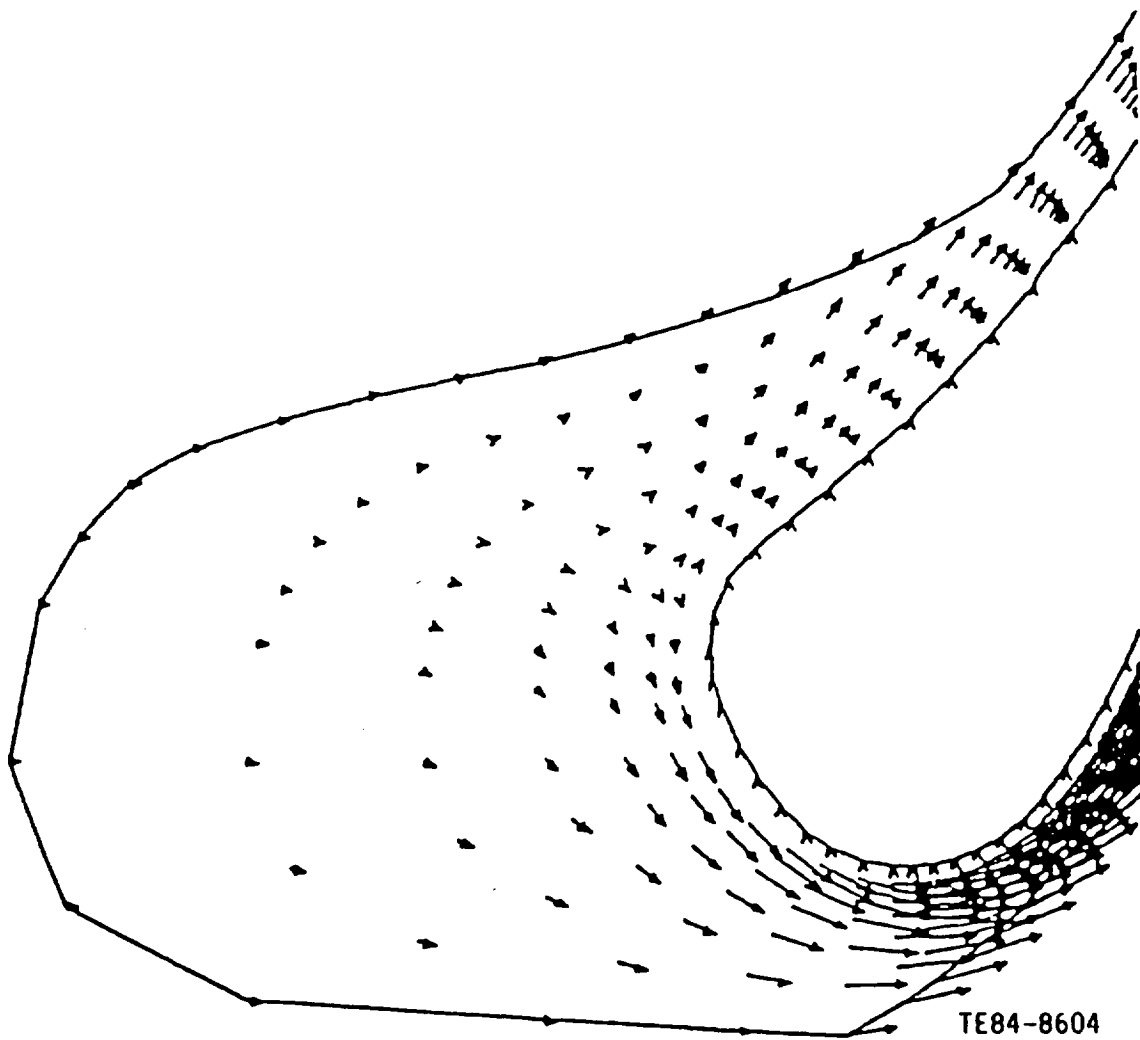


Figure 26. Leading edge vector plot at the 2.95% spanwise plane.

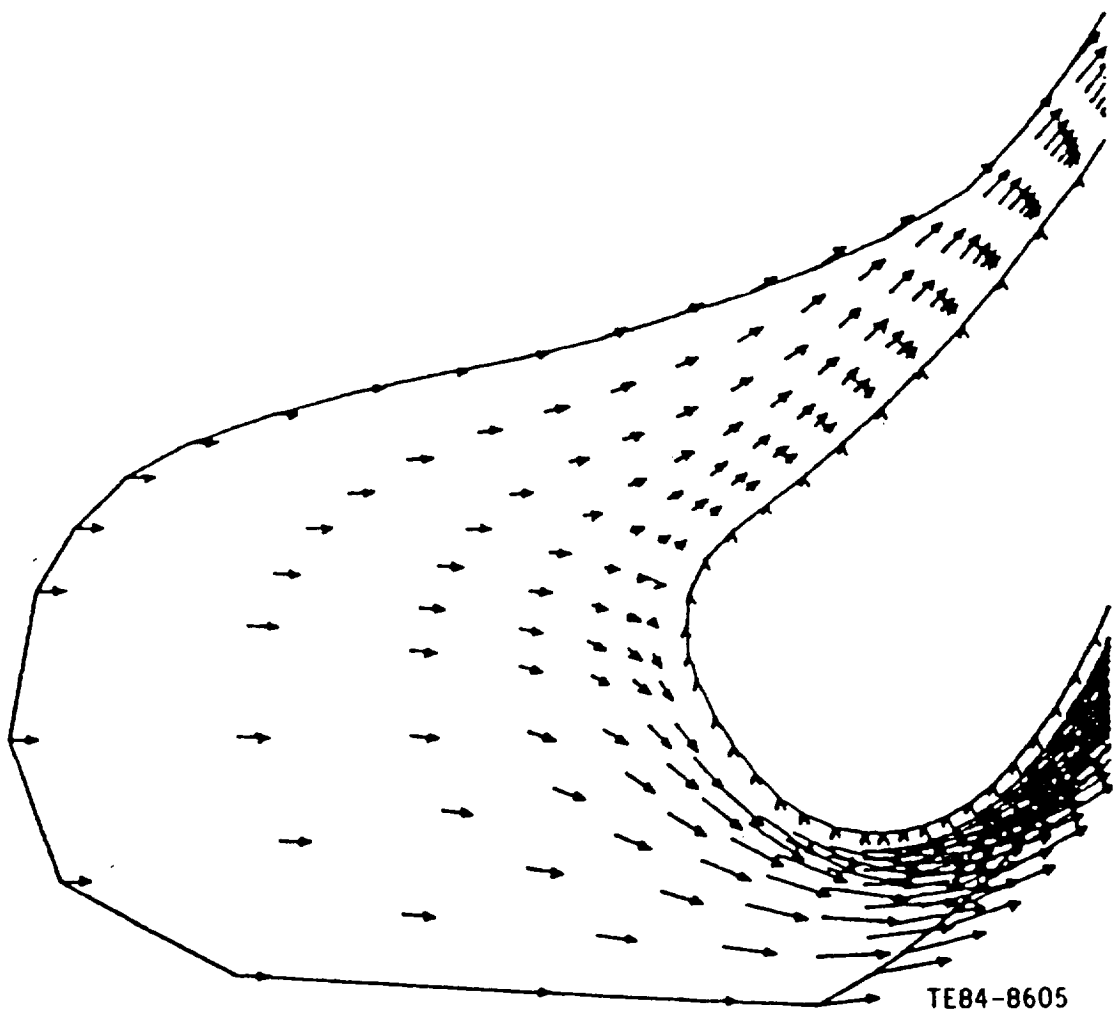


Figure 27. Leading edge vector plot at the midspan plane.

## V. CONCLUSIONS

The work described in this report has focused on the application of the time-dependent ensemble-averaged Navier-Stokes (N-S) equations to transonic turbine cascade flow fields. In particular, efforts have focused on an assessment of the procedure in conjunction with a suitable turbulence model to calculate steady turbine flow fields using an O-type coordinate system. Three cascade configurations have been considered: the two-dimensional (2-D) turbine cascade of Turner (Ref 21), the 2-D C3X turbine cascade of Hylton et al (Ref 22), and the three-dimensional (3-D) C3X rectilinear turbine cascade. The calculations were carried out in nonorthogonal body-fitted coordinate systems, while grid points were orthogonal near the body surface where viscous flow gradients were suitably resolved. A stagnation pressure inflow/static pressure outflow boundary condition was employed together with no-slip on the solid surfaces. In general, converged solutions were obtained within 80-150 time steps. For example, it took 80 time steps to reach a steady-state solution for a 2-D laminar Turner turbine cascade flow on a 100 x 30 computational grid starting with a uniform velocity (except for a near wall no-slip correction) and a uniform pressure field. The solution was obtained in approximately 570 sec central processing unit (CPU) time of the unvectorized CRAY-1 system. However, the code used to implement the algorithm is still a research code with a large amount of overhead computation. Recent effort on the code speed-up (Ref 9 and 44) shows the run time can be reduced by 50% with code restructuring. In addition, code vectorization is expected to decrease run time by at least a factor of five, leading to a 2-D solution in less than 1 min CPU time.

Comparisons were made between the predicted and measured surface pressure and heat transfer distributions wherever available. In general, the pressure predictions were in good agreement with the data. The computed heat transfer results also showed good agreement with the data when an empirical transition model was used, although further work in the development of laminar-turbulent transitional models is indicated. The calculations showed most of the known features associated with turbine cascade flow fields. The flow turning, leading edge stagnation region, boundary layer development, wake development, film-cooling effects, and 3-D boundary layer separation were all clearly observed. These results indicate the ability of the present N-S analysis to predict the

surface pressure distribution, heat transfer rates, viscous flow development for practical turbine cascades operating at realistic flow conditions in reasonable amounts of computation time with a suitable turbulence model, and plausible boundary conditions.

## APPENDIX A

### SOLUTION PROCEDURE

The solution procedure method employs a consistently-split linearized block implicit (LBI) algorithm, which has been discussed in detail in Ref 13 and 34. There are two important elements of this method:

- o the use of a noniterative formal time linearization to produce a fully-coupled linear multidimensional scheme that is written in block implicit form
- o solution of this linearized coupled scheme using a consistent "splitting" [alternating direction implicit (ADI) scheme] patterned after the Douglas-Gunn (Ref 35) treatment of scalar ADI schemes.

The solution procedure method is referred to as a split LBI scheme. The method has the following attributes:

- o The noniterative linearization is efficient.
- o The fully-coupled linearized algorithm eliminates instabilities and/or extremely slow convergence rates often attributed to methods that employ ad hoc decoupling and linearization assumptions to identify nonlinear coefficients that are then treated by lag and update techniques.
- o The splitting or ADI technique produces an efficient algorithm that is stable for large time steps and also provides a means for convergence acceleration for further efficiency in computing steady solutions.
- o Intermediate steps of the splitting are consistent with the governing equations, and this means that the physical boundary conditions can be used for the intermediate solutions. Other splittings that are inconsistent can have difficulty in satisfying physical boundary conditions (Ref 34).
- o The convergence rate and overall efficiency of the algorithm are much less sensitive to mesh refinement and redistribution than algorithms based on

explicit schemes or that employ ad hoc decoupling and linearization assumptions. This is important for accuracy and for computing turbulent flows with viscous sublayer resolution.

- o The solution procedure method is general and is specifically designed for the complex systems of equations that govern multiscale viscous flow in complicated geometries.

The LBI algorithm was later considered by Beam and Warming (Ref 45), but the ADI splitting was derived by approximate factorization instead of the Douglas-Gunn procedure. Beam and Warming refer to the algorithm as a delta form approximate factorization scheme. This scheme replaced an earlier nondelta form scheme (Ref 46), which has inconsistent intermediate steps.

#### SPATIAL DIFFERENCING AND ARTIFICIAL DISSIPATION

The spatial differencing procedures are a straightforward adaption of those used in Ref 13 and elsewhere. Three-point central difference formulas are used for spatial derivatives, including the first-derivative convection and pressure gradient terms. This has an advantage over one-sided formulas in flow calculations subject to two-point boundary conditions (virtually all viscous or subsonic flows) in that all boundary conditions enter the algorithm implicitly. In practical flow calculations, artificial dissipation is usually needed and is added to control high-frequency numerical oscillations that otherwise occur with the central-difference formula.

In the present investigation, artificial (anisotropic) dissipation terms of the form

$$\sum_j d_j \left( \frac{\partial y^j}{\partial x_j} \right)^2 \frac{\partial^2 u_k}{\partial x_j^2} \quad (40)$$

are added to the right-hand side of each (k-th) component of the momentum equation, where for each coordinate direction  $x_j$ , the artificial diffusivity  $d_j$  is positive and is chosen as the larger of zero and the local quantity

$\nu_e (\sigma \text{Re}_{\Delta x}^{-1})/\text{Re}$ . Here, the local cell Reynolds number  $\text{Re}_{\Delta x_j}$  for the  $j$ -th direction is defined by

$$\text{Re}_{\Delta x_j} = \text{Re} \left| \rho u_j \right| \Delta x_j / \nu_e \quad (41)$$

This treatment lowers the formal accuracy to  $O(\Delta x)$ , but the functional form is such that accuracy in representing physical shear stresses in thin shear layers with small normal velocity is not seriously degraded. This latter property follows from the anisotropic form of the dissipation and the combination of both small normal velocity and small grid spacing in thin shear layers.

#### SPLIT LBI ALGORITHM

##### Linearization and Time Differencing

The system of governing equations to be solved consists of either three or four equations: continuity and two components of momentum equation in three dependent variables,  $\rho$ ,  $u$ ,  $v$ , and  $w$ , or continuity and three components of momentum equation in four dependent variables,  $\rho$ ,  $u$ ,  $v$ , and  $w$ . Using notation similar to that in Ref 13, at a single grid point this system of governing equations can be written in the following form:

$$\partial H(\phi) / \partial t = D(\phi) + S(\phi) \quad (42)$$

where  $\phi$  is the column-vector of dependent variables,  $H$  and  $S$  are column-vector algebraic functions of  $\phi$ , and  $D$  is a column vector whose elements are the spatial differential operators that generate all spatial derivatives appearing in the governing equation associated with each element.

The solution procedure is based on the following two-level implicit time-difference approximations of Equation (42):

$$(H^{n+1} - H^n) / \Delta t = \beta (D^{n+1} + S^{n+1}) + (1 - \beta) (D^n + S^n) \quad (43)$$

where, for example,  $H^{n+1}$  denotes  $H(\phi^{n+1})$  and  $\Delta t = t^{n+1} - t^n$ . The parameter  $\beta$  ( $0.5 \leq \beta \leq 1$ ) permits a variable time-centering of the scheme, with a truncation error of order  $[\Delta t^2, (\beta - 1/2) \Delta t]$ .

A local time linearization (Taylor expansion about  $\phi^n$ ) of requisite formal accuracy is introduced, and this serves to define a linear differential operator  $L$  (Ref 13) such that

$$D^{n+1} = D^n + L^n(\phi^{n+1} - \phi^n) + O(\Delta t^2) \quad (44)$$

Similarly,

$$H^{n+1} = H^n + (\partial H / \partial \phi)^n (\phi^{n+1} - \phi^n) + O(\Delta t^2) \quad (45)$$

$$S^{n+1} = S^n + (\partial S / \partial \phi)^n (\phi^{n+1} - \phi^n) + O(\Delta t^2) \quad (46)$$

Equations (44 through 46) are inserted into Equation (43) to obtain the following system, which is linear in  $\phi^{n+1}$

$$(A - \beta \Delta t L^n) (\phi^{n+1} - \phi^n) = \Delta t (D^n + S^n) \quad (47)$$

and is termed an LBI scheme. Here,  $A$  denotes a matrix defined by

$$A \equiv (\partial H / \partial \phi)^n - \beta \Delta t (\partial S / \partial \phi)^n \quad (48)$$

Equation (47) has  $O(\Delta t)$  accuracy unless  $H \equiv \phi$ , in which case the accuracy is the same as Equation (43).

### Special Treatment of Diffusive Terms

The time differencing of diffusive terms is modified to accommodate cross-derivative terms and also turbulent viscosity and artificial dissipation coefficients that depend on the solution variables. Although formal linearization



of the convection and pressure gradient terms and the resulting implicit coupling of variables is critical to the stability and rapid convergence of the algorithm, it does not appear to be important for the turbulent viscosity and artificial dissipation coefficients. Because the relationship between  $\mu_e$  and  $d_j$  and the mean flow variables is not conveniently linearized, these diffusive coefficients are evaluated explicitly at  $t^n$  during each time step. Notationally, this is equivalent to neglecting terms proportional to  $\partial\mu_e/\partial\phi$  or  $\partial d_j/\partial\phi$  in  $L^n$ , which are formally present in Equation (44), but retaining all terms proportional to  $\mu_e$  or  $d_j$  in both  $L^n$  and  $D^n$ .

Extensive experience has shown that this has little, if any, affect on the performance of the algorithm. This treatment also has the added benefit that the turbulence model equations can be decoupled from the system of mean flow equations by an appropriate matrix partitioning (Ref 34) and solved separately in each step of the ADI solution procedure. This reduces the block size of the block tridiagonal systems that must be solved in each step and reduces the computational labor.

In addition, the viscous terms in the present formulation include a number of spatial cross-derivative terms. Although it is possible to treat cross-derivative terms implicitly within the ADI treatment that follows, it is not convenient to do so; and consequently, all cross-derivative terms are evaluated explicitly at  $t^n$ . For a scalar model equation representing combined convection and diffusion, it has been shown by Beam and Warming (Ref 47) that the explicit treatment of cross-derivative terms does not degrade the unconditional stability of the present algorithm. To preserve notational simplicity, it is understood that all cross-derivative terms appearing in  $L^n$  are neglected but are retained in  $D^n$ . Neglecting terms in  $L^n$  has no effect on steady solutions of Equation (47), because  $\phi^{n+1} - \phi^n = 0$ , and thus Equation (47) reduces to the steady form of the equations:  $D^n + S^n = 0$ . Aside from stability considerations, the only effort of neglecting terms in  $L^n$  is to introduce an  $O(\Delta t)$  truncation error.

### Consistent Splitting of the LBI Scheme

To obtain an efficient algorithm, the linearized system Equation (47) is split using ADI techniques. To obtain the split scheme, the multidimensional operator  $L$  is rewritten as the sum of three one-dimensional (1-D) suboperators  $L_i$  ( $i = 1, 2, 3$ ) each of which contains all terms having derivatives with respect to the  $i$ -th coordinate. The split form of Equation (47) can be derived either as in Ref 13 and 34 by following the procedure described by Douglas and Gunn (Ref 35) in their generalization and unification of scalar ADI schemes, or using approximate factorization. For this system of equations, the split algorithm is given by

$$(A - \beta \Delta t L_1^n) (\phi^* - \phi^n) = \Delta t (D^n + S^n) \quad (49a)$$

$$(A - \beta \Delta t L_2^n) (\phi^{**} - \phi^n) = A (\phi^* - \phi^n) \quad (49b)$$

$$(A - \beta \Delta t L_3^n) (\phi^{n+1} - \phi^n) = A (\phi^{**} - \phi^n) \quad (49c)$$

where  $\phi^*$  and  $\phi^{**}$  are consistent intermediate solutions. If spatial derivatives appearing in  $L_i$  and  $D$  are replaced by three-point difference formulas, as indicated previously, then each step in Equation (49) can be solved by a block-tridiagonal elimination.

Combining Equations (49a-c) gives

$$(A - \beta \Delta t L_1^n) A^{-1} (A - \beta \Delta t L_2^n) A^{-1} (A - \beta \Delta t L_3^n) (\phi^{n+1} - \phi^n) = \Delta t (D^n + S^n) \quad (50)$$

which approximates the unsplit scheme Equation (47) to  $O(\Delta t^2)$ . Because the intermediate steps are also consistent approximations for Equation (47), physical boundary conditions can be used for  $\phi^*$  and  $\phi^{**}$  (Ref 13 and 34). Finally, since the suboperators  $L_i$  are homogeneous operators, it follows from Equations (49a-c) that steady solutions have the property of  $\phi^{n+1} = \phi^* = \phi^{**} = \phi^n$  and satisfy

$$D^n + S^n = 0 \quad (51)$$

The steady solution depends only on the spatial difference approximations used for Equation (51) and does not depend on the solution algorithm itself.

## APPENDIX B

### USER'S MANUAL

The user's manual that follows describes two separate computer codes that are used to obtain solutions for cascade flow problems. A nonorthogonal coordinate system is generated through COORD so that the physical boundaries and periodic boundaries coincide with coordinate surfaces. The output from COORD consists of results printed in the output file and results written on a temporary file. This latter set of results must be saved and used as input for the second program, MINT.

Figure 28 shows the overall program flow of COORD. Table I describes the COORD namelist input. The MINT code combines a block data program (BLKDAT) containing pertinent data statements, a main program (DAL) and a series of subroutines to perform the required calculations. Figure 29 shows the overall program flow, Figure 30 illustrates the input and initialization procedures. Table II describes the MINT namelist input, and Table III lists the major FORTRAN variables in MINT. Figure 31 provides a global description of execution control. These program flow charts only provide a means of guidance for interested users wishing to consult the program listing.

#### SAMPLE INPUT CARDS AND PRINTED OUTPUT

A sample two-dimensional (2-D) case was run to illustrate the set up of input parameters and typical printouts of the COORD program and MINT code, respectively. Table IV lists sample inputs for COORD. For the program, all parameters in the namelist input &INPT and &DATA1 must be specified. Two sequential &DATA1 are required in the namelist input. The first set is used for the parameterization of the inner loop and the second set is used for that of the outer loop. Sample input for the MINT code is listed in Table V. For the MINT code, the namelist data shown is for a new calculation. In the case of a restarted calculation the input is identical except for the restart flag IREST set in &READ1, and the variables NT and DT in &READ9. It is not advisable to change any other values on a restart.

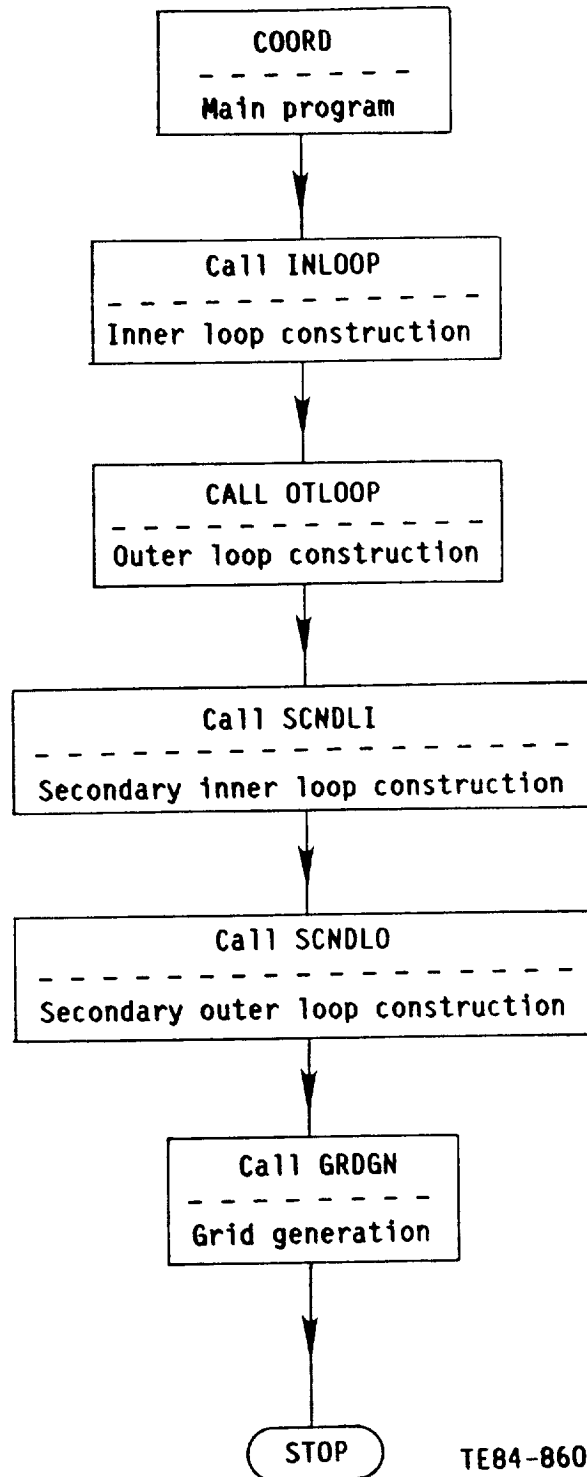
In COORD, the code output first prints out the input airfoil coordinate data, as shown in Table VI. These geometry data are followed by the print-out of

the namelist INPT and two sequential DATA1. Finally, the grid coordinates' associated metric data, coordinate intersection angles, and Jacobian are printed out. The grid coordinates are written by means of a binary write on TAPE9 and must be saved for input to the MINT code.

In the MINT code, the code output first prints out a series of dimensionless parameters (DIM1-DIM10, DIM12, and DIM14) and the dimensionless, referenced total temperature, total pressure, and total enthalpy as shown in Table VII. This output is followed by the finite difference coefficients for first and second derivatives in both directions. In each direction, three lines are written. The first and third lines give one-sided difference weights at the lower and upper boundaries; the second line of each set gives central differences used for the interior points. Six numbers are written on each line; the first set of three values represents the first derivative coefficients and the second set of three values represents the second derivative coefficients.

The next output item is the namelist data &READ1 and &READ9. The values of some parameters may be changed by the internal operations. The following items are the print-outs of the local surface static pressure, boundary layer thickness, and heat transfer coefficients around the blade surface, respectively. The upstream total pressure is also indicated in the print-out. The value of total pressure, PTOTI, will be reached in IDTAB (through namelist input) time steps if the PTOTI is greater than the reference total pressure. A summary print, which gives not only the maximum relative change over a time step by SSTES1 but also the location, is written at each time step. The maximum relative changes of each dependent variable are also given. RESMAX is the maximum residual of the equations solved and indicates how well the steady-state equation is being satisfied.

Following the summary data of the final time step of the run, the pressure coefficient and the heat transfer coefficient are written against the blade surface coordinates. The distribution of the heat transfer coefficient along the blade surface is zero for the case of IHSTAG=2 (i.e. constant stagnation enthalpy option). Finally, a complete flow field print-out is produced.



TE84-8606

Figure 28. The overall program flow for program COORD.

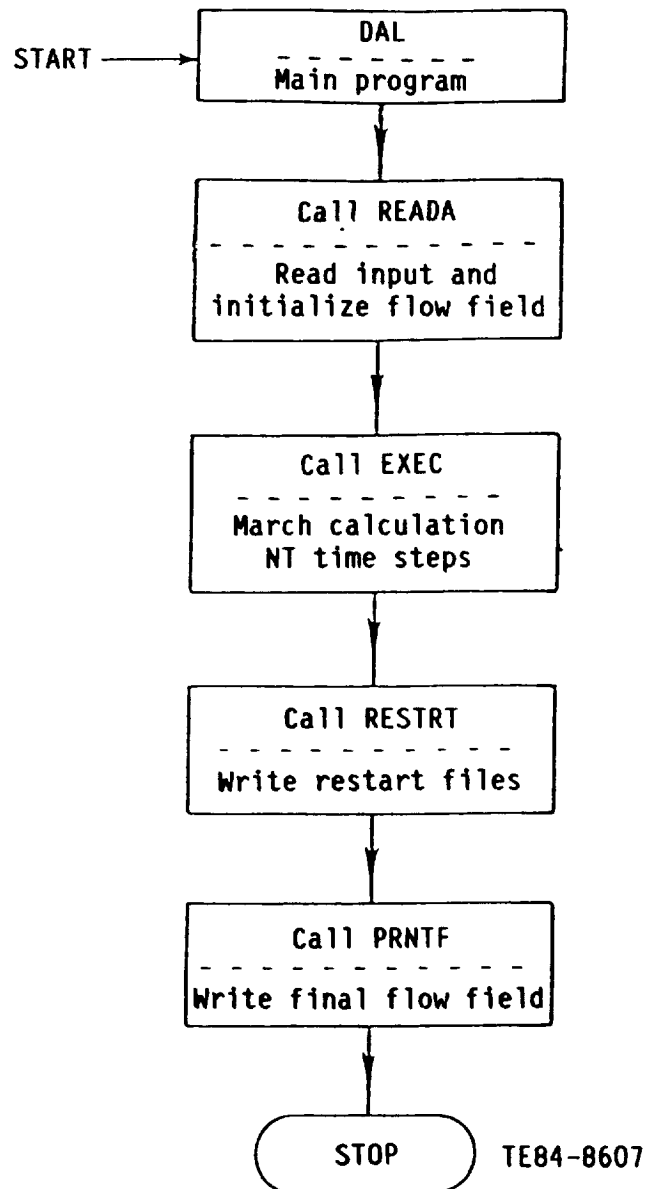


Figure 29. The overall program flow for program DAL.

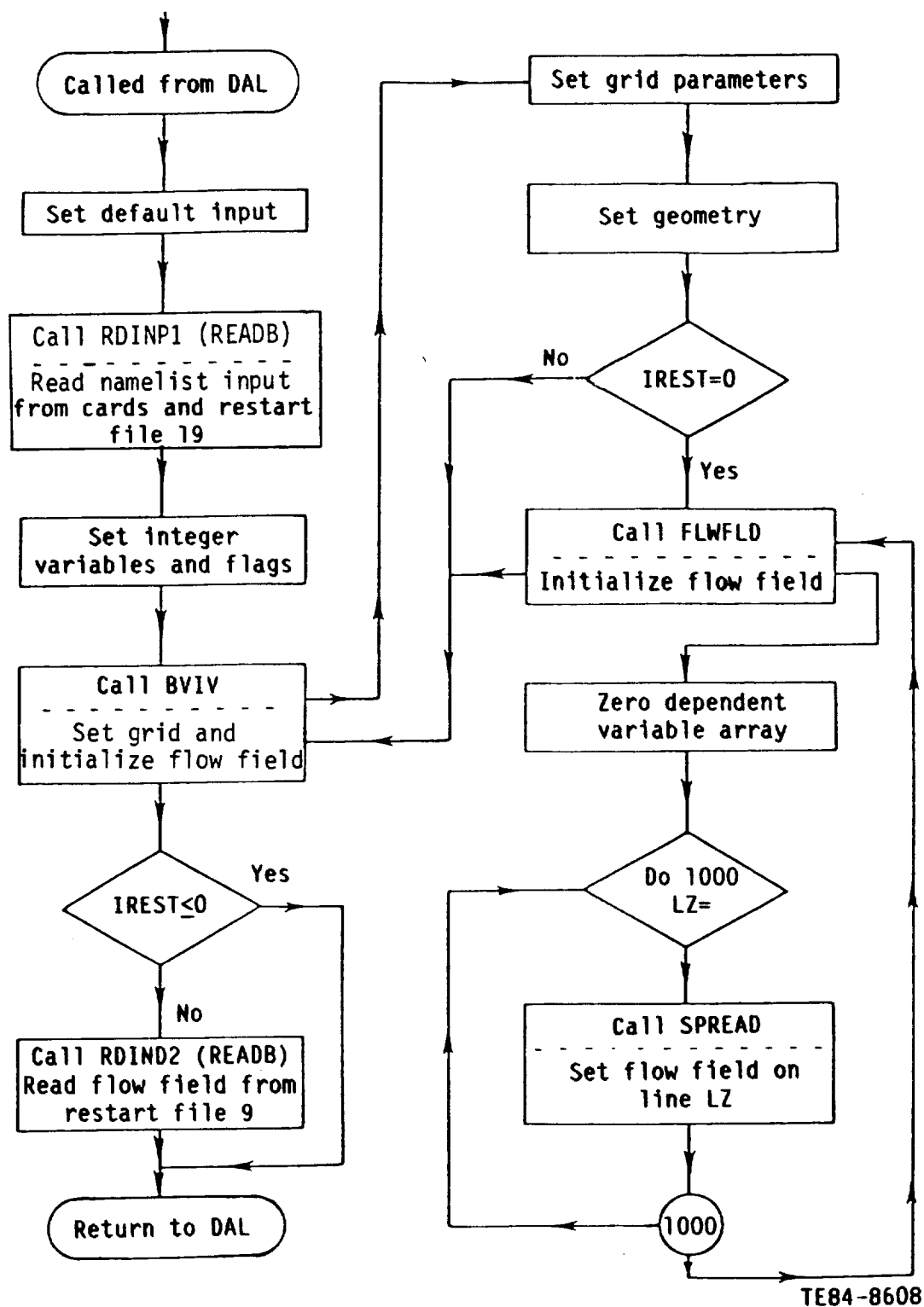
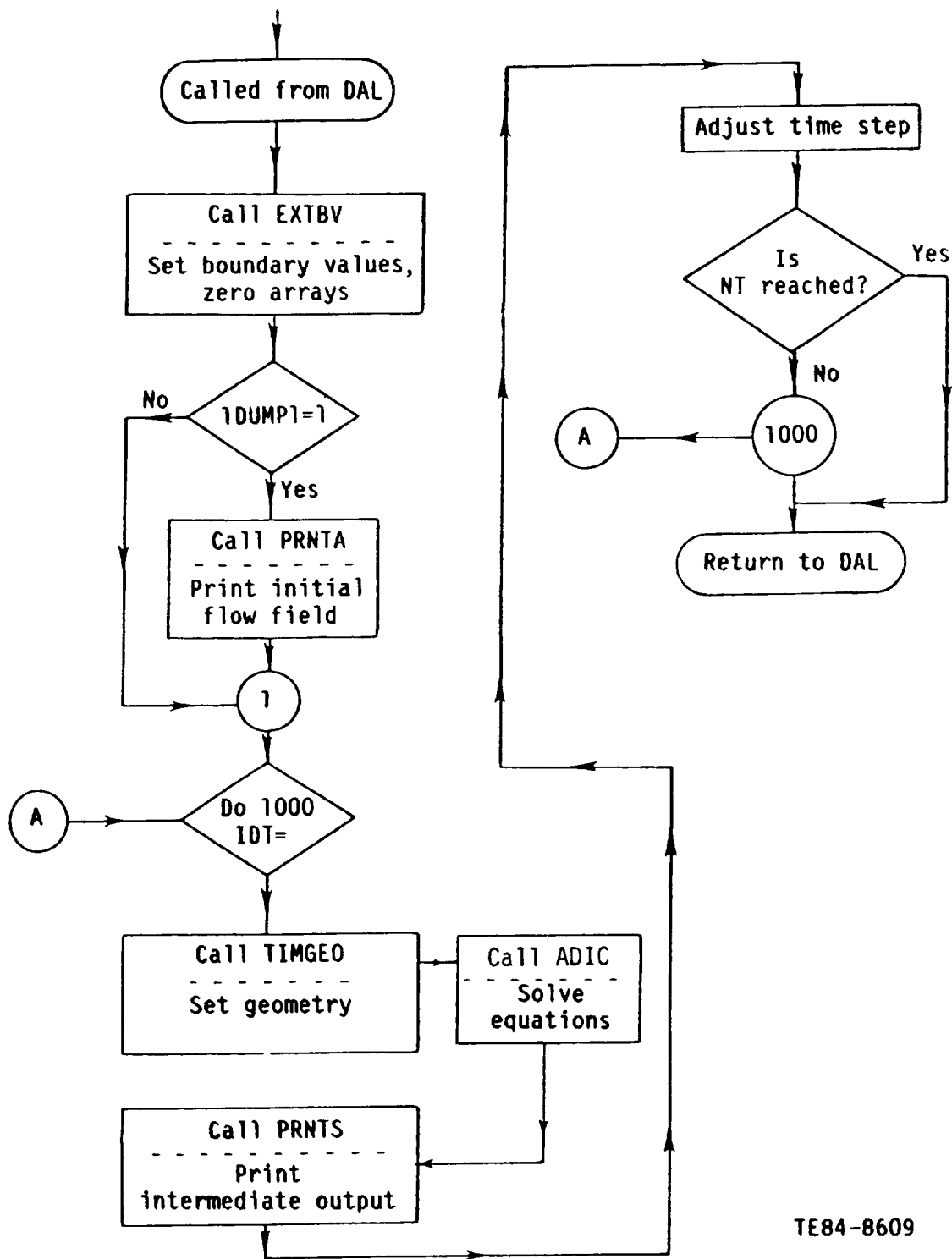


Figure 30. The program flow chart for subroutine READA.





TE84-8609

Figure 31. The program flow chart for subroutine EXEC.

Table I.  
COORD namelist input description.

<u>Namelist or variable name</u>	<u>Description</u>
<u>&amp;INPT</u>	
NRAD	number of pseudoradial points
NTHETA	number of pseudoazimuthal points
RMAX0	cascade passage spacing/2
RMAX1	normal distance between blade surface and inner-secondary loop
RMAX2	normal distance between outer loop and outer-secondary loop
DAMP	damping parameter in pseudoradial direction
NE	number of airfoil input data points
LED	airfoil data point number at airfoil leading edge
DMX(I)	array for x-location of airfoil input data points
DMY(I)	array for y-location of airfoil input data points
XM2, XM3 YM2, YM3	input outer loop location (see Figure 32)
EXTF, EXTR	extension of periodic line (see Figure 32)
<u>&amp;DATA1</u>	
NCLUST	total number of the interior cluster points [A cluster point is the sequential number of the selected grid point that must coincide with a particular predetermined value of the z-coordinate. Accordingly, pairs of (1, YFIRST) and (NUMDZ+2, YLAST) are also cluster points, but they are boundary cluster points.]
CLPY(I), I = 1 - 60	the z-coordinate of the cluster point (Both boundary and internal cluster points must be specified.)
CLPX(I), I = 1 - 60	the sequential number of the grid point corresponding to CLPY(I)
ETAP(J), I = 1 - 60	the sequential number of the grid point defined as the pivot point (The grid spacing will have the fastest variation at a pivot point. For each of the interior cluster points there will be a pair of pivot points: one ahead of the cluster point, the other after the

Table I. (cont)

<u>Namelist or variable name</u>	<u>Description</u>
	cluster point. However, only one pivot point will be associated with each of the boundary cluster points.)
ALPH(J), I = 1 - 60	width parameter specifying width (in terms of the number of grid points) in which 90% of the grid size variation takes place around the pivot point ETAP(J)
> 0	decreasing grid size
< 0	increasing grid size
NEND = 0	no stretching at YFIRST and YLAST
= 1	stretching at YFIRST only
= 2	stretching at YLAST only
= 3	stretching at YFIRST and YLAST
RHO (always > 0.0)	approximate ratio of the grid size at CLPY(2) to the maximum grid size in the interval $CLPY(1) < Z < CLPY(2)$
= 1.0	no stretching at YFIRST (used with NEND = 0 or 2)
RATIO(K), K = 1 - 40 (always > 0.0)	approximate ratio of the grid size at CLPY(K+1) to the maximum grid size in the interval $CLPY(K) < Z < CLPY(K+1)$
= 1.0	no grid variation at CLPY(K+1)
BETA0 (always > 0.0)	calculated (It indicates the first derivative of the z-coordinate with respect to the computational coordinate at YFIRST.)
BETA(L), L = 1 - 60 (always > 0.0)	calculated [It indicates the ratio between the grid sizes on both sides of the pivot point ETAP(L+1).]

---

**Notes:**

The airfoil x-y data points DMX and DMY must be input in order around the airfoil starting from any arbitrary location on the airfoil. The computer code then nondimensionalizes the coordinates with respect to the axial chord and places the origin at the location of maximum x (near the trailing edge) with the airfoil oriented as shown in Figure 32. The units of DMX and DMY are arbitrary while RMAX0, RMAX1 and RMAX2 are nondimensional.

After this is done, the grid point numbering is reordered so that the first point terminates in the trailing cap, e.g., line AA' in Figure 2. All pseudo-azimuthal grid point locations are referenced to this line AA'. Hence, CLPX and CLPY refer to the grid point locations and the azimuthal parameterized coordinate value, respectively.

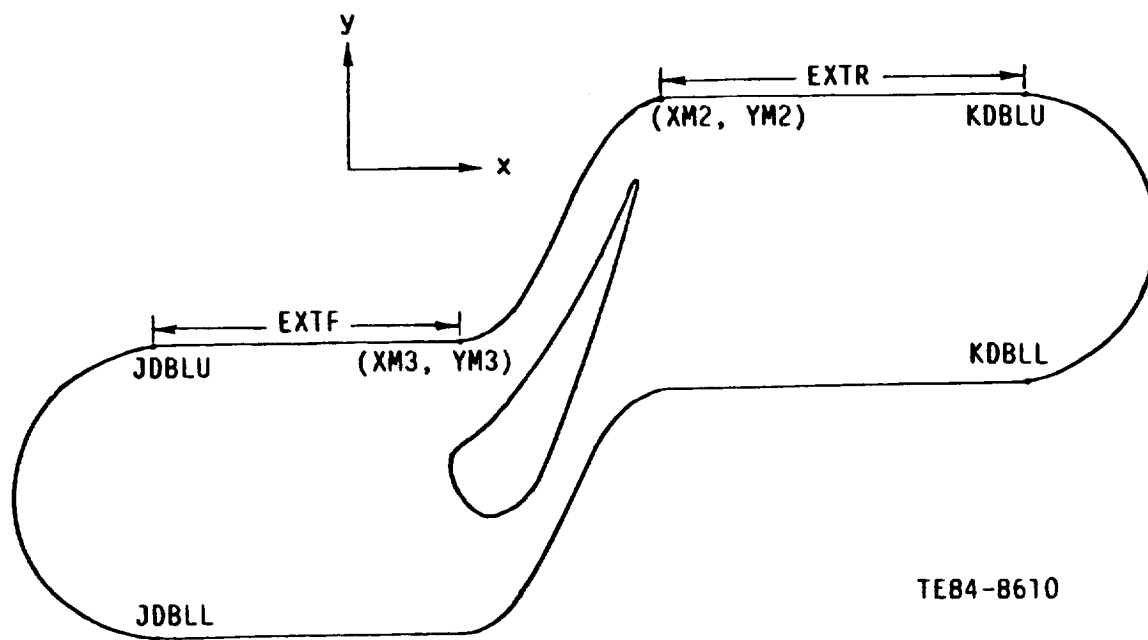


Figure 32. Cascade geometry.

Table II.  
MINT namelist input description.

<u>Namelist or variable name</u>	<u>Description</u>
<u>&amp;READ1</u>	
IREST = 0	A new calculation is being started.
= 1	The case is being run from the restart files.
IOTAPE = 10	output unit number for the dependent variable array restart data
INTAPE = 9	input unit number for the dependent variable array restart data
IOTAP1 = 20	output unit number for the namelist restart data
INTAP1 = 19	input unit number for the namelist restart data
<u>&amp;READ9</u>	
NUMDX	number of interior grid points in the pseudoazimuthal direction (x or y <sup>1</sup> direction); total number of points in this direction = NUMDX + 2, NUMDX ≤ 128
NUMDY	number of interior grid points in the spanwise direction (3D only)
NUMDZ	number of interior grid points in the pseudoradial direction (z or y <sup>3</sup> direction); total number of points in this direction = NUMDZ + 2, NUMDZ ≤ 28
TWOD = T	logical variable for 2-D calculation
= F	logical variable for 3-D calculation
CLENG	reference length--m
WREF	reference velocity--m/sec
DENSR	reference density--kg/m <sup>3</sup>
TREF	reference temperature--°K
VISCR	reference dynamic viscosity--kg/m sec
AVISC(IDIR,IEQ)	artificial dissipation parameter $\sigma$ IEQ = 1-5 and IDIR = 1-3 IEQ = 1 indicates the x-momentum equation. IEQ = 2 indicates the y-momentum equation. IEQ = 3 indicates the z-momentum equation. IEQ = 4 indicates the continuity equation.

Table II. (cont)

<u>Namelist or variable name</u>	<u>Description</u>
	<p>IEQ = 5 indicates the energy equation.  IEQ = 16 indicates the turbulent kinetic energy.  IEQ = 17 indicates the turbulent dissipation energy rate.  IDIR = 1 indicates the x second derivative term.  IDIR = 2 indicates the y second derivative term.  IDIR = 3 indicates the z second derivative term.</p> <p>For example, AVISC(3, 1) is the value of <math>\sigma</math> used for the artificial dissipation term <math>\partial^2 U / \partial Z^2</math> in the x-momentum equation. Even if the y-momentum equation is not solved, the corresponding AVISC must be supplied. Default values are 0.0; recommended values are 0.50 initially, followed by runs at 0.2.</p>
NT	number of time steps to be run
DT	initial nondimensional time step (If DT is omitted on a restart, DT will be set to the value it was at the termination of the last run.)
DTMIN	minimum nondimensional time step for this run
DTMAX	maximum nondimensional time step for this run
ITEST	Steady-state test is performed every ITEST time steps. (Default value is 1.)
IPRINT	Complete flow field print-outs are provided every IPRINT time steps.
IVARPR(IV)	optional print control flag for variable IV
= 0	suppress print-out of variable IV
= 1	normal print-out of variable IV
IV	IVARPR(IV)
1	transverse velocity, u
2	spanwise velocity, v
3	streamwise velocity, w
4	density, $\rho$
5	enthalpy, h
16	turbulent kinetic energy, k
17	turbulent dissipation rate, $\epsilon$
26	pressure, P
27	temperature, T
28	effective viscosity, $\mu_{\text{eff}}$
33	mixing length, $\ell$

Table II. (cont)

<u>Namelist or variable name</u>	<u>Description</u>
	35 Mach number, Ma
	36 total pressure, $P_T$
IDUMP1	
= 1	print initial flow field for this run
= 2	no initial print-out
IPLOT	
= 0	no plot file (TAPE1) written
> 0	plot file written at time step increment IPLOT
JDBLU	point number at the end of the periodic line in the leading edge of the cascade (see Figure 32) referenced to the grid point corresponding to line AA' in Figure 2
JDBLL	point number at the end of the periodic line in the leading edge of the cascade (see Figure 32) referenced to the grid point corresponding to line AA' in Figure 2
KDBLU	point number at the end of the periodic line in the trailing edge of the cascade (see Figure 32) referenced to the grid point corresponding to line AA' in Figure 2
KDBLL	point number at the end of the periodic line in the trailing edge of the cascade (see Figure 32) referenced to the grid point corresponding to line AA' in Figure 2
IHSTAG	
= 0	static enthalpy option
= 2	constant stagnation enthalpy option
FLWNG	exit flow angle used for defining the wake region and boundary extrapolation, referenced to streamwise axis, x, as shown in Figure 32
TGAS	total temperature of the incoming gas at the inlet

Table II. (cont)

<u>Namelist or variable name</u>	<u>Description</u>
TWALL1	surface temperature distribution along the blade surface (nondimensional), referenced to pseudoazimuthal grid point location around body
IBLOW	
= 0	without film-cooling option
= 1	with film-cooling option
BLOU	U velocity component of the blowing velocity profile for the film-cooling option (nondimensional), referenced to pseudoazimuthal grid point location around body
BLOW	W velocity component of the blowing velocity profile for the film-cooling option (nondimensional), referenced to pseudoazimuthal grid point location around body
PTOTI	total pressure at the inlet of the cascade flow field (nondimensional)
IVISC	index for turbulent modeling
= 1	laminar flow constant viscosity
= 2	laminar flow Sutherland's law
= 3	mixing length model
= 4	k- $\epsilon$ one-equation model
= 5	k- $\epsilon$ two-equation model
IDTA	the time step number at which the inlet total pressure begins to be increased linearly (default IDTA = 0)
IDTAB	The number of time steps used to increase inlet total pressure up to PTOTI begins at IDTA (default IDTAB = 10).

---

**Notes:**

The nondimensional time is defined as  $CLENG/WREF$ . The recommended values of the time steps can be obtained from the sample run in this User's Manual.



Table III.  
List of major FORTRAN variables in MINT.

<u>FORTRAN symbol</u>	<u>Common block</u>	<u>Description</u>
AC(I,J,K)	BLK1	dependent variable array
ACG(J,J)	BLK1	geometry data array
AN(I,J)	BLKM	array storing time term linearized coefficients
APR(I,J)	PRNT	print output array
AVANDR	TURB	damping constant
AVISC(I,J)	MISC2	artificial dissipation parameter
C(I,J,K)	BLKM	coupled matrix array storage
CLENG	CREF	reference length
CMACH	MISC2	reference Mach number
D	VARNO	index for divergence
D1(I,J,K)	BLKM	array storing first sweep linearized coefficients
D2(I,J,K)	BLKM	array storing second sweep linearized coefficients
D3(I,J,K)	BLKM	array storing third sweep linearized coefficients
DENSR	CREF	reference density
DFW(I,J,K)	AD17	difference weight array
DIM1	NOND	inverse Reynolds number
DIM2	NOND	reference pressure/reference dynamic head
DIM3	NOND	reference pressure/(reference density x reference enthalpy)
DIM4	NOND	$1.0/(Rey \times P_r)$
DIM12	NOND	$2.0 \times DIM1$
DS	VARNO	index for dissipation
DT	MISC2	time step

Table III. (cont)

<u>FORTRAN symbol</u>	<u>Common block</u>	<u>Description</u>
DTCON	MISC2	inverse step
DTMAX	MISC2	maximum allowable time step
DTMIN	MISC2	minimum allowable time step
E(I,J,K)	BLKM	coupled matrix array storage
GRID(I)	GTRAN	grid distribution parameter
H	VARNO	index for enthalpy
I1	MGAUS	lower limit for matrix inversion
IADI	ADI1	ADI sweep number
IBC	ADI1	boundary condition boundary parameter
IDT	MISC2	time step index
IDTADJ	MISC2	time step control parameter
IDUPM1	OUTA	parameter controlling initial station print (see &READ9)
IEQ	ADI1	equation number
IGPRT(I)	GE01	geometry print control
IL	MGAUS	upper limit for matrix inversion
IPRINT	MISC2	print interval parameter (see &READ9)
IRERUN	MISC2	restart write control parameter
IREST	MISC2	restart read control parameter (see &READ1)
IVARPR(I)	MISC2	print parameter (see &READ9)
JADI	ADI1	ADI sweep parameter
JEQBC(I,J,K)	ADI1	boundary condition type parameter
JX	ADI2	direction 1 grid point index
KZ	ADI2	direction 3 grid point index
LX	ADI2	direction 1 grid point index

Table III. (cont)

<u>FORTRAN symbol</u>	<u>Common block</u>	<u>Description</u>
LX1	ADI3	first direction 1 interior point
LX2	ADI3	last direction 1 interior point
LY	ADI2	direction 2 grid point index
LY1	ADI3	first direction 2 interior point
LY2	ADI3	last direction 2 interior point
LZ	ADI2	direction 3 grid point index
LZ1	ADI3	first direction 3 interior point
LZ2	ADI3	last direction 3 interior point
LZPRNT	MISC2	3-D print control
MEQS	ADI1	number of equations to be solved
NT	MISC2	number of time steps to be run
NUMDX	MISC2	number of interior direction 1 points
NUMDY	MISC2	number of interior direction 2 points
NUMDZ	MISC2	number of interior direction 3 points
NX1	ADI4	first grid point--direction 1
NX2	ADI4	last grid point--direction 1
NY1	ADI4	first grid point--direction 2
NY2	ADI4	last grid point--direction 2
NZ1	ADI4	first grid point--direction 3
NZ2	ADI4	last grid point--direction 3
P	VARNO	index for pressure
PCNT1	MISC2	time step control parameter
PCNT2	MISC2	time step control parameter
PREF	CREF	reference pressure
PRNDL	CREF	Prandtl number

Table III. (cont)

<u>FORTTRAN symbol</u>	<u>Common block</u>	<u>Description</u>
PTOT	BCCON	total pressure
R	VARNO	index for density
REY	CREF	Reynolds number
SN(I)	BLKM	array storing source term linearized coefficient
SSTEST	MISC2	maximum change in variable across the time step
T	VARNO	index for temperature
TAUW	TURB	wall shear
TREF	CREF	reference temperature
TTIME	MISC2	cumulative time
TTOT	BCCON	total temperature
U	VARNO	index for direction 1 velocity
USTAR	TURB	dimensionless velocity
V	VARNO	index for direction 2 velocity
VISCL	TURB	laminar reference viscosity
VISCR	CREF	reference viscosity
VS	VARNO	index for viscosity
W	VARNO	index for direction 3 velocity
WREF	CREF	reference velocity
XGMAX(I)	GRID1	maximum coordinate value
XGMIN(I)	GRID1	minimum coordinate value
XPLUS	TURB	dimensionless distance from surface

ORIGINAL FILED IN  
OF POOR QUALITY

81

Table V.  
Sample inputs for MINT code.

```

JOB,JN=SAMPLE,M=2100,T=300.
ACCOUNT,AC=,PW=
ACCESS,ON=OLOPL,PDN=SRAMNTS,ID=AESRAI.
ACCESS,ON=OLOBIN,PDN=SRAMNTB,ID=AESRAI.
ACCESS,ON=GRID,PDN=C3XCOR, ID=AESRAI,ED=2.
ASSIGN,ON=PLOT, A=FT01.
ASSIGN,ON=RST9, A=FT09.
ASSIGN,ON=RST19,A=FT19.
ASSIGN,ON=RST10,A=FT10.
ASSIGN,ON=RST20,A=FT20.
ASSIGN,ON=GRID, A=FT21.
LOR,ON=OLOBIN,MAP=PART,NA.
SAVE,ON=RST10,PDN=SAMA1,ID=AESRAI.
SAVE,ON=RST20,PDN=SAMB1,ID=AESRAI.
/EOF
***** C3X-GRID CASCADE 120X30 *****
***** TURBULENT FLOW *****
&READ1
INTAP1=19,INTAPE=9,IOTAPE=10,IOTAP1=20,
IREST=0,
&END
&READ9
NUMDX=118, NUMDZ=28,
JOBLL=55, JOBLL=67, KOBLL=117,
AVISC = 12*0.5,3*0.5,60*0.5,
IHSTAG=0, TREF=766., CLENG=0.07816, VISC=0.3423122E-04, DENSR=1.0972523,
LAMPLO=0,
FLWNG=72.38,
IVARPR(1)=25*1, 1,1,1,6*0.1,
DTMIN=0.1,ITEST=1000,IVISC=3,
IDUMPL=2,
NT=10,IPRINT=10,
DT=1.,
DTMAX=5.,
IGAS=811.,
TWALL(1)=0.8, 0.805, 0.81, 0.815, 0.816, 0.817, 0.818, 0.819, 0.82, 0.82,
TWALL(1)=16*0.82, 0.815, 0.81, 0.805, 0.795,
TWALL(1)=0.79, 0.777, 0.77, 0.76, 0.75, 0.74, 0.73, 0.72, 0.715, 0.707,
TWALL(1)=0.7, 0.697, 0.692, 6*0.69, 0.695,
TWALL(1)=0.702, 0.717, 0.73, 0.745, 0.755, 3*0.76, 0.762, 0.765,
TWALL(1)=0.767, 22*0.77, 0.775, 0.777, 0.779, 0.78, 0.782, 9*0.785,
0.78, 0.778, 0.775, 0.765, 0.763, 0.76, 0.755, 0.75, 0.745, 0.74, 0.738, 0.735,
TWALL(1)=0.77, 0.773, 0.774, 0.775, 0.76, 0.76, 0.76, 0.77, 0.78, 0.785, 0.79, 0.795,
IBLOW=0,BLOW(1)=8*0.0766,BLOW(1)=8*0.0643,
PTOTI=1.66,
IOTA=0, IOTAB=40,
&END
/EOF

```

Table VI.  
Sample outputs for COORD program.

AIRFOIL COORDINATES	
0.781610E+01	0.530000E-02
0.781150E+01	0.412000E-01
0.766240E+01	0.639100E+00
0.750240E+01	0.123570E+01
0.733350E+01	0.183010E+01
0.715750E+01	0.242210E+01
0.697560E+01	0.301220E+01
0.678940E+01	0.360150E+01
0.659970E+01	0.418970E+01
0.640740E+01	0.477670E+01
0.621260E+01	0.536220E+01
0.601600E+01	0.594870E+01
0.581710E+01	0.653360E+01
0.561570E+01	0.711760E+01
0.541100E+01	0.770300E+01
0.520190E+01	0.828140E+01
0.498700E+01	0.886050E+01
0.476480E+01	0.943960E+01
0.453280E+01	0.100940E+02
0.428850E+01	0.105766E+02
0.402720E+01	0.111364E+02
0.373760E+01	0.116817E+02
0.339850E+01	0.121976E+02
0.298350E+01	0.126538E+02
0.247070E+01	0.129339E+02
0.187430E+01	0.131376E+02
0.127230E+01	0.133023E+02
0.765800E+00	0.126164E+02
0.389400E+00	0.121894E+02
0.169700E+00	0.116547E+02
0.569000E+01	0.113711E+02
0.216000E+01	0.113741E+02
0.640000E-02	0.112274E+02
0.264000E-01	0.110822E+02
0.650000E-01	0.109332E+02
0.131200E+00	0.107935E+02
0.332800E+00	0.106557E+02
0.384800E+00	0.104000E+02
0.499900E+00	0.103023E+02
0.449400E+00	0.102116E+02
0.155190E+01	0.995770E+01
0.188850E+01	0.968150E+01
0.2231490E+01	0.939120E+01
0.2437740E+01	0.909320E+01
0.313390E+01	0.878260E+01
0.342040E+01	0.846150E+01
0.369750E+01	0.813080E+01
0.396540E+01	0.779090E+01
0.422400E+01	0.744300E+01
0.447600E+01	0.708740E+01
0.471910E+01	0.672490E+01
0.495480E+01	0.635640E+01
0.518340E+01	0.598170E+01
0.540510E+01	0.560200E+01
0.562030E+01	0.521770E+01
0.5842960E+01	0.482900E+01
	0.443640E+01
	0.404010E+01
	0.364060E+01

[illegible]



ORIGINAL PAGE IS  
OF POOR QUALITY

Table VI. (cont)

[illegible]

Table VI. (cont)

RADIAL MESH POINT = 2										JACOBIAN									
LOOPWISE MESH POINTS										ANGLE									
PY										GRT									
GRR										GTT									
GTT										GRT									
GRT										GTT									
GTT										GRT									
GRT										GTT									
GTT										GRT									
GRT										GTT									
GTT										GRT									
GRT										GTT									
GTT										GRT									
GRT										GTT									
GTT										GRT									
GRT										GTT									
GTT										GRT									
GRT										GTT									
GTT										GRT									
GRT										GTT									
GTT										GRT									
GRT										GTT									
GTT										GRT									
GRT										GTT									
GTT										GRT									
GRT										GTT									
GTT										GRT									
GRT										GTT									
GTT										GRT									
GRT										GTT									
GTT										GRT									
GRT										GTT									
GTT										GRT									
GRT										GTT									
GTT										GRT									
GRT										GTT									
GTT										GRT									
GRT										GTT									
GTT										GRT									
GRT										GTT									
GTT										GRT									
GRT										GTT									
GTT										GRT									
GRT										GTT									
GTT										GRT									
GRT										GTT									
GTT										GRT									
GRT										GTT									
GTT										GRT									
GRT										GTT									
GTT										GRT									
GRT										GTT									
GTT										GRT									
GRT										GTT									
GTT										GRT									
GRT										GTT									
GTT										GRT									
GRT										GTT									
GTT										GRT									
GRT										GTT									
GTT										GRT									
GRT										GTT									
GTT										GRT									
GRT										GTT									
GTT										GRT									
GRT										GTT									
GTT										GRT									
GRT										GTT									
GTT										GRT									
GRT										GTT									
GTT										GRT									
GRT										GTT									
GTT										GRT									
GRT										GTT									
GTT										GRT									
GRT										GTT									
GTT										GRT									
GRT										GTT									
GTT										GRT									
GRT										GTT									
GTT										GRT									
GRT										GTT									
GTT										GRT									
GRT										GTT									
GTT										GRT									
GRT										GTT									
GTT										GRT									
GRT										GTT									
GTT										GRT									
GRT										GTT									
GTT										GRT									
GRT										GTT									
GTT										GRT									
GRT										GTT									
GTT										GRT									
GRT										GTT									
GTT										GRT									
GRT										GTT									
GTT										GRT									
GRT										GTT									
GTT										GRT									
GRT										GTT									
GTT										GRT									
GRT										GTT									
GTT										GRT									
GRT										GTT									
GTT										GRT									
GRT										GTT									
GTT										GRT									
GRT										GTT									
GTT										GRT									
GRT										GTT									
GTT										GRT									
GRT										GTT									
GTT										GRT									
GRT										GTT									
GTT										GRT									
GRT										GTT									
GTT										GRT									
GRT										GTT									
GTT										GRT									
GRT										GTT									
GTT										GRT									
GRT										GTT									
GTT										GRT									
GRT										GTT									
GTT										GRT									
GRT										GTT									
GTT										GRT									
GRT										GTT									
GTT										GRT									
GRT										GTT									
GTT										GRT									
GRT										GTT									
GTT										GRT									
GRT										GTT									
GTT										GRT									
GRT										GTT									
GTT										GRT									
GRT										GTT									
GTT										GRT									
GRT										GTT									
GTT										GRT									
GRT										GTT									
GTT										GRT									
GRT										GTT									
GTT										GRT									
GRT										GTT									
GTT										GRT									
GRT										GTT									
GTT										GRT									
GRT										GTT									
GTT										GRT									
GRT										GTT									
GTT										GRT									
GRT										GTT									
GTT										GRT									
GRT										GTT									
GTT										GRT									
GRT										GTT									
GTT										GRT									
GRT										GTT									
GTT										GRT									
GRT										GTT									
GTT										GRT									
GRT										GTT									
GTT										GRT									
GRT										GTT									
GTT										GRT									
GRT										GTT									
GTT										GRT									
GRT										GTT									
GTT										GRT									
GRT										GTT									
GTT										GRT									
GRT										GTT									
GTT										GRT									
GRT										GTT									
GTT										GRT									
GRT										GTT									
GTT										GRT									
GRT										GTT									
GTT										GRT									
GRT										GTT									
GTT										GRT									
GRT										GTT									
GTT										GRT									
GRT										GTT									
GTT										GRT									
GRT										GTT									
GTT										GRT									
GRT										GTT									
GTT										GRT									
GRT										GTT									
GTT										GRT									
GRT										GTT									
GTT										GRT									
GRT										GTT									
GTT										GRT									
GRT										GTT									
GTT										GRT									
GRT										GTT									
GTT										GRT									
GRT										GTT									
GTT										GRT									
GRT										GTT									
GTT										GRT									
GRT										GTT									
GTT										GRT									
GRT										GTT									
GTT										GRT									
GRT										GTT									
GTT										GRT									
GRT										GTT									
GTT										GRT									

Table VI. (cont)

Table VI. (cont)

LOOPWISE MESH POINTS	PX	PY	GRR	GIT	RADIAL MESH POINT = 3	ANGLE	JACOBIAN
94	0.839630	0.000000	0.557120	0.9337E+00	0.168E+02	0.597E-03	0.738E-01
95	0.858050	0.000000	0.500440	0.168E+02	0.675E-03	0.895E-03	0.761E-01
96	0.875710	0.000000	0.445440	0.168E+03	0.807E-03	0.895E+02	0.815E-01
97	0.892380	0.000000	0.393130	0.168E+03	0.126E-02	0.895E+02	0.845E-01
98	0.907320	0.000000	0.342640	0.168E+03	0.129E-02	0.895E+02	0.865E-01
99	0.921660	0.000000	0.297860	0.168E+03	0.231E-02	0.895E+02	0.887E-01
100	0.934500	0.000000	0.254680	0.168E+03	0.430E-02	0.895E+02	0.920E-01
101	0.946170	0.000000	0.214690	0.168E+02	0.662E-02	0.895E+02	0.969E-01
102	0.956800	0.000000	0.178280	0.168E+02	0.922E-02	0.895E+02	1.025E-01
103	0.966400	0.000000	0.145910	0.168E+02	0.120E-01	0.895E+02	1.087E-01
104	0.975000	0.000000	0.117800	0.168E+02	0.158E-01	0.895E+02	1.153E-01
105	0.982600	0.000000	0.093400	0.168E+02	0.200E-01	0.895E+02	1.222E-01
106	0.989200	0.000000	0.072200	0.168E+02	0.245E-01	0.895E+02	1.292E-01
107	0.994800	0.000000	0.053800	0.168E+02	0.292E-01	0.895E+02	1.362E-01
108	0.999400	0.000000	0.037800	0.168E+02	0.340E-01	0.895E+02	1.431E-01
109	1.003000	0.000000	0.023800	0.168E+02	0.388E-01	0.895E+02	1.498E-01
110	1.005600	0.000000	0.012400	0.168E+02	0.436E-01	0.895E+02	1.563E-01
111	1.007200	0.000000	0.003200	0.168E+02	0.484E-01	0.895E+02	1.625E-01
112	1.007800	0.000000	0.000000	0.168E+02	0.532E-01	0.895E+02	1.684E-01
113	1.007400	0.000000	0.000000	0.168E+02	0.580E-01	0.895E+02	1.739E-01
114	1.006000	0.000000	0.000000	0.168E+02	0.628E-01	0.895E+02	1.790E-01
115	1.003600	0.000000	0.000000	0.168E+02	0.676E-01	0.895E+02	1.837E-01
116	1.000200	0.000000	0.000000	0.168E+02	0.724E-01	0.895E+02	1.880E-01
117	0.995800	0.000000	0.000000	0.168E+02	0.772E-01	0.895E+02	1.918E-01
118	0.990400	0.000000	0.000000	0.168E+02	0.820E-01	0.895E+02	1.951E-01
119	0.984000	0.000000	0.000000	0.168E+02	0.868E-01	0.895E+02	1.979E-01
120	0.976600	0.000000	0.000000	0.168E+02	0.916E-01	0.895E+02	2.002E-01
121	0.968200	0.000000	0.000000	0.168E+02	0.964E-01	0.895E+02	2.020E-01
122	0.958800	0.000000	0.000000	0.168E+02	1.012E-01	0.895E+02	2.033E-01
123	0.948400	0.000000	0.000000	0.168E+02	1.060E-01	0.895E+02	2.041E-01
124	0.937000	0.000000	0.000000	0.168E+02	1.108E-01	0.895E+02	2.044E-01
125	0.924600	0.000000	0.000000	0.168E+02	1.156E-01	0.895E+02	2.042E-01
126	0.911200	0.000000	0.000000	0.168E+02	1.204E-01	0.895E+02	2.035E-01
127	0.896800	0.000000	0.000000	0.168E+02	1.252E-01	0.895E+02	2.023E-01
128	0.881400	0.000000	0.000000	0.168E+02	1.300E-01	0.895E+02	2.006E-01
129	0.865000	0.000000	0.000000	0.168E+02	1.348E-01	0.895E+02	1.984E-01
130	0.847600	0.000000	0.000000	0.168E+02	1.396E-01	0.895E+02	1.957E-01
131	0.829200</						

Table VI. (cont)

LOCAL-WISE MESH POINTS										RADIAL MESH POINT = 4										JACORIAN																																																																																	
PX										GTT										ANGLE																																																																																	
101	100	99	98	97	96	95	94	93	92	91	90	89	88	87	86	85	84	83	82	81	80	79	78	77	76	75	74	73	72	71	70	69	68	67	66	65	64	63	62	61	60	59	58	57	56	55	54	53	52	51	50	49	48	47	46	45	44	43	42	41	40	39	38	37	36	35	34	33	32	31	30	29	28	27	26	25	24	23	22	21	20	19	18	17	16	15	14	13	12	11	10	9	8	7	6	5	4	3	2	1	0
101	100	99	98	97	96	95	94	93	92	91	90	89	88	87	86	85	84	83	82	81	80	79	78	77	76	75	74	73	72	71	70	69	68	67	66	65	64	63	62	61	60	59	58	57	56	55	54	53	52	51	50	49	48	47	46	45	44	43	42	41	40	39	38	37	36	35	34	33	32	31	30	29	28	27	26	25	24	23	22	21	20	19	18	17	16	15	14	13	12	11	10	9	8	7	6	5	4	3	2	1	0
101	100	99	98	97	96	95	94	93	92	91	90	89	88	87	86	85	84	83	82	81	80	79	78	77	76	75	74	73	72	71	70	69	68	67	66	65	64	63	62	61	60	59	58	57	56	55	54	53	52	51	50	49	48	47	46	45	44	43	42	41	40	39	38	37	36	35	34	33	32	31	30	29	28	27	26	25	24	23	22	21	20	19	18	17	16	15	14	13	12	11	10	9	8	7	6	5	4	3	2	1	0
101	100	99	98	97	96	95	94	93	92	91	90	89	88	87	86	85	84	83	82	81	80	79	78	77	76	75	74	73	72	71	70	69	68	67	66	65	64	63	62	61	60	59	58	57	56	55	54	53	52	51	50	49	48	47	46	45	44	43	42	41	40	39	38	37	36	35	34	33	32	31	30	29	28	27	26	25	24	23	22	21	20	19	18	17	16	15	14	13	12	11	10	9	8	7	6	5	4	3	2	1	0
101	100	99	98	97	96	95	94	93	92	91	90	89	88	87	86	85	84	83	82	81	80	79	78	77	76	75	74	73	72	71	70	69	68	67	66	65	64	63	62	61	60	59	58	57	56	55	54	53	52	51	50	49	48	47	46	45	44	43	42	41	40	39	38	37	36	35	34	33	32	31	30	29	28	27	26	25	24	23	22	21	20	19	18	17	16	15	14	13	12	11	10	9	8	7	6	5	4	3	2	1	0
101	100	99	98	97	96	95	94	93	92	91	90	89	88	87	86	85	84	83	82	81	80	79	78	77	76	75	74	73	72	71	70	69	68	67	66	65	64	63	62	61	60	59	58	57	56	55	54	53	52	51	50	49	48	47	46	45	44	43	42	41																																									

Table VI. (cont)

[illegible]

ORIGINAL PAGE IS  
OF POOR QUALITY

Table VI. (cont)

[illegible]

ORIGINAL PAGE IS  
OF POOR QUALITY

Table VI. (cont)

[illegible]



Table VI. (cont)

92	0.162494622E+01	0.1422E+01	0.220E+03	0.000E+00	0.900E+02	0.177E+02
93	0.18190104E+01	0.1422E+01	0.220E+03	0.000E+00	0.900E+02	0.177E+02
94	0.20318043E+01	0.1422E+01	0.220E+03	0.000E+00	0.900E+02	0.177E+02
95	0.22629143E+01	0.1422E+01	0.220E+03	0.000E+00	0.900E+02	0.177E+02
96	0.25157920E+01	0.1422E+01	0.220E+03	0.000E+00	0.900E+02	0.177E+02
97	0.27477507E+01	0.1422E+01	0.220E+03	0.000E+00	0.900E+02	0.177E+02
98	0.30782355E+01	0.1422E+01	0.220E+03	0.000E+00	0.900E+02	0.177E+02
99	0.33578705E+01	0.1422E+01	0.220E+03	0.000E+00	0.900E+02	0.177E+02
100	0.35645317E+01	0.1422E+01	0.220E+03	0.000E+00	0.900E+02	0.177E+02
101	0.36500000E+01	0.1422E+01	0.220E+03	0.000E+00	0.900E+02	0.177E+02



ORIGINAL FILE  
OF POOR QUALITY

Table VI. (cont)

[illegible]

Table VII. (cont)

[illegible]

97

Table VII. (cont)

[illegible]

Table VII. (cont)

[illegible]

0.1286058037E+01	58	0.1286058037E+01
------------------	----	------------------

100



Table VII. (cont)

[illegible]

102

[illegible]

Table VII. (cont)

[illegible]

Table VII. (cont)

[illegible]

ORIGINAL PAGE IS  
OF POOR QUALITY

Table VII. (cont)

[illegible]

Table VII. (cont)

The image displays a highly complex, black-and-white abstract pattern. It consists of numerous small, interconnected geometric shapes and lines, creating a dense, textured appearance. The pattern is highly repetitive and symmetrical, suggesting a complex, possibly fractal-like structure. The overall effect is one of intense complexity and repetition, with the pattern filling the entire frame. The pattern is composed of many small, interconnected shapes and lines, creating a highly textured, almost crystalline appearance. The overall effect is one of intense complexity and repetition.

ORECAST DUMP COMPLETED AT TIME STEP 10 UNIT NO. = 10 RESTART NO. = 1

Table VII. (cont)

***** FINAL FLOW FIELD ***** RESULTS AT 1 STEP NO. 10 ***** ***** U-VL *****									
LZ=									
0	1	2	3	4	5	6	7	8	9
129	0	0	0	0	0	0	0	0	0
118	0	0	0	0	0	0	0	0	0
117	0	0	0	0	0	0	0	0	0
116	0	0	0	0	0	0	0	0	0
115	0	0	0	0	0	0	0	0	0
114	0	0	0	0	0	0	0	0	0
113	0	0	0	0	0	0	0	0	0
112	0	0	0	0	0	0	0	0	0
111	0	0	0	0	0	0	0	0	0
110	0	0	0	0	0	0	0	0	0
109	0	0	0	0	0	0	0	0	0
108	0	0	0	0	0	0	0	0	0
107	0	0	0	0	0	0	0	0	0
106	0	0	0	0	0	0	0	0	0
105	0	0	0	0	0	0	0	0	0
104	0	0	0	0	0	0	0	0	0
103	0	0	0	0	0	0	0	0	0
102	0	0	0	0	0	0	0	0	0
101	0	0	0	0	0	0	0	0	0
100	0	0	0	0	0	0	0	0	0
99	0	0	0	0	0	0	0	0	0
98	0	0	0	0	0	0	0	0	0
97	0	0	0	0	0	0	0	0	0
96	0	0	0	0	0	0	0	0	0
95	0	0	0	0	0	0	0	0	0
94	0	0	0	0	0	0	0	0	0
93	0	0	0	0	0	0	0	0	0
92	0	0	0	0	0	0	0	0	0
91	0	0	0	0	0	0	0	0	0
90	0	0	0	0	0	0	0	0	0
89	0	0	0	0	0	0	0	0	0
88	0	0	0	0	0	0	0	0	0
87	0	0	0	0	0	0	0	0	0
86	0	0	0	0	0	0	0	0	0
85	0	0	0	0	0	0	0	0	0
84	0	0	0	0	0	0	0	0	0
83	0	0	0	0	0	0	0	0	0
82	0	0	0	0	0	0	0	0	0
81	0	0	0	0	0	0	0	0	0
80	0	0	0	0	0	0	0	0	0
79	0	0	0	0	0	0	0	0	0
78	0	0	0	0	0	0	0	0	0
77	0	0	0	0	0	0	0	0	0
76	0	0	0	0	0	0	0	0	0
75	0	0	0	0	0	0	0	0	0
74	0	0	0	0	0	0	0	0	0
73	0	0	0	0	0	0	0	0	0
72	0	0	0	0	0	0	0	0	0
71	0	0	0	0	0	0	0	0	0
70	0	0	0	0	0	0	0	0	0
69	0	0	0	0	0	0	0	0	0
68	0	0	0	0	0	0	0	0	0
67	0	0	0	0	0	0	0	0	0
66	0	0	0	0	0	0	0	0	0
65	0	0	0	0	0	0	0	0	0
64	0	0	0	0	0	0	0	0	0
63	0	0	0	0	0	0	0	0	0
62	0	0	0	0	0	0	0	0	0
61	0	0	0	0	0	0	0	0	0
60	0	0	0	0	0	0	0	0	0
59	0	0	0	0	0	0	0	0	0
58	0	0	0	0	0	0	0	0	0
57	0	0	0	0	0	0	0	0	0
56	0	0	0	0	0	0	0	0	0
55	0	0	0	0	0	0	0	0	0
54	0	0	0	0	0	0	0	0	0
53	0	0	0	0	0	0	0	0	0
52	0	0	0	0	0	0	0	0	0
51	0	0	0	0	0	0	0	0	0
50	0	0	0	0	0	0	0	0	0
49	0	0	0	0	0	0	0	0	0
48	0	0	0	0	0	0	0	0	0
47	0	0	0	0	0	0	0	0	0
46	0	0	0	0	0	0	0	0	0
45	0	0	0	0	0	0	0	0	0
44	0	0	0	0	0	0	0	0	0
43	0	0	0	0	0	0	0	0	0
42	0	0	0	0	0	0	0	0	0
41	0	0	0	0	0	0	0	0	0
40	0	0	0	0	0	0	0	0	0
39	0	0	0	0	0	0	0	0	0
38	0	0	0	0	0	0	0	0	0
37	0	0	0	0	0	0	0	0	0
36	0	0	0	0	0	0	0	0	0
35	0	0	0	0	0	0	0	0	0
34	0	0	0	0	0	0	0	0	0
33	0	0	0	0	0	0	0	0	0
32	0	0	0	0	0	0	0	0	0
31	0	0	0	0	0	0	0	0	0
30	0	0	0	0	0	0	0	0	0
29	0	0	0	0	0	0	0	0	0
28	0	0	0	0	0	0	0	0	0
27	0	0	0	0	0	0	0	0	0
26	0	0	0	0	0	0	0	0	0
25	0	0	0	0	0	0	0	0	0
24	0	0	0	0	0	0	0	0	0
23	0	0	0	0	0	0	0	0	0
22	0	0	0	0	0	0	0	0	0
21	0	0	0	0	0	0	0	0	0
20	0	0	0	0	0	0	0	0	0
19	0	0	0	0	0	0	0	0	0
18	0	0	0	0	0	0	0	0	0
17	0	0	0	0	0	0	0	0	0
16	0	0	0	0	0	0	0	0	0
15	0	0	0	0	0	0	0	0	0
14	0	0	0	0	0	0	0	0	0
13	0	0	0	0	0	0	0	0	0
12	0	0	0	0	0	0	0	0	0
11	0	0	0	0	0	0	0	0	0
10	0	0	0	0	0	0	0	0	0
9	0	0	0	0	0	0	0	0	0
8	0	0	0	0	0	0	0	0	0
7	0	0	0	0	0	0	0	0	0
6	0	0	0	0	0	0	0	0	0
5	0	0	0	0	0	0	0	0	0
4	0	0	0	0	0	0	0	0	0
3	0	0	0	0	0	0	0	0	0
2	0	0	0	0	0	0	0	0	0
1	0	0	0	0	0	0	0	0	0
0	0	0	0	0	0	0	0	0	0





Table VII. (cont)

[illegible]

Table VII. (cont)

111

Table VII. (cont)

[illegible]

[illegible]

Table VII. (cont)

[illegible]

## Table VII. (cont)

[illegible]

[illegible][illegible]



Table VII. (cont)

Table VII. (cont)

[illegible]

Table VII. (cont)

119

[illegible]

[illegible]

[illegible]

## Table VII. (cont)

[illegible]

Table VII. (cont)

[illegible]



Table VII. (cont)

[illegible]

[illegible]

Table VII. (cont)

[illegible]

This image is a highly complex, black-and-white abstract pattern. It appears to be a dense, textured surface, possibly a microscopic view of a material or a corrupted digital image. The pattern is composed of numerous small, irregular shapes, lines, and clusters of pixels, creating a highly detailed and intricate visual field. The overall effect is one of intense visual noise and complexity, with no discernible figures, objects, or text. The pattern seems to have a crystalline or organic quality, with various structures and voids interspersed throughout. The density of the pattern is high, with very little white space visible between the black elements. The overall impression is one of a vast, unending field of intricate detail.

[illegible][illegible]

[illegible]

131

Table VII. (cont)

[illegible]



Table VII. (cont)

133

This image displays a highly complex, repeating geometric pattern. It consists of a dense array of small, interconnected shapes and lines, creating a textured, almost crystalline appearance. The pattern is composed of numerous small, interconnected shapes and lines, creating a highly textured and intricate visual effect. The overall effect is one of a complex, repeating digital or architectural design, possibly a stylized representation of a city grid or a complex network. The pattern is composed of numerous small, interconnected shapes and lines, creating a highly textured and intricate visual effect.

[illegible]

[illegible]

[illegible]

[illegible][illegible]

[illegible][illegible]

[illegible]



Table VII. (cont)

141

[illegible]

Table VII. (cont)

[illegible]

[illegible]

RESULTS AT STEP NO.	
TIME PLOTS	DIR1 PLOTS
TIME PLOTS	DIR3 PLOTS

APPENDIX C  
LIST OF ACRONYMS, ABBREVIATIONS, AND SYMBOLS

<u>Term</u>	<u>Definition</u>
$A^+$	van Driest damping coefficient
ADI	alternating direction implicit
ADVR	axial velocity density ratio
$b$	total or effective viscosity
$C_p$	specific heat at constant pressure
$D$	damping parameter
$d$	distance to the nearest wall
$d^+$	dimensionless distance to the nearest wall
$\mathbb{D}$	deformation tensor
$h$	enthalpy
$h/h_0$	normalized heat transfer coefficient
$h_1, h_2, h_3$	normal distance between loops
$I$	identity tensor
$k$	turbulence kinetic energy
$K_B$	bulk viscosity coefficient
LBI	linearized block implicit
$\ell$	mixing length
$\ell_\infty$	mixing length in the core flow region
Ma	Mach number
MINT code	multidimensional, implicit, nonlinear, time-dependent code
N-S	Navier-Stokes
$P$	pressure
$Pr$	laminar Prandtl number
$\vec{P}(r,s)$	position vector

<u>Term</u>	<u>Definition</u>
$Pr_t$	effective turbulent Prandtl number
$P_s$	static pressure
$P_s/P_T$	static pressure/total pressure
$P_t$	total pressure
$\vec{Q}$	mean heat flux vector
$q$	magnitude of the velocity
$\vec{Q}_T$	turbulent heat flux vector
$R$	universal gas constant
$r$	radial parameter
$Re$	Reynolds number
$R_\tau$	local ratio of turbulent to laminar viscosity
$s$	arc length parameter
SRA	Scientific Research Associates
$T$	temperature
$t$	time
$T_0$	reference temperature
$T_t$	stagnation temperature
$T_w/T_g$	wall to gas temperature ratio
$U$	velocity
$\vec{U}$	velocity vector
$u$	velocity component in x-direction
$\vec{u}$	fluctuation velocity vector
$U_e$	edge velocity
$u_\tau$	friction velocity
$v$	velocity component in y-direction

<u>Term</u>	<u>Definition</u>
$w$	velocity component in z-direction
$w_e$	w at the edge of the boundary layer
$x, x_1$	Cartesian coordinate in the transverse direction
$x/cx$	fraction of axial chord
$x_{te}$	trailing edge location
$y, x_2$	Cartesian coordinate in the spanwise direction
$y^1, y^2, y^3$	computational coordinates
$z, x_3$	Cartesian coordinate in the streamwise direction
1-D	one-dimensional
2-D	two-dimensional
3-D	three-dimensional
$\Delta x$	grid spacing
$\delta$	boundary layer thickness
$\delta_{ps}$	pressure surface trailing edge boundary layer thickness
$\delta_{ss}$	suction surface trailing edge boundary layer thickness
$\epsilon$	turbulence energy dissipation rate
$\kappa$	von Karman constant
$\kappa$	mean thermal conductivity
$\mu$	dynamic viscosity
$\mu^T$	turbulent viscosity
$\nu_{art}$	artificial dissipation
$\xi, \eta, \zeta$	computational coordinates
$\bar{\pi}$	molecular stress tensor
$\pi^T$	turbulent stress tensor
$\rho$	density

<u>Term</u>	<u>Definition</u>
$\sigma$	artificial dissipation parameter
$\tau$	time
$\tau_l$	local shear stress
$\tau_{xx}, \tau_{xy}, \text{ etc.}$	component of stress tensor
$\Phi$	mean flow dissipation rate



## REFERENCES

1. R.A. Delaney, "Time Marching Analysis of Steady Transonic Flow in Turbomachinery Cascades Using the Hopscotch Method," ASME Journal of Engineering for Power, Vol 105, pp 272-279, 1983.
2. J.R. Caspar, D.E. Hobbs, and R.L. Davis, "Calculation of Two-Dimensional Cascade Flow Using Finite Area Methods," AIAA Journal, Vol 18, 1980.
3. H. McDonald, "Computation of Turbomachinery Boundary Layers, The Aerodynamics of Aircraft Gas Turbine Engines," AFAPL-TR-78-52, 1978.
4. E.C. Hansen, G.K. Serovy, and P.M. Sockol, "Axial Flow Compressor Turning Angle and Loss by Inviscid-Viscous Interaction Blade-to-Blade Computation," ASME Journal of Engineering for Power, Vol 102, 1980.
5. T. Rehyner and I. Flugge-Lotz, "The Interaction of Shock Waves with a Laminar Boundary Layer," International Journal of Nonlinear Mechanics, Vol 3, 1968.
6. L.S. Langston, M.L. Nice, and R.M. Hooper, "Three-Dimensional Flow within a Turbine Cascade Passage," ASME Journal of Engineering for Power, Vol 99, pp 21-28, 1977.
7. S.J. Shamroth and H. McDonald, "An Assessment of an Ensemble-Averaged Navier-Stokes Calculation Procedure for Cascade Flow Fields," Scientific Research Associates Report R82-92001-F, 1982.
8. S.J. Shamroth, H. McDonald, and W.R. Briley, "Prediction of Cascade Flow Fields Using the Averaged Navier-Stokes Equations," ASME Journal of Engineering for Gas Turbines and Power, Vol 106, 1984.
9. S.J. Shamroth, R.J. Yang, and H. McDonald, "Further Development of a Transonic Cascade Analysis," Scientific Research Associates Report R83-9200015-F, 1983.

10. S.J. Shamroth, H.J. Gibeling, and H. McDonald, "A Navier-Stokes Solution for Laminar and Turbulent Flow through a Cascade of Airfoils," AIAA Paper No. 89-1426, Scientific Research Associates Report R79-920004-F, 1980.
11. S.J. Shamroth, H. McDonald, and W.R. Briley, "A Navier-Stokes Solution for Transonic Flow through a Cascade," Scientific Research Associates Report R81-920007-F, 1982.
12. H. McDonald, S.J. Shamroth, and W.R. Briley, "Transonic Flows with Viscous Effects," Transonic Shock and Multi-Dimensional Flows: Advances in Scientific Computing, Academic Press, New York, 1982.
13. W.R. Briley and H. McDonald, "Solution of the Multi-Dimensional Compressible Navier-Stokes Equations by a Generalized Implicit Method," Journal of Computational Physics, Vol 24, 1977.
14. S.J. Shamroth and S.J. Gibeling, "Analysis of Turbulent Flow about an Isolated Airfoil Using a Time-Dependent Navier-Stokes Procedure," Paper presented at AGARD Specialists Meeting on Boundary Layer Effects on Unsteady Airloads, Aix-en-Provence, France, September 1980.
15. H.E. Stephens and D.E. Hobbs, "Design and Performance of Supercritical Airfoils for Axial Flow Compressors," Pratt and Whitney Aircraft Report FR11455, 1979.
16. D.E. Hobbs, J.H. Wagner, J.F. Dannenhoffer, and R.P. Dring, "Wake Experiment and Modeling for Fore and Aft-Loaded Compressor Cascade," Pratt and Whitney Aircraft Report FR13514, 1980.
17. J.F. Thompson, F.C. Thames, and C.W. Mastin, "Boundary Fitted Curvilinear Coordinate Systems for Solution of Partial Differential Equations on Fields Containing Any Number of Arbitrary Two-Dimensional Bodies," NASA CR-2729, July 1977.
18. P.R. Eiseman, "A Coordinate System for a Viscous Transonic Cascade Analysis," Journal of Computational Physics, Vol 26, pp 307-338, March 1978.

19. Y.H. Oh, "An Analytical Transformation Technique for Generating Uniformly Spaced Computational Mesh in Numerical Grid Generation Techniques," NASA CP-2166, 1980.
20. P.R. Eiseman, "Coordinate Generation with Precise Controls over Mesh Properties," Journal of Computational Physics, Vol 47, 1982.
21. A.B. Turner, "Local Heat Transfer Measurements on a Gas Turbine Blade," Journal of Mechanical Engineering Sciences, Vol 13, 1971.
22. L.D. Hylton, M.S. Mihelc, E.R. Turner, D.A. Nealy, and R.E. York, "Analytical and Experimental Evaluation of the Heat Transfer Distribution over the Surface of Turbine Vanes," NASA CR-168015, May 1983.
23. P.D. Thomas and C.K. Lombard, "Geometric Conservation Law and Its Application to Flow Computation on Moving Grids," AIAA Journal, Vol 17, No. 10, 1979.
24. R.G. Hindman, "Generalized Coordinate Forms of Governing Fluid Equation and Associated Geometrically Induced Errors," AIAA Journal, Vol 20, 1982.
25. H. Schlichting, Boundary Layer Theory, McGraw-Hill, New York, 1960.
26. H. McDonald and R.W. Fish, "Practical Calculation of Transitional Boundary Layers," International Journal of Heat and Mass Transfer, Vol 16, No. 9, 1973.
27. W.P. Jones and B.E. Launder, "The Prediction of Laminarization with a Two-Equation Model of Turbulence," International Journal of Heat and Mass Transfer, Vol 15, 1972.
28. S.J. Shamroth and H.J. Gibeling, "A Compressible Solution of the Navier-Stokes Equations for Turbulent Flow about an Airfoil," NASA CR-3183, 1979.
29. B.E. Launder and D.B. Spalding, "The Numerical Computation of Turbulent Flows," Computer Methods in Applied Mechanics and Engineering, Vol 3, pp 269-287, 1974.

30. V.C. Patel, W. Rodi, and G. Scheurer, "Evaluation of Turbulence Models for Near Wall and Low Reynolds Number Flow," Third Symposium on Turbulent Shear Flow, University of California, Davis, 1981.
31. W.R. Briley and H. McDonald, "Computation of Three-Dimensional Horseshoe Vortex Flow Using the Navier-Stokes Equations," Seventh International Conference on Numerical Methods in Fluid Dynamics, 1980.
32. C.W. Mastin, "Error Induced by Coordinate Systems," Numerical Grid Generation, J.F. Thompson, ed., Elsevier Publishing, New York, 1982.
33. I. Lindemuth and J. Killeen, "Alternating Direction Implicit Techniques for Two-Dimensional Magnetohydrodynamic Calculations," Journal of Computational Physics, Vol 13, 1973.
34. W.R. Briley and H. McDonald, "On the Structure and Use of Linearized Block Implicit Schemes," Journal of Computational Physics, Vol 34, 1980.
35. J. Douglas and J.E. Gunn, "A General Formulation of Alternating Direction Methods," Numerische Mathematik, Vol 6, pp 428-453, 1964.
36. W.R. Briley, R.C. Buggeln, and H. McDonald, "Computation of Laminar and Turbulent Flow in 90 Degree Square Duct and Pipe Bends Using the Navier-Stokes Equation, Scientific Research Associates Report R82-920009-F, 1982.
37. N.S. Liu, S.J. Shamroth, and H. McDonald, "Numerical Solution of the Navier-Stokes Equations for Compressible Turbulent Two/Three-Dimensional Flows in the Terminal Shock Region of an Inlet/Diffuser," AIAA Paper 83-1892, 1983.
38. D.V. Roscoe, S.J. Shamroth, H.J. Gibeling, and H. McDonald, "Investigation of the Mechanism of Transonic Shock Wave/Boundary Layer Interactions Using a Navier-Stokes Analysis," U.S. Army Research Office Contract DAAG29-80-C-0082, Scientific Research Associates Report R84-930006-F, 1984.

39. S. Dhawan and R. Narasimha, "Some Properties of Boundary Layer Flow During Transition from Laminar to Turbulent Motion," *Journal of Fluid Mechanics*, Vol 3, pp 418-436, 1958.
40. T.J. Barber and L.S. Langston, "Three-Dimensional Modeling of Cascade Flows," AIAA Paper 79-0047, 17th Aerospace Science Meeting, 1979.
41. L.S. Langston, "Cross Flows in a Turbine Cascade Passage," *ASME Journal of Engineering for Power*, Vol 102, pp 866-874, 1980.
42. R.A. Graziani, M.F. Blair, J.R. Taylor, and R.E. Mayle, "An Experimental Study of Endwall and Airfoil Surface Heat Transfer in a Large Scale Turbine Blade Cascade," *ASME Journal of Engineering for Power*, Vol 102, pp 257-267, 1980.
43. C.H. Sieverding and P. Van den Bosche, "The Use of Colored Smoke to Visualize Secondary Flows in a Turbine-Blade Cascade," *Journal of Fluid Mechanics*, Vol 134, pp 85-89, 1983.
44. S.J. Shamroth and H. McDonald, "Development of a Design-Oriented Navier-Stokes Cascade Analysis," Scientific Research Associates Report R84-910006-F, March 1984.
45. R.M. Beam and R.F. Warming, "An Implicit Factored Scheme for Compressible Navier-Stokes Equations," *AIAA Journal*, Vol 16, 1978.
46. R.M. Beam and R.F. Warming, "An Implicit Finite Difference Algorithm for Hyperbolic Systems in Conservation Law Form," *Journal of Computational Physics*, Vol 22, 1976.
47. R.M. Beam and R.F. Warming, "Alternating Direction Implicit Methods for Parabolic Equations with a Mixed Derivative," *SIAM Journal on Scientific and Statistical Computing*, Vol 1, 1980.

1. Report No. NASA CR-174828		2. Government Accession No.		3. Recipient's Catalog No.	
4. Title and Subtitle Turbine Vane External Heat Transfer Volume II. Numerical Solutions of the Navier-Stokes Equations for Two- and Three-Dimensional Turbine Cascades with Heat Transfer				5. Report Date July 1985	
				6. Performing Organization Code	
7. Author(s) R. J. Yang, B. C. Weinberg, S. J. Shamroth, H. McDonald				8. Performing Organization Report No. EDR 11984, Volume II	
9. Performing Organization Name and Address Performed by Scientific Research Associates, Inc., P.O. Box 498, Glastonbury, Connecticut 06033 Under subcontract from Allison Gas Turbine Division of General Motors Corporation, P.O. Box 420, Indianapolis, Indiana 46206-0420				10. Work Unit No.	
				11. Contract or Grant No. NAS3-23695	
12. Sponsoring Agency Name and Address National Aeronautics and Space Administration Washington, D.C. 20546				13. Type of Report and Period Covered Contractor report	
				14. Sponsoring Agency Code	
15. Supplementary Notes Prepared in cooperation with NASA Project Manager H. J. Gladden, NASA-Lewis Research Center, Cleveland, Ohio					
16. Abstract  This two-volume report addresses the progress of contract NAS3-23695 to improve the predictive design capabilities for external heat transfer to turbine vanes. Volume II describes work performed under subcontract by Scientific Research Associates. This analytical effort examined the application of the time-dependent ensemble-averaged Navier-Stokes equations to transonic turbine cascade flow fields. In particular, efforts focused on an assessment of the procedure in conjunction with a suitable turbulence model to calculate steady turbine flow fields using an O-type coordinate system. Three cascade configurations were considered.  Comparisons were made between the predicted and measured surface pressures and heat transfer distributions wherever available. In general, the pressure predictions were in good agreement with the data. Heat transfer calculations also showed good agreement when an empirical transition model was used. However, further work in the development of laminar-turbulent transitional models is indicated. The calculations showed most of the known features associated with turbine cascade flow fields. These results indicate the ability of the Navier-Stokes analysis to predict, in reasonable amounts of computation time, the surface pressure distribution, heat transfer rates, and viscous flow development for turbine cascades operating at realistic flow conditions.					
17. Key Words (Suggested by Author(s)) Turbine aerodynamics, turbine heat transfer, film cooling, boundary layer heat transfer, Navier-Stokes, turbine cascade analysis				18. Distribution Statement	
19. Security Classif. (of this report) Unclassified		20. Security Classif. (of this page) Unclassified		21. No. of Pages 153	
				22. Price*	

\* For sale by the National Technical Information Service, Springfield, Virginia 22151